

3-11-2011

Direction Finding With Mutually Orthogonal Antennas

David F. Chick

Follow this and additional works at: <https://scholar.afit.edu/etd>

Part of the [Electromagnetics and Photonics Commons](#), and the [Signal Processing Commons](#)

Recommended Citation

Chick, David F, "Direction Finding With Mutually Orthogonal Antennas" (2011). *Theses and Dissertations*. 1368.
<https://scholar.afit.edu/etd/1368>

This Thesis is brought to you for free and open access by the Student Graduate Works at AFIT Scholar. It has been accepted for inclusion in Theses and Dissertations by an authorized administrator of AFIT Scholar. For more information, please contact richard.mansfield@afit.edu.



**DIRECTION FINDING WITH MUTUALLY
ORTHOGONAL ANTENNAS**

THESIS

David F. Chick, 2d Lt, USAF
AFIT/GE/ENG/11-03

**DEPARTMENT OF THE AIR FORCE
AIR UNIVERSITY**

AIR FORCE INSTITUTE OF TECHNOLOGY

Wright-Patterson Air Force Base, Ohio

APPROVED FOR PUBLIC RELEASE; DISTRIBUTION UNLIMITED

The views expressed in this thesis are those of the author and do not reflect the official policy or position of the United States Air Force, the Department of Defense, or the United States Government.

This material is declared a work of the U.S. Government and is not subject to copyright protection in the United States.

AFIT/GE/ENG/11-03

DIRECTION FINDING WITH
MUTUALLY ORTHOGONAL ANTENNAS

THESIS

Presented to the Faculty

Department of Electrical and Computer Engineering

Graduate School of Engineering and Management

Air Force Institute of Technology

Air University

Air Education and Training Command

In Partial Fulfillment of the Requirements for the
Degree of Master of Science in Electrical Engineering

David F. Chick, BS

2d Lt, USAF

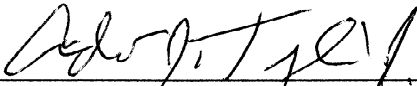
March 2011

APPROVED FOR PUBLIC RELEASE; DISTRIBUTION UNLIMITED

DIRECTION FINDING WITH
MUTUALLY ORTHOGONAL ANTENNAS

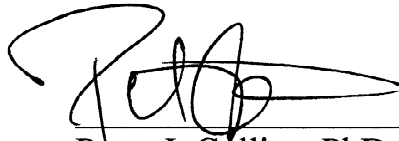
David F. Chick, BS
2d Lt, USAF

Approved:



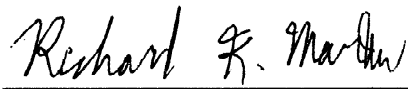
Andrew Terzuoli, PhD (Chairman)

07 Mar 2011
Date



Peter J. Collins, PhD (Member)

07 MAR 2011
Date



Richard Martin, PhD (Member)

07 Mar 2011
Date

Abstract

Estimating the direction-of-arrival of incident electromagnetic plane waves (a.k.a. direction finding or DF) has typically been accomplished in the past using arrays of spatially separated antennas. The spatial separation produces a delay in each antenna's measured voltage due to the finite propagation time as the wave strikes each antenna in succession. In this thesis, we approach the problem differently by using three antennas that have been oriented in orthogonal directions but are co-located at the origin of a coordinate system. Being co-located, this mutually orthogonal arrangement of antennas cannot detect the propagation phase delay and must rely solely on the polarization properties of the incident waves. Using the vector effective height concept, three algorithms are formulated. The first algorithm estimates the direction-of-arrival by computing a vector that is perpendicular to the locus of the instantaneous electric field vector measured at the origin of the coordinate system. The second and third algorithms are based on the well-known maximum likelihood and MUSIC algorithms. Simulation results show that each algorithm can estimate the direction-of-arrival with a root-mean-squared error within 1° or less when the incident wave is circularly polarized, the antennas are small compared to wavelength, and the signal-to-noise ratio is above 20dB.

AFIT/GE/ENG/11-03

*To my loving wife and my two
wonderful children*

Acknowledgements

I am wholeheartedly thankful to my thesis advisor, Dr. Andrew Terzuoli, whose support, advice, and encouragement from start to finish enabled me to develop an understanding of this subject. I would also like to thank my committee members Major Scott Goodman, Dr. Peter Collins, and Dr. Richard Martin as well as the sponsor, Dr. Charles Cerny from the Air Force Research Laboratory, for their continued support during this thesis effort.

David F. Chick

Table of Contents

	Page
Abstract	iv
Dedication	v
Acknowledgements	vi
Table of Contents	vii
List of Figures	ix
List of Tables	xvii
1. Direction Finding With Mutually Orthogonal Antennas	1-1
1.1. Introduction	1-1
1.2. Background: AFRL Contracted DF Work	1-3
1.3. Qualitative Comparison of DF Approaches	1-8
1.4. Potential Benefits & Impact	1-9
1.5. Conclusion	1-11
2. Common Direction Finding Methods and Literature Review	2-1
2.1. Introduction	2-1
2.2. Basic Concepts & the Narrowband Signal Model	2-1
2.3. Review of Common DF Methods	2-4
Classic Beam Forming	2-5
Monopulse	2-6
Phase Matching	2-7
2.4. DF Processing on Multiple Co-Channel Emitters	2-8
The Maximum Likelihood Technique	2-9
The MUSIC Technique	2-13
The ESPRIT Technique	2-18
2.5. Literature Review: DF With Orthogonal Antennas	2-19
2.6. Conclusion	2-27
3. Approach & Methodology	3-1
3.1. Introduction	3-1
3.2. Uniform Plane Wave Model	3-2
3.3. Vector Effective Height of Any Antenna	3-7
3.4. Using the Tripole as a Field Probe	3-9
3.5. Simple DF Algorithm Using the Tripole	3-12
3.6. DF With Three Non-Dipole Antennas	3-16
3.7. Testing the Algorithms	3-20
3.8. Conclusion	3-24

4. Results & Discussion	4-1
4.1. Introduction.....	4-1
4.2. Simple Tripole Algorithm Results.....	4-1
4.3. Maximum Likelihood (ML) Algorithm Results	4-7
ML on the Tripole.....	4-7
ML on the Bowtie Antennas	4-10
ML on the Biconical Antennas	4-13
4.4. MUSIC Algorithm Results	4-15
4.5. Performance Comparison.....	4-17
4.6. Further Discussion	4-18
4.7. Conclusion	4-19
5. Concluding Remarks & Future Work	5-1
5.1. Concluding Remarks.....	5-1
5.2. Future Work Possibilities.....	5-3
Appendix A: Wideband Antenna Simulations & Measurements	A-1
Appendix B: The Rotation Transform Matrix	B-1
Appendix C: Maximum Likelihood and MUSIC Algorithm Results	C-1
Bibliography	BIB-1

List of Figures

Figure	Page
1-1: Mutually orthogonal dipoles	1-3
1-2: Wideband antennas	1-6
1-3: Block diagram of envisioned DF system using mutually orthogonal antennas.....	1-7
2-1: Linear array with incident wave	2-2
2-2: Three mutually orthogonal dipoles (tripole) with coordinate convention	2-20
3-1: Coordinate systems	3-3
3-2: Axial ratios of an ellipse	3-5
3-3: Phase fronts of a TEM UPW traveling toward the origin.....	3-6
3-4: Orthogonal antennas	3-17
(a) Biconical antennas	
(b) Bowtie antennas	
3-5: Antenna dimensions.....	3-21
(a) Dipole	
(b) Bowtie	
(c) Biconical with spherical end caps	
4-1: Noise free power spectrum of the eight UPWs simulated in CST.....	4-3
4-2: Known (circles) and estimated (plus signs) directions-of-arrival of the eight (numbered) UPWs for the noise free case	4-3
4-3: SNR=40dB.....	4-4
4-4: SNR=35dB.....	4-4
4-5: SNR=30dB.....	4-4
4-6: SNR=25dB.....	4-4
4-7: SNR=20dB.....	4-4
4-8: SNR=15dB.....	4-4
4-9: SNR=10dB.....	4-5
4-10: SNR 30dB, AR 1.....	4-6
4-11: SNR 30dB, AR 2.....	4-6
4-12: SNR 30dB, AR 5.....	4-6
4-13: SNR 30dB, AR 10.....	4-6
4-14: SNR 30dB, AR 20.....	4-6
4-15: SNR 30dB, AR 80.....	4-6
4-16: ML Tripole Result: Signal at (10°, 20°), SNR = 40dB.....	4-8
4-17: ML Tripole Result: Signal at (10°, 20°), SNR = 30dB.....	4-8
4-18: ML Tripole Result: Signal at (10°, 20°), SNR = 20dB.....	4-8
4-19: ML Tripole Result: Signal at (10°, 20°), SNR = 10dB.....	4-8
4-20: ML Tripole Result: Signal at (45°, 60°), SNR = 40dB.....	4-8
4-21: ML Tripole Result: Signal at (45°, 60°), SNR = 30dB.....	4-8
4-22: ML Tripole Result: Signal at (45°, 60°), SNR = 20dB.....	4-9

Figure	Page
4-23: ML Tripole Result: Signal at (45°, 60°), SNR = 10dB.....	4-9
4-24: ML Tripole Result: Signal at (80°, 340°), SNR = 40dB.....	4-9
4-25: ML Tripole Result: Signal at (80°, 340°), SNR = 30dB.....	4-9
4-26: ML Tripole Result: Signal at (80°, 340°), SNR = 20dB.....	4-9
4-27: ML Tripole Result: Signal at (80°, 340°), SNR = 10dB.....	4-9
4-28: ML Tripole Result: Varying AR, AR = 1.....	4-10
4-29: ML Tripole Result: Varying AR, AR = 2.....	4-10
4-30: ML Tripole Result: Varying AR, AR = 5.....	4-10
4-31: ML Tripole Result: Varying AR, AR = 10.....	4-10
4-32: ML Tripole Result: Varying AR, AR = 20.....	4-10
4-33: ML Tripole Result: Varying AR, AR = 80.....	4-10
4-34: ML Bowtie Antenna Results, Signal 1.....	4-11
4-35: ML Bowtie Antenna Results, Signal 2.....	4-11
4-36: ML Bowtie Antenna Results, Signal 3.....	4-11
4-37: ML Bowtie Antenna Results, Signal 4.....	4-11
4-38: ML Bowtie Antenna Results, Signal 5.....	4-11
4-39: ML Bowtie Antenna Results, Signal 6.....	4-11
4-40: ML Bowtie Antenna Results, Signal 7.....	4-11
4-41: ML Bowtie Antenna Results, Signal 8.....	4-11
4-42: ML Bowtie Antenna Results, Signal 9.....	4-11
4-43: 205mm antenna, f = 0.5GHz, $\alpha=50^\circ$, <u>no</u> mutual coupling.....	4-14
4-44: 205mm antenna, f = 3GHz, $\alpha=50^\circ$, <u>no</u> mutual coupling.....	4-14
4-45: 205mm antenna, f = 3GHz, $\alpha=50^\circ$, mutual coupling included.....	4-14
4-46: 50mm antenna, f = 0.5GHz, $\alpha=50^\circ$, mutual coupling included.....	4-14
4-47: 50mm antenna, f = 1.5GHz, $\alpha=50^\circ$, mutual coupling included.....	4-14
4-48: 50mm antenna, f = 3GHz, $\alpha=50^\circ$, mutual coupling included.....	4-14
4-49: MUSIC spectrum of signal 1 ($\alpha=1^\circ$) showing sharp peak at the direction-of-arrival.....	4-16
4-50: 2D version of the MUSIC spectrum of signal 1 ($\alpha=1^\circ$) which clearly shows the difference between the known (circle) and estimated (plus) direction-of-arrival.....	4-16
4-51: MUSIC spectrum of signal 3 ($\alpha=30^\circ$).....	4-16
4-52: MUSIC spectrum of signal 6 ($\alpha=50^\circ$).....	4-16
4-53: RMSE (deg) vs SNR (dB), (θ, ϕ) = (40°, 50°).....	4-17
A-1: Photograph of the two different types of wideband antennas.....	A-2
A-2: Type 2 antenna.....	A-4
(a) Photograph	
(b) X-ray image	
(c) Plot showing equation of fit (axes in inches)	
A-3: CST Model of the type 2 antenna with important dimensions.....	A-5
A-4: Coax cable dimensions.....	A-7
A-5: Feed point with important dimensions.....	A-7

Figure	Page
A-6: Alternative view of the feed point	A-8
A-7: Current at 0.8GHz.....	A-9
A-8: Current at 1.3GHz.....	A-9
A-9: Current at 1.8GHz.....	A-9
A-10: Current at 2.5GHz.....	A-9
A-11: Current at 3.0GHz.....	A-10
A-12: Measurement arrangement.....	A-11
A-13: Close-up of mount.....	A-11
A-14: Equivalent arrangement with example incident wave at $\theta=60^\circ$, $\phi=45^\circ$	A-11
A-15: Measured vs. simulated S11	A-13
A-16: $\text{abs}(E_\theta)$ at 1.3GHz (with antenna drawn for reference).....	A-14
A-17: $\text{abs}(E_\theta)$ at 1.8GHz	A-15
A-18: $\text{abs}(E_\theta)$ at 2.1GHz	A-15
A-19: $\text{abs}(E_\theta)$ at 2.5GHz	A-15
A-20: $\text{abs}(E_\theta)$ at 3.0GHz	A-15
A-21: Frequency: 1.0GHz, $\theta = 10^\circ$	A-16
A-22: Frequency: 1.0GHz, $\theta = 20^\circ$	A-16
A-23: Frequency: 1.0GHz, $\theta = 60^\circ$	A-16
A-24: Frequency: 1.0GHz, $\theta = 90^\circ$	A-16
A-25: Frequency: 1.2GHz, $\theta = 10^\circ$	A-17
A-26: Frequency: 1.2GHz, $\theta = 30^\circ$	A-17
A-27: Frequency: 1.2GHz, $\theta = 60^\circ$	A-17
A-28: Frequency: 1.2GHz, $\theta = 80^\circ$	A-17
A-29: Frequency: 1.4GHz, $\theta = 20^\circ$	A-17
A-30: Frequency: 1.4GHz, $\theta = 50^\circ$	A-17
A-31: Frequency: 1.4GHz, $\theta = 70^\circ$	A-18
A-32: Frequency: 1.4GHz, $\theta = 80^\circ$	A-18
A-33: Frequency: 1.6GHz, $\theta = 10^\circ$	A-18
A-34: Frequency: 1.6GHz, $\theta = 30^\circ$	A-18
A-35: Frequency: 1.6GHz, $\theta = 60^\circ$	A-18
A-36: Frequency: 1.6GHz, $\theta = 80^\circ$	A-18
A-37: Frequency: 1.8GHz, $\theta = 10^\circ$	A-19
A-38: Frequency: 1.8GHz, $\theta = 30^\circ$	A-19
A-39: Frequency: 1.8GHz, $\theta = 70^\circ$	A-19
A-40: Frequency: 1.8GHz, $\theta = 90^\circ$	A-19
A-41: Frequency: 2.0GHz, $\theta = 10^\circ$	A-19
A-42: Frequency: 2.0GHz, $\theta = 30^\circ$	A-19
A-43: Frequency: 2.0GHz, $\theta = 60^\circ$	A-20
A-44: Frequency: 2.0GHz, $\theta = 80^\circ$	A-20
A-45: Frequency: 2.2GHz, $\theta = 10^\circ$	A-20
A-46: Frequency: 2.2GHz, $\theta = 30^\circ$	A-20
A-47: Frequency: 2.2GHz, $\theta = 60^\circ$	A-20

Figure	Page
A-48: Frequency: 2.2GHz, $\theta = 80^\circ$	A-20
A-49: Frequency: 2.4GHz, $\theta = 10^\circ$	A-21
A-50: Frequency: 2.4GHz, $\theta = 30^\circ$	A-21
A-51: Frequency: 2.4GHz, $\theta = 60^\circ$	A-21
A-52: Frequency: 2.4GHz, $\theta = 90^\circ$	A-21
A-53: Frequency: 2.6GHz, $\theta = 10^\circ$	A-21
A-54: Frequency: 2.6GHz, $\theta = 30^\circ$	A-21
A-55: Frequency: 2.6GHz, $\theta = 60^\circ$	A-22
A-56: Frequency: 2.6GHz, $\theta = 90^\circ$	A-22
A-57: Frequency: 2.8GHz, $\theta = 10^\circ$	A-22
A-58: Frequency: 2.8GHz, $\theta = 30^\circ$	A-22
A-59: Frequency: 2.8GHz, $\theta = 50^\circ$	A-22
A-60: Frequency: 2.8GHz, $\theta = 90^\circ$	A-22
A-61: Frequency: 3.0GHz, $\theta = 10^\circ$	A-23
A-62: Frequency: 3.0GHz, $\theta = 30^\circ$	A-23
A-63: Frequency: 3.0GHz, $\theta = 50^\circ$	A-23
A-64: Frequency: 3.0GHz, $\theta = 80^\circ$	A-23
B-1: Two coordinate systems related by rotation angles α , β , and γ	B-1
B-2: Intuitive rotation for a dipole along the Z-axis	B-4
B-3: Rotation that produces a solution in the unprimed coordinate system	B-5
B-4: Y-directed dipole pattern E_ϕ vs ϕ , with $\theta=45^\circ$	B-7
B-5: Y-directed dipole pattern E_θ vs ϕ , with $\theta=55^\circ$	B-7
B-6: Y-directed dipole pattern E_θ vs θ , with $\phi=30^\circ$	B-7
B-7: Y-directed dipole pattern E_ϕ vs θ , with $\phi=30^\circ$	B-7
B-8: Z-directed bowtie pattern computed in CST.....	B-8
B-9: Y-directed bowtie pattern computed in CST	B-8
B-10: Y-directed bowtie pattern obtained by applying the rotation transform	B-8
C-1: ML Results, 205mm Antennas, 0.5GHz, no mutual coupling, $\alpha = 1^\circ$	C-2
C-2: ML Results, 205mm Antennas, 0.5GHz, no mutual coupling, $\alpha = 10^\circ$	C-2
C-3: ML Results, 205mm Antennas, 0.5GHz, no mutual coupling, $\alpha = 20^\circ$	C-2
C-4: ML Results, 205mm Antennas, 0.5GHz, no mutual coupling, $\alpha = 30^\circ$	C-2
C-5: ML Results, 205mm Antennas, 0.5GHz, no mutual coupling, $\alpha = 40^\circ$	C-2
C-6: ML Results, 205mm Antennas, 0.5GHz, no mutual coupling, $\alpha = 50^\circ$	C-2
C-7: ML Results, 205mm Antennas, 0.5GHz, with mutual coupling, $\alpha = 1^\circ$	C-2
C-8: ML Results, 205mm Antennas, 0.5GHz, with mutual coupling, $\alpha = 10^\circ$	C-2
C-9: ML Results, 205mm Antennas, 0.5GHz, with mutual coupling, $\alpha = 20^\circ$	C-2
C-10: ML Results, 205mm Antennas, 0.5GHz, with mutual coupling, $\alpha = 30^\circ$	C-2
C-11: ML Results, 205mm Antennas, 0.5GHz, with mutual coupling, $\alpha = 40^\circ$	C-2
C-12: ML Results, 205mm Antennas, 0.5GHz, with mutual coupling, $\alpha = 50^\circ$	C-2
C-13: ML Results, 205mm Antennas, 1GHz, no mutual coupling, $\alpha = 1^\circ$	C-3
C-14: ML Results, 205mm Antennas, 1GHz, no mutual coupling, $\alpha = 10^\circ$	C-3

C-58: ML Results, 205mm Antennas, 2.5GHz, with mutual coupling, $\alpha = 30^\circ$	C-6
C-59: ML Results, 205mm Antennas, 2.5GHz, with mutual coupling, $\alpha = 40^\circ$	C-6
C-60: ML Results, 205mm Antennas, 2.5GHz, with mutual coupling, $\alpha = 50^\circ$	C-6
C-61: ML Results, 205mm Antennas, 3GHz, no mutual coupling, $\alpha = 1^\circ$	C-7
C-62: ML Results, 205mm Antennas, 3GHz, no mutual coupling, $\alpha = 10^\circ$	C-7
C-63: ML Results, 205mm Antennas, 3GHz, no mutual coupling, $\alpha = 20^\circ$	C-7
C-64: ML Results, 205mm Antennas, 3GHz, no mutual coupling, $\alpha = 30^\circ$	C-7
C-65: ML Results, 205mm Antennas, 3GHz, no mutual coupling, $\alpha = 40^\circ$	C-7
C-66: ML Results, 205mm Antennas, 3GHz, no mutual coupling, $\alpha = 50^\circ$	C-7
C-67: ML Results, 205mm Antennas, 3GHz, with mutual coupling, $\alpha = 1^\circ$	C-7
C-68: ML Results, 205mm Antennas, 3GHz, with mutual coupling, $\alpha = 10^\circ$	C-7
C-69: ML Results, 205mm Antennas, 3GHz, with mutual coupling, $\alpha = 20^\circ$	C-7
C-70: ML Results, 205mm Antennas, 3GHz, with mutual coupling, $\alpha = 30^\circ$	C-7
C-71: ML Results, 205mm Antennas, 3GHz, with mutual coupling, $\alpha = 40^\circ$	C-7
C-72: ML Results, 205mm Antennas, 3GHz, with mutual coupling, $\alpha = 50^\circ$	C-7
C-73: ML Results, 50mm Antennas, 3GHz, no mutual coupling, $\alpha = 1^\circ$	C-8
C-74: ML Results, 50mm Antennas, 3GHz, no mutual coupling, $\alpha = 10^\circ$	C-8
C-75: ML Results, 50mm Antennas, 3GHz, no mutual coupling, $\alpha = 20^\circ$	C-8
C-76: ML Results, 50mm Antennas, 3GHz, no mutual coupling, $\alpha = 30^\circ$	C-8
C-77: ML Results, 50mm Antennas, 3GHz, no mutual coupling, $\alpha = 40^\circ$	C-8
C-78: ML Results, 50mm Antennas, 3GHz, no mutual coupling, $\alpha = 50^\circ$	C-8
C-79: ML Results, 50mm Antennas, 0.5GHz, with mutual coupling, $\alpha = 1^\circ$	C-9
C-80: ML Results, 50mm Antennas, 0.5GHz, with mutual coupling, $\alpha = 10^\circ$	C-9
C-81: ML Results, 50mm Antennas, 0.5GHz, with mutual coupling, $\alpha = 20^\circ$	C-9
C-82: ML Results, 50mm Antennas, 0.5GHz, with mutual coupling, $\alpha = 30^\circ$	C-9
C-83: ML Results, 50mm Antennas, 0.5GHz, with mutual coupling, $\alpha = 40^\circ$	C-9
C-84: ML Results, 50mm Antennas, 0.5GHz, with mutual coupling, $\alpha = 50^\circ$	C-9
C-85: ML Results, 50mm Antennas, 1GHz, with mutual coupling, $\alpha = 1^\circ$	C-9
C-86: ML Results, 50mm Antennas, 1GHz, with mutual coupling, $\alpha = 10^\circ$	C-9
C-87: ML Results, 50mm Antennas, 1GHz, with mutual coupling, $\alpha = 20^\circ$	C-9
C-88: ML Results, 50mm Antennas, 1GHz, with mutual coupling, $\alpha = 30^\circ$	C-9
C-89: ML Results, 50mm Antennas, 1GHz, with mutual coupling, $\alpha = 40^\circ$	C-9
C-90: ML Results, 50mm Antennas, 1GHz, with mutual coupling, $\alpha = 50^\circ$	C-9
C-91: ML Results, 50mm Antennas, 1.5GHz, with mutual coupling, $\alpha = 1^\circ$	C-10
C-92: ML Results, 50mm Antennas, 1.5GHz, with mutual coupling, $\alpha = 10^\circ$	C-10
C-93: ML Results, 50mm Antennas, 1.5GHz, with mutual coupling, $\alpha = 20^\circ$	C-10
C-94: ML Results, 50mm Antennas, 1.5GHz, with mutual coupling, $\alpha = 30^\circ$	C-10
C-95: ML Results, 50mm Antennas, 1.5GHz, with mutual coupling, $\alpha = 40^\circ$	C-10
C-96: ML Results, 50mm Antennas, 1.5GHz, with mutual coupling, $\alpha = 50^\circ$	C-10
C-97: ML Results, 50mm Antennas, 2GHz, with mutual coupling, $\alpha = 1^\circ$	C-10
C-98: ML Results, 50mm Antennas, 2GHz, with mutual coupling, $\alpha = 10^\circ$	C-10
C-99: ML Results, 50mm Antennas, 2GHz, with mutual coupling, $\alpha = 20^\circ$	C-10
C-100: ML Results, 50mm Antennas, 2GHz, with mutual coupling, $\alpha = 30^\circ$	C-10

Figure	Page
C-144: MUSIC Results, 50mm Ant., 2.5GHz, with mutual coupling, $\alpha = 50^\circ$	C-14
C-145: MUSIC Results, 50mm Ant., 3GHz, with mutual coupling, $\alpha = 1^\circ$	C-14
C-146: MUSIC Results, 50mm Ant., 3GHz, with mutual coupling, $\alpha = 10^\circ$	C-14
C-147: MUSIC Results, 50mm Ant., 3GHz, with mutual coupling, $\alpha = 20^\circ$	C-14
C-148: MUSIC Results, 50mm Ant., 3GHz, with mutual coupling, $\alpha = 30^\circ$	C-14
C-149: MUSIC Results, 50mm Ant., 3GHz, with mutual coupling, $\alpha = 40^\circ$	C-14
C-150: MUSIC Results, 50mm Ant., 3GHz, with mutual coupling, $\alpha = 50^\circ$	C-14

List of Tables

Table	Page
4-1: Parameters of the eight UPWs incident on the tripole	4-2
4-2: Angular difference between known and estimated angles-of-arrival for noise-free case	4-3
4-3: Parameters of the nine UPWs incident on the bowties	4-11
4-4: Parameters of the UPWs incident on the biconical antennas.....	4-14

CHAPTER 1

Direction Finding With Mutually Orthogonal Antennas

1.1 INTRODUCTION

Determining the location of an electromagnetic emitter has been an interest of scientists, engineers, government agencies, and many others for a very long time. Almost as soon as the first radio waves were detectable, people have sought ways to determine the location of the transmitting source. As early as 1904, a scientist and inventor named John S. Stone designed antennas for this purpose and is credited with important pioneering work in the area. Fredrick A. Kolster used a loop antenna during World War I to detect signals for the National Bureau of Standards. During World War II, with the rise of radar and other advanced technologies, pinpointing the location of an emitting source became an important area of work for numerous intelligence agencies on both sides of the conflict. In modern times, estimating the location of signal sources has been used for hunting down illegal radio broadcasts, locating emergency transmitter beacons, navigating sea vessels, and various other military applications [1].

If we think of an electromagnetic emitter placed on the Earth's surface, then the process of estimating the location of that emitter can be thought of in three separate steps. First, the electromagnetic waves from the emitter must be detected. Second, the bearing information of these waves must be estimated. The third step, referred to as geolocation, attempts to use the bearing information from step two (along with other available

information) to approximate the location of the emitter on the Earth's surface. The main topic of this thesis is the second step which will be referred to herein as direction finding (DF) but is also commonly known as direction-of-arrival estimation. We stress that DF is distinct from, but related to, the geolocation problem. In DF we seek to answer, "where did that signal come from?" The geolocation problem, on the other hand, asks "where is the transmitter physically located?" For our work, we want to determine the bearing of the incident electromagnetic signals that, we assume, have already been detected by a receiver (i.e., step one is assumed to have already been accomplished).

The problem of estimating the direction-of-arrival of incident signals has often been solved in the past using large arrays of antennas. These large arrays are needed for creating narrow beam patterns and for satisfying the underlying assumptions associated with advanced DF algorithms such as MUSIC and ESPRIT (see Chapter 2). However, when size and weight restrictions are important, large arrays become impractical. Therefore, interest has grown for research into smaller, light-weight DF systems that could potentially be mounted on unmanned aerial vehicles (UAVs) where size and weight constraints prohibit the use of large antenna arrays. A DF system using a single electric field sensor formed from three mutually orthogonal antennas may fit this need. Figure 1 - 1 demonstrates the proposed arrangement using three dipole antennas, each placed along a coordinate axis.

The idea of using three mutually orthogonal antennas in a DF application was first posed to this author by researchers at the Air Force Research Laboratory (AFRL). After acquiring some DF equipment from an expired contract, the researchers wanted to know if the equipment could be incorporated into a system that uses a mutually orthogonal

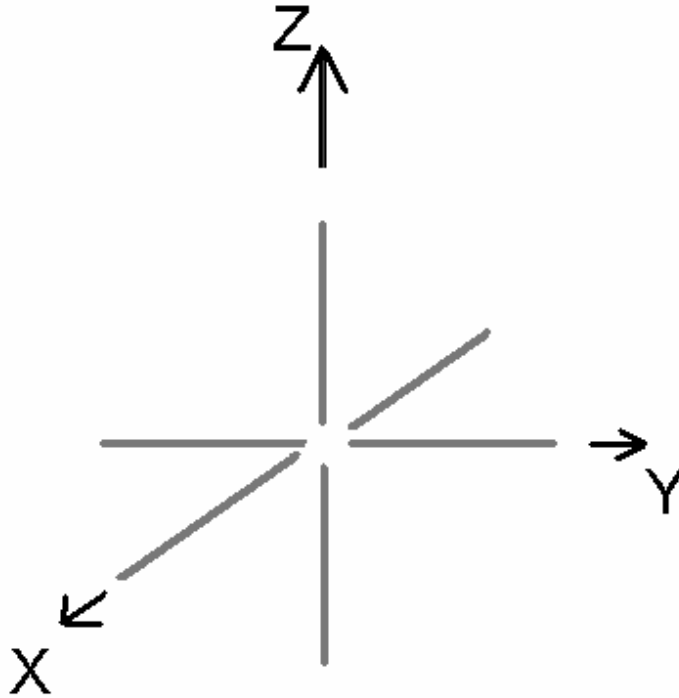


Figure 1 - 1: Mutually orthogonal dipoles

arrangement of antennas. The following section offers more details about this background work which eventually led to the ideas pursued in this thesis. Later in this chapter, we'll qualitatively look at the theoretical difference between using an array of spatially separated antennas and using an arrangement of mutually orthogonal antennas. We'll also discuss some potential benefits of the mutually orthogonal approach.

1.2 BACKGROUND: AFRL CONTRACTED DF WORK

In 2006, AFRL (Radio Frequency Sensor Technology Division) contracted a major aeronautical systems development company to research a DF and geolocation system for UAVs. The system was expected to operate from 30MHz to 3000MHz and to be scalable to fit on a variety of UAV platforms (Dakota, MQ-1 Predator, RQ-4 Global

Hawk, etc). Over the next two and a half years of the contract, the company studied the system requirements and the concept of operations (CONOPS), designed and built a set of wideband antennas, wrote and tested DF and geolocation software, integrated the necessary system hardware and software, and tested the system in an outdoor measurement range on a non-moving Dakota airframe.

Their initial solutions to the DF problem and the geolocation problem were fairly straight forward. The DF portion of their system used a set of six antennas that formed two independent triangular arrays on the underside of the airframe. Their DF algorithm processed the measured phase difference between the array elements. In Chapter 2, this approach will be labeled as a *phase matching* method. The geolocation algorithm they used was based on [2]. Known as the “statistical theory of DF fixing,” this geolocation method uses the lines of bearing from the DF algorithm to approximate an elliptical zone of confidence around the estimated location of the emitter. Since the geolocation portion of their system isn’t the focus of this thesis, the details will not be discussed further.

Unfortunately, the phase matching DF algorithm initially attempted by the contractors had some limiting drawbacks. While they presented a closed-form theoretical formulation of their DF algorithm in the finalized report, they indicated that it only works under ideal circumstances. The ideal case assumes no noise, no unexpected coupling between the antenna elements and the aircraft fuselage, and no multipath reflections. When these ideal conditions are satisfied, the phase measurements on each antenna are directly related to the physical spacing between each antenna and the direction-of-arrival of the incident signal. In the realistic, non-ideal case, multipath reflections and the complicated interaction of the electromagnetic fields between the antennas and the

aircraft fuselage create distortions in the phase relationship which cause their algorithm to fail.

The contractors overcame the phase distortion problems by using a look-up table algorithm. The look-up table algorithm essentially compares the phase differences (amplitude independent) on the six antennas with an extensive set of stored phase difference values that correspond to the direction of the incident wave. The algorithm searches through the table to find the values that correspond to the smallest Euclidian distance between the measured values and the values in the table. Building this table required taking numerous measurements in an outdoor range to compile enough useful data for the various combinations of different frequencies and angles-of-arrival anticipated.

When using the lookup table algorithm, their system was somewhat successful in outdoor stationary measurements and in simulations. In the outdoor measurement range, it had an average accuracy of 2° when determining the direction of a single incident plane wave. The best of the simulations showed that the DF system and the geolocation system, when working together, were able to locate as many as six radio emitters to within an average geolocation error of roughly an acre when measurements were taken from three cooperating airframes equipped with the system.

The stored data in the look-up tables is currently only applicable to the Dakota airframe and only when the antennas are installed in the same location and orientation as when the contractors gathered the data in the tables. While it would be possible to place their system on another aircraft or to rearrange the antennas on the same airframe, this would require taking countless measurements again to recompile the data tables. This

technique isn't as practical as an independent or software definable system that could be placed on any airframe.

When the contract expired in 2009, AFRL received the system hardware and software including six wideband blade antennas (see Figure 1 - 2, also see Appendix A), the finalized DF and geolocation algorithms written in Matlab, and other associated hardware such as matching circuits, receivers, clock generators, etc. Also received was the final report describing the contractors' efforts.

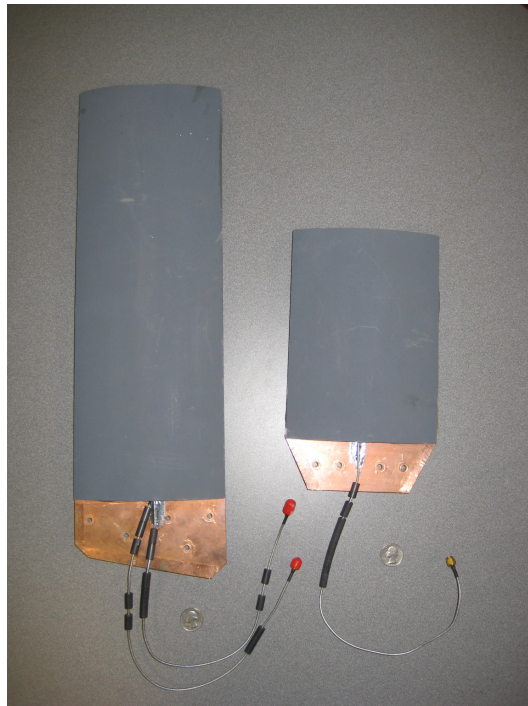


Figure 1 - 2: Wideband antennas

In early 2010, researchers at AFRL/RYRR posed the question of whether it was possible to perform DF using the contractor developed antennas in a mutually orthogonal arrangement instead of the triangular array used by the contractors. The researchers were very interested to know what type of algorithms could be used with such an arrangement.

It was believed that the potential benefits of the mutually orthogonal arrangement would be a more flexible and novel design as well as the ability to determine the polarization of the incident wave.

The researchers agreed to sponsor this thesis work with the eventual goal of developing a three channel DF system summarized by the block diagram of Figure 1 - 3. The receiver section, which includes the tuner and digitizer, is eventually planned to be a state-of-the-art digital software definable receiver known as the DRS Picoceptor which operates from 30MHz-3000MHz, weighs less than a pound, and consumes less than five watts making it an ideal choice for UAV applications. Other researchers at AFRL are currently studying the Picoceptor. This thesis has focused on the antenna and the algorithm blocks in the diagram by investigating this idea of a mutually orthogonal arrangement of antennas to perform DF.

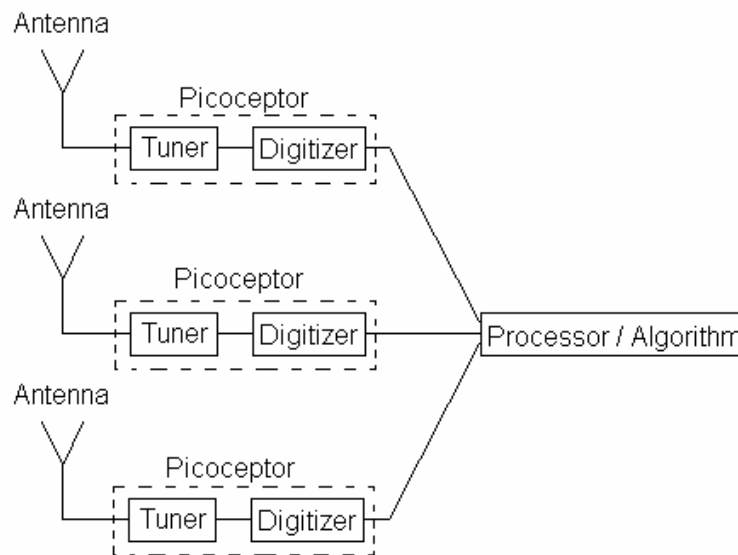


Figure 1 - 3: Block diagram of envisioned DF system using mutually orthogonal antennas

1.3 QUALITATIVE COMPARISON OF DF APPROACHES

This section briefly explains the main difference between using an array of spatially separated antennas and using the proposed arrangement of three mutually orthogonal antennas in a DF application. Many more details are provided in the coming chapters.

To understand the main difference between the two DF approaches, we consider an electromagnetic signal propagating through unbounded free-space. This signal will travel with a known velocity equal to the speed of light. If we measure this signal at two distinct points in space, there will be a phase difference in the measurements due to the finite propagation time as the signal moves from one sensor apparatus to the next. The amount of phase delay is proportional to the array configuration and the direction-of-arrival of the incident signal. The DF problem is typically solved by spatially separating several antennas, thereby forming an array, and then measuring the propagation delay on each antenna element. The measured phase differences are then processed using any of the numerous different known DF algorithms. Indeed, all of the common direction finding methods contained in Chapter 2 will be explained in relation to an array of antennas that measures the propagation phase delay.

Direction finding with a set of three mutually orthogonal antennas is quite different and fairly unconventional. Because the phase center of each antenna is co-located at the same point as the other two antennas, there is no measurable phase difference due to the propagation phase delay. However, going back to our electromagnetic signal propagating through space, we also know, in addition to its travel velocity, that it will have an electric field exhibiting certain polarization properties. This

polarization information is the key to estimating the direction-of-arrival using the orthogonal arrangement. Exploiting this polarization information, instead of the propagation phase delay, is the main difference between the traditional array-based approach and the approach studied in this thesis. It is important to note that the three antennas in the orthogonal arrangement will still measure a phase difference but it is due to the polarization properties of the electric field, not the propagation delay. The next section explains some potential benefits of using this unconventional approach.

1.4 POTENTIAL BENEFITS & IMPACT

Using an arrangement of three mutually orthogonal antennas for DF has some potential advantages over the conventional solution using arrays. For example, when size and weight limitations are important, a system that only needs three antennas is very beneficial. Contrast this with the conventional solution using arrays where it is usually advantageous to incorporate as many antennas as possible to create narrow beam patterns. Another important advantage of the mutually orthogonal arrangement is that, since it relies on measuring the polarization parameters of the incident electric fields, it can potentially extract valuable information about the characteristics of the emitting source for intelligence purposes. Finally, a third important advantage of the mutually orthogonal arrangement is that, when the antenna elements are small compared to wavelength, the system could be essentially frequency independent. As explained by [3], the measurements taken from a mutually orthogonal arrangement of three antennas “ ... contain no time-delay phase factors; that is, [the measurements], unlike those of spatially

displaced arrays, are independent of the impinging signals' frequency spectra ... due to the spatial co-location of the [antennas].”

A DF system of this nature could prove very useful for signal intelligence gathering. If the system is constructed with the Picoceptors as envisioned by the block diagram in Figure 1 - 3, it would offer a wideband record functionality that could be used to listen for, and eventually estimate the location of, hard-to-detect signals such as spread-spectrum, short duration, weak transmissions, or signals hidden inside restricted bands. In addition, the lightweight and small size would provide a valuable DF capability for unmanned aerial vehicles that could expand the signal intelligence gathered from our adversaries, thereby improving the warfighter's ability to engage in conflict.

Before moving to the conclusion, we should mention that there are also several disadvantages to using this arrangement. As will be discussed in the literature review contained in Chapter 2, this arrangement can only estimate, at most, the direction-of-arrival of two incident signals that are operating on the same carrier frequency. Of course, if the signals are on different carrier frequencies, they can be separated in the frequency domain and then processed separately (this is the approach taken in this thesis). Another disadvantage is that the close proximity of the antenna elements to each other will create complicated mutual coupling problems. Mutual coupling with any surrounding support structures such as the airframe or the local ground planes is also possible. In this thesis, the mutual coupling between the antenna elements is accounted for during the simulations in CST Microwave Studio. However, since the antennas are modeled as being completely isolated in free space, no mutual coupling between any external structures will be studied.

1.5 CONCLUSION

A recently expired contract at AFRL has sparked interest in using a set of mutually orthogonal antennas to perform direction finding (DF) of electromagnetic signals. Approaching the DF problem in this way is quite different from how it has typically been accomplished in the past which, in large part, has relied on measuring the propagation phase delay between the elements in an antenna array. The mutually orthogonal arrangement uses the polarization information of the electric field rather than the propagation delay.

In the coming chapters, this thesis will present the study of DF with mutually orthogonal antennas. In Chapter 2, we'll review the conventional methods that have typically been used to approach the DF problem in the past including so-called *super-resolution* techniques such as the maximum likelihood technique and the MUSIC technique. Chapter 2 also contains a literature review on prior DF work with a mutually orthogonal set of antennas. In Chapter 3, we explain the methods that were used to study the DF problem during this thesis. Specifically, we'll review the uniform plane wave model and an antenna concept known as the vector effective height. By combining the vector effective height concept with some of the techniques from Chapter 2, we'll then develop three DF algorithms that can be used with our arrangement of antennas. Chapter 4 presents and discusses the results obtained from applying the algorithms to mutually orthogonal arrangements of dipole, bowtie, and biconical antennas. Finally, Chapter 5 contains closing remarks and a discussion about possible future work.

CHAPTER 2

Common Direction Finding Methods and Literature Review

2.1 INTRODUCTION

This chapter reviews some common direction finding (DF) methods including classic beam forming, phase matching, monopulse, maximum likelihood, MUSIC, and ESPRIT. Although, each method is explained in relation to the conventional DF approach using spatially separated antennas, reviewing these common methods is important since they are often encountered in the literature and because a few of them will be adapted to the mutually orthogonal arrangement in the next chapter. This chapter also contains a literature review on prior DF work with mutually orthogonal antennas. As a starting point, the next section introduces some basic concepts which will be utilized when explaining the common DF methods.

2.2 BASIC CONCEPTS & THE NARROWBAND SIGNAL MODEL

Before presenting a review of the different DF methods, it's essential to start with some basic concepts. This section describes the narrowband signal model that is a basic assumption for all of the DF methods described later. The narrowband signal model says that we can treat the baseband signal received on each antenna element as being identical,

but time shifted and magnitude scaled, versions of the original baseband signal. The development of the narrowband signal model that follows is based on the discussion presented in [4].

Let a transmitted signal from an emitter be given by $s(t) \cdot e^{j \omega_c t}$ where $s(t)$ is the baseband signal and $\omega_c = 2\pi f_c$ is the angular frequency of the modulating carrier. When the signal is received by an M -element linear array of antennas, each antenna will detect the signal at a slightly different time due to the spacing between the array elements and the angle γ_0 between the normal of the array face and the incident wave (see Figure 2 - 1).

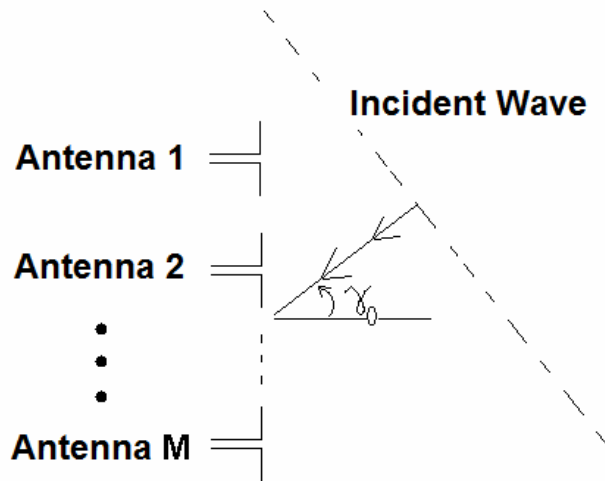


Figure 2 - 1: Linear array with incident wave

The vector of the received signal is

$$\vec{x}_{rec}(t) = \begin{bmatrix} s(t - \tau_1) \cdot e^{j \omega_c (t - \tau_1)} \\ s(t - \tau_2) \cdot e^{j \omega_c (t - \tau_2)} \\ \vdots \\ s(t - \tau_M) \cdot e^{j \omega_c (t - \tau_M)} \end{bmatrix} \quad (2-1)$$

where $\tau_m = -(d_m/c) \cdot \sin(\gamma_0)$ with d_m being the distance from a reference point on the antenna to the m^{th} array element ($1 \leq m \leq M$) and c is the speed of light. After demodulating \vec{x}_{rec} , we get the baseband signal given by

$$\vec{x}(t) = \begin{bmatrix} s(t - \tau_1) \cdot e^{j\omega_c \tau_1} \\ s(t - \tau_2) \cdot e^{j\omega_c \tau_2} \\ \vdots \\ s(t - \tau_M) \cdot e^{j\omega_c \tau_M} \end{bmatrix} \quad (2-2)$$

The narrowband signal approximation assumes that the delay in the baseband signal is negligible, meaning $s(t - \tau_m) \approx s(t)$. The reasoning follows. Let D be the aperture size of the array which is defined as the distance between the two end elements in the array. If D is measured in carrier wavelengths λ_c , then the longest time delay between the time when the wave front hits the first antenna and the time that it hits the last antenna element in the array is at most D/f_c seconds. Now, if we label the bandwidth of the baseband signal as B , and we assume that B is very narrowbanded ($B \ll f_c/D$), then we can approximate the baseband signal delay $\tau_m = 0$ for each antenna element. This is analogous to the ‘‘lumped parameter’’ model in circuit theory which allows us to treat all elements of the circuit as existing in the same location when the operating wavelength is much greater than the size of the circuit [5].

Using the narrowband approximation for the baseband signal, (2-2) becomes

$$\vec{x}(t) \approx \begin{bmatrix} s(t) \cdot e^{j\omega_c \tau_1} \\ s(t) \cdot e^{j\omega_c \tau_2} \\ \vdots \\ s(t) \cdot e^{j\omega_c \tau_M} \end{bmatrix} = s(t) \begin{bmatrix} e^{j\omega_c \tau_1} \\ e^{j\omega_c \tau_2} \\ \vdots \\ e^{j\omega_c \tau_M} \end{bmatrix} \quad (2-3)$$

This approximation, valid for $B \ll f_c/D$, is known as the narrowband signal approximation. From this approximation, we define an array manifold $\vec{a}(\theta_0)$ given by

$$\vec{a}(\theta_0) = \begin{bmatrix} e^{j\theta_0 d_1} \\ e^{j\theta_0 d_2} \\ \vdots \\ e^{j\theta_0 d_M} \end{bmatrix} = \begin{bmatrix} e^{-j\theta_0 d_1 \sin(\theta_0)/c} \\ e^{-j\theta_0 d_2 \sin(\theta_0)/c} \\ \vdots \\ e^{-j\theta_0 d_M \sin(\theta_0)/c} \end{bmatrix} \quad (2-4)$$

which is the response of the antenna array to a unit amplitude signal $s(t) = 1$.

Lastly, the complete received signal, when using this narrowband approximation model, is given by

$$\vec{y}(t) = s(t)\vec{a}(\theta_0) + \vec{v}(t) \quad (2-5)$$

where $\vec{v}(t)$ is a multivariate complex Gaussian noise vector with uncorrelated elements having zero mean and variance of σ^2 . If the signal is sampled at discrete moments in time for use by a digital processor, then we simply replace the time t with k which denotes the index of the sampled signal. The narrowband signal model is an important analytical assumption that holds true for many practical signals and forms the foundation for reviewing the common DF methods which are discussed in the next section.

2.3 REVIEW OF COMMON DF METHODS

There are numerous DF methods used in modern DF systems. This section is intended to provide a brief overview of the basic features of three commonly used methods known as classic beam forming, monopulse, and phase matching. As explained in [4], “In the absence of noise and practical imperfections, [each of these] method[s] provides a perfect estimate of the direction of [a single] incident wave.” However, there

are two problems. The first problem occurs when trying to estimate the direction-of-arrival (DOA) of two or more co-channel emitters that are spatially separated. The second problem involves a single emitting source that undergoes multipath propagation. In either case, there will be several incident waves operating on the same carrier frequency that arrive at the receiving antenna from different directions. These two problems can significantly degrade the resolvability of the system (i.e., the ability to determine how many emitters are detected) and accuracy of the direction estimates. To solve the problem of multiple co-channel emitters and multipath reflections, more advanced techniques are needed to process the received signals. The more advanced techniques, discussed later in section 2.4, are referred to as maximum likelihood, MUSIC, and ESPRIT. Each of these advanced techniques can be used with any of the three basic DF methods under certain constraints which will be discussed below.

Classic Beam Forming

Classic beam forming can be thought of as a delay-and-sum method. The idea is to delay the received signal in each array element by an appropriate amount and then sum up the result from each element. If the delays have been chosen correctly, the signal on each element will *line up* coherently so that adding them produces a larger amplitude result (larger signal-to-noise ratio). An incorrect delay to each element would cause a smaller response (smaller signal-to-noise ratio) since one or more elements would be adding destructively to the end result.

Assuming the narrowband model applies (see section 2.2), the digitally sampled received signal on each array element is given by (2-5) with t replaced by the sample

index k . When the delays are applied to each element, the array will be looking in the γ direction and will measure a received power of

$$p(\gamma, k) = \left| \vec{W}(\gamma)^H \vec{y}(k) \right|^2 \quad (2-6)$$

where $\vec{W}(\gamma)$ is a weight factor that allows for control of the array sidelobes using an appropriate windowing function and the superscript $(\bullet)^H$ is the Hermitian transpose. The delays that cause (2-6) to be maximized will indicate the direction γ_0 of the incoming wave. An algorithm for using the classical beam forming method would simply vary the delays in each antenna element to steer the beam until a maximum is found. See [6] for more on steering the beam of an antenna array.

When a beamformer is used and there are two co-channel emitters inside the beam, the beamforming method can not distinguish between the two transmitters and instead estimates the midpoint between the two transmitters. This is one of the main drawbacks to the beam forming method. One solution is to use a large array to obtain a very narrow beam thereby reducing the chance that more than one co-channel emitters is inside the beam. If a large array is not possible, then we need to use the more advanced processing techniques discussed later in section 2.4.

Monopulse

Another common direction finding method is known as monopulse. This method is also used extensively in radar tracking applications. The idea is to compare the difference between the received signal powers on two separate antennas that are pointed

in slightly different directions. The antennas could be arrays or just two individual antennas as long as they have some known directivity.

Let γ_0 be the true direction of the emitter. If we let Δ be the difference between the directions that the two antennas are pointing and let γ be the midpoint between them, then the first antenna is pointed at $(\gamma + \Delta/2)$ and the second antenna is pointed at $(\gamma - \Delta/2)$. The monopulse response is given by

$$b(\gamma) = \frac{1}{\Delta} \left[p_1 \left(\gamma + \frac{\Delta}{2} \right) - p_2 \left(\gamma - \frac{\Delta}{2} \right) \right] \quad (2-7)$$

where $p_1(\bullet)$ and $p_2(\bullet)$ are the received powers given by (2-6) for each antenna and $1 / \Delta$ is a normalization factor. Once a signal has been detected, a system using monopulse tries to keep the received power in both antennas equal thereby keeping $b(\gamma) \approx 0$, which suggests $\gamma \approx \gamma_0$.

Phase Matching

The last of the three basic DF methods is known as phase matching. The basic idea with this method is to ignore the amplitude component of the received signal and rely entirely on the phase information received on each antenna due to the propagation delay. In doing so, it is possible to reduce the negative effects inherent with amplitude measurements such as unmatched antennas and amplifier gain issues.

Assuming a single, narrowband, monochromatic plane wave is incident on the antenna array, we let $\vec{\phi}(k)$ represent the vector of phase measurements on the antennas for a single snapshot in time. For the same snapshot in time, let $\vec{\phi}(\gamma)$ represent the phases of the array manifold given by

$$\vec{\gamma}(k) = \begin{bmatrix} d_1 \sin(\gamma(k)) / c \\ d_2 \sin(\gamma(k)) / c \\ \vdots \\ d_M \sin(\gamma(k)) / c \end{bmatrix} \quad (2-8)$$

The direction of the incident wave, γ_0 , is calculated by finding the $\gamma(k)$ that minimizes the difference between the measured phases in $\tilde{\gamma}(k)$ and the assumed phases in $\vec{\gamma}(k)$. In other words, we minimize the squared norm of the difference given by

$$d(k) = \left\| \tilde{\gamma}(k) - \vec{\gamma}(k) \right\|^2 \quad (2-9)$$

Since the actual phase on any received antenna is an unknown phase delay τ_m from the original emitter signal $s(t) \cdot e^{j \omega t}$, a typical practice is to measure the relative phases instead of the absolute phase by assigning one of the antennas to have *zero phase*. This antenna is the phase reference of the antenna array and all other phase measurements are subtracted from the phase on the reference. In [4], the authors offer another approach to account for the unknown phase delay. Their method is to include an additional unknown phase term in (2-9) and then simultaneously estimate the unknown direction γ_0 and the unknown additional phase term.

2.4 DF PROCESSING ON MULTIPLE CO-CHANNEL EMITTERS

If we assume no noise or other practical imperfections, then the three methods presented in the previous section provide perfect estimates for the incident direction of a single, narrowband, monochromatic plane wave. The situation becomes more complicated when there are multiple waves incident on the receiving antenna either due to multipath effects or from multiple emitters operating at the same frequency (i.e., co-

channel emitters). As pointed out in [4], if these co-channel emitters are spatially separated by more than a beamwidth, then the three methods of the previous section will in fact be able to resolve (i.e., the ability to determine how many emitters are detected) the different emitters. However, when the emitters are spaced closer than a beamwidth apart, the resolvability and accuracy of the direction estimates becomes degraded and simply inaccurate.

To solve the problem of multiple co-channel emitters and multipath reflections, more advanced techniques are needed to process the received signals. These so-called “super-resolution” techniques provide the ability to resolve the direction of the incident waves even if they are less than a beamwidth apart. This section discusses the basic ideas behind three of the most common advanced techniques referred to as the maximum likelihood technique, the MUSIC technique, and the ESPRIT technique. Each of these advanced techniques can be used with any of the three basic direction finding methods but are explained below assuming they are implemented with a classic beam forming method.

The Maximum Likelihood Technique

Consider, for a moment, a single incident wave striking the receiving antenna as shown in Figure 2 - 1. Also, recall that we have labeled the angle at which the antenna is looking as γ and the angle of the incident wave as γ_0 . The basic idea with maximum likelihood is to search through all possible look angles γ until we find the value that *most likely* produced the observed signal $\bar{y}(t)$. The classic beam forming method, discussed in section 2.3, is in fact a simplified case of the maximum likelihood technique when only

one wave is incident on the antenna array and the noise is additive white Gaussian noise (AWGN). When there are n incident signals operating at the same frequency (i.e., n co-channel emitters), the maximum likelihood technique would need to search through all combinations of possible values of $\gamma_0, \gamma_1, \dots, \gamma_n$ to find the set that most likely produced the observed signal $\bar{y}(t)$. To use the maximum likelihood technique, we must know the underlying probability density function of the parameters being estimated [7: 315]. For the mathematical formulation that follows, we assume all random variables are independent and follow a Gaussian distribution.

For clarity of demonstrating the basic mathematical formulation of the maximum likelihood technique, let us consider only three incident co-channel signals. Suppose we have measured the received signal $\bar{y}(k)$ on our M -element antenna array for a single snapshot at time k . Modifying (2-5) to incorporate the three incident signals, the $M \times 1$ received signal vector is written as

$$\bar{y}(k) = s_0(k) \cdot \bar{a}(\gamma_0) + s_1(k) \cdot \bar{a}(\gamma_1) + s_2(k) \cdot \bar{a}(\gamma_2) + \bar{v}(k) \quad (2-10)$$

where all terms were defined in section 2.2. Since we are assuming that the noise follows a Gaussian distribution, then $\bar{y}(k)$ is also Gaussian, and the maximum likelihood technique is equivalent to a non-linear least squares problem (proof given in [4]). This least squares problem seeks to find the best possible values of the six quantities $s_0(k)$, $s_1(k)$, $s_2(k)$, γ_0 , γ_1 , and γ_2 so as to minimize the arbitrarily named function g given by

$$g = \left\| \bar{y}(k) - \{s_0(k) \cdot \bar{a}(\gamma_0) + s_1(k) \cdot \bar{a}(\gamma_1) + s_2(k) \cdot \bar{a}(\gamma_2)\} \right\|^2 \quad (2-11)$$

Before we can solve (2-11), we need to begin by working first with (2-10). If we define an $M \times 3$ matrix containing the array manifold vectors as

$\mathbf{A}(a_0, a_1, a_2) = [\vec{a}(a_0) \ \vec{a}(a_1) \ \vec{a}(a_2)]$ then we can rewrite (2-10) without the noise term as

$$\vec{y}(k) = [\vec{a}(a_0) \ \vec{a}(a_1) \ \vec{a}(a_2)] \begin{bmatrix} s_0(k) \\ s_1(k) \\ s_2(k) \end{bmatrix} = \mathbf{A}(a_0, a_1, a_2) \begin{bmatrix} s_0(k) \\ s_1(k) \\ s_2(k) \end{bmatrix} = \vec{y}(k) \quad (2-12)$$

which is now in the recognizable form $\mathbf{A}\vec{s} = \vec{y}$. Since \mathbf{A} is $M \times 3$, it will not have an inverse in general. Therefore, from [8], the best estimate of the signal vector is found by taking

$$\begin{bmatrix} s_0(k) \\ s_1(k) \\ s_2(k) \end{bmatrix} = (\mathbf{A}^H \mathbf{A})^{-1} \mathbf{A}^H \vec{y}(k) \quad (2-13)$$

where $(\bullet)^H$ denotes a Hermitian transpose. Substituting (2-12) and (2-13) into (2-11) we obtain

$$\begin{aligned} g &= \left\| \vec{y}(k) - \left\{ \mathbf{A}(a_0, a_1, a_2) \begin{bmatrix} s_0(k) \\ s_1(k) \\ s_2(k) \end{bmatrix} \right\} \right\|^2 \\ &= \left\| \vec{y}(k) - \left\{ \mathbf{A}(a_0, a_1, a_2) (\mathbf{A}^H \mathbf{A})^{-1} \mathbf{A}^H \vec{y}(k) \right\} \right\|^2 \end{aligned} \quad (2-14)$$

Notice that the matrix $\mathbf{A}(\mathbf{A}^H \mathbf{A})^{-1} \mathbf{A}^H$ is $M \times M$ and is *acting* on $\vec{y}(k)$. From studies in linear algebra [8: 162-166], we recognize this as a projection matrix that projects the vector $\vec{y}(k)$ onto the subspace spanned by the columns of \mathbf{A} (i.e., the column space of \mathbf{A} denoted $C(\mathbf{A})$). Since this is a projection, we use the letter \mathbf{P} to label the projection matrix as $\mathbf{P} = \mathbf{A}(\mathbf{A}^H \mathbf{A})^{-1} \mathbf{A}^H$. Then, factoring out the $\vec{y}(k)$ in (2-14) we get

$$g = \left\| (\mathbf{I} - \mathbf{P}) \vec{y}(k) \right\|^2 \quad (2-15)$$

where \mathbf{I} is the $m \times m$ identity matrix. The trick here is to recall, again from linear algebra, that $\mathbf{I} - \mathbf{P}$ is in fact another projection matrix that projects $\bar{\mathbf{y}}(k)$ onto the null-space of \mathbf{A}^H , denoted $N(\mathbf{A}^H)$ which, from the fundamental theorem of linear algebra, is equal to the orthogonal complement of $C(\mathbf{A})$ (i.e., $N(\mathbf{A}^H) = C(\mathbf{A})^\perp$). Therefore, the final step is to label $\mathbf{P}^\perp = \mathbf{I} - \mathbf{P}$ and perform some standard linear algebra math to obtain

$$\begin{aligned}
 g &= \|\mathbf{P}^\perp \bar{\mathbf{y}}(k)\|^2 \\
 &= (\mathbf{P}^\perp \bar{\mathbf{y}}(k))^H (\mathbf{P}^\perp \bar{\mathbf{y}}(k)) \\
 &= \bar{\mathbf{y}}^H(k) (\mathbf{P}^\perp)^H \mathbf{P}^\perp \bar{\mathbf{y}}(k) \\
 &= \bar{\mathbf{y}}^H(k) \mathbf{P}^\perp \bar{\mathbf{y}}(k)
 \end{aligned} \tag{2-16}$$

In the last step above, we are using the fact that any projection matrix is equal to its transpose and its square (i.e., $\mathbf{P} = \mathbf{P}^H = \mathbf{P}^2$) [8: 164].

In our case, minimizing (2-16) requires a 3-dimensional numeric search for the best combination of angles γ_0 , γ_1 , and γ_2 . In general, an n -dimensional brute-force search would be required for the n incident waves. Since the search is typically only accomplished for discrete values of γ_0 , γ_1 , and γ_2 , further refinement is obtained by interpolation.

There are several attractive features of the maximum likelihood technique. One feature is that, theoretically, you could obtain an estimate for the direction of $\gamma_0, \gamma_1, \dots, \gamma_n$ by taking only a single snapshot of the received signal and using (2-16). If additional snapshots are available and the noise is independent over time, then (2-16) becomes a sum of the g -values computed for each of the K snapshots to yield

$$g = \sum_{k=1}^K \bar{\mathbf{y}}^H(k) \mathbf{P}^\perp \bar{\mathbf{y}}(k) \tag{2-17}$$

Another attractive feature is that the technique is *asymptotically efficient* meaning its accuracy at pinpointing the correct $\gamma_0, \gamma_1, \dots, \gamma_n$ approaches the Cramer Rao Bound as the signal-to-noise ratio approaches infinity [4].

There are several drawbacks to this technique as well. The need to perform this numeric search is computationally expensive and may require more computation time than is desired for a practical, real-time system. Another drawback is that we must know a priori how many signals are expected in the environment at the specified frequency before processing the returns. For example, suppose there were only two incident signals but we mistakenly *tell* the algorithm to look for three. The maximum likelihood algorithm would still report the three values of γ_0, γ_1 , and γ_2 that minimize g in (2-16). Many researchers have suggested ways to reduce these problems (see [4: 25]), but a discussion of their work is beyond our purpose here which was merely to outline the essential idea behind the basic maximum likelihood technique.

It may be apparent to the astute reader that the development of the maximum likelihood technique ignores the eigenstructure inherent in the model. This observation is precisely the motivation for the development of the MUSIC technique which is discussed next.

The MUSIC Technique

The **Multi-Signal Classification**, or MUSIC, technique uses linear algebra and statistics concepts to exploit the eigenstructure of the sample covariance matrix of the received data. The basic idea is to decompose the covariance matrix using singular value decomposition and then use the orthogonality between the signal and noise subspaces to

form a so-called “MUSIC spectrum” which indicates the directions of the incident signals.

Before going into the mathematical formulation, it’s important to understand that the MUSIC technique (and other subspace-based algorithms) relies on several important assumptions. First, the number of incident co-channel signals cannot exceed the number of array elements. Second, the noise is assumed to be white Gaussian noise with zero mean and variance of σ^2 . Third, the number of total snapshots of data must be larger than the number of elements in the antenna array. Lastly, the incident signals must be non-coherent with each other (i.e., the signals are not due to multipath reflections from a common source) and must have zero mean and positive semi-definite covariance matrixes. If these assumptions are not satisfied, the MUSIC technique will not be able to resolve multiple co-channel targets and could produce erroneous DOA estimates. In addition, the MUSIC method is not as optimal as the maximum likelihood technique, but it is much more practical because of the reduced computational cost [4].

To demonstrate the basic mathematical formulation, we again consider only three co-channel signals incident on the M -element antenna array of Figure 2 - 1. Writing (2-5) in matrix form for a single snapshot of the three incident signals at time k we obtain

$$\vec{y}(k) = \begin{bmatrix} y_1(k) \\ y_2(k) \\ \vdots \\ y_M(k) \end{bmatrix} = \mathbf{A} \begin{pmatrix} s_0(k) \\ s_1(k) \\ s_2(k) \end{pmatrix} + \vec{v}(k) = \mathbf{A}\vec{s} + \vec{v} \quad (2-18)$$

Assume now that we have collected a total of K snapshots of the received signal. The data will now need to be represented by a matrix where we place the data from the 1st snapshot in the 1st column, the data in the 2nd snapshot in the 2nd column, etc, as follows

$$\mathbf{y} = \begin{bmatrix} y_1(1) & y_1(2) & \cdots & y_1(K) \\ y_2(1) & y_2(2) & \cdots & y_2(K) \\ \vdots & \vdots & \ddots & \vdots \\ y_M(1) & y_M(2) & \cdots & y_M(K) \end{bmatrix} = \begin{bmatrix} \bar{y}_1^T \\ \bar{y}_2^T \\ \vdots \\ \bar{y}_M^T \end{bmatrix} \quad (2-19)$$

Doing the same to the right side of (2-18) we obtain

$$\mathbf{y} = \mathbf{A} \begin{pmatrix} s_0 \\ s_1 \\ s_2 \end{pmatrix} + \begin{bmatrix} v_1(1) & v_1(2) & \cdots & v_1(K) \\ v_2(1) & v_2(2) & \cdots & v_2(K) \\ \vdots & \vdots & \ddots & \vdots \\ v_M(1) & v_M(2) & \cdots & v_M(K) \end{bmatrix} \quad (2-20)$$

which can be conveniently written as

$$\mathbf{y} = \mathbf{A}\mathbf{s} + \mathbf{v}. \quad (2-21)$$

The covariance matrix for the received data, denoted \mathbf{R}_y , is obtained by taking the statistical expected value of the matrix product $\mathbf{y}\mathbf{y}^H$ which gives

$$\mathbf{R}_y = E[\mathbf{y}\mathbf{y}^H] = E[(\mathbf{A}\mathbf{s} + \mathbf{v})(\mathbf{A}\mathbf{s} + \mathbf{v})^H] \quad (2-22)$$

If we perform basic linear algebra we find

$$\begin{aligned} \mathbf{R}_y &= E[\mathbf{y}\mathbf{y}^H] = E[(\mathbf{A}\mathbf{s} + \mathbf{v})(\mathbf{A}\mathbf{s})^H + \mathbf{v}\mathbf{v}^H] \\ &= E[(\mathbf{A}\mathbf{s} + \mathbf{v})(\mathbf{s}^H \mathbf{A}^H + \mathbf{v}^H)] \\ &= E[(\mathbf{A}\mathbf{s} + \mathbf{v})(\mathbf{s}^H \mathbf{A}^H) + (\mathbf{A}\mathbf{s} + \mathbf{v})\mathbf{v}^H] \\ &= E[\mathbf{A}\mathbf{s}\mathbf{s}^H \mathbf{A}^H + \mathbf{v}\mathbf{s}^H \mathbf{A}^H + \mathbf{A}\mathbf{s}\mathbf{v}^H + \mathbf{v}\mathbf{v}^H] \end{aligned} \quad (2-23)$$

Applying well known rules for expected values we can reduce (2-23) further to obtain

$$\begin{aligned}
\mathbf{R}_y &= E[\mathbf{y}\mathbf{y}^H] = E[\mathbf{A}\mathbf{s}\mathbf{s}^H\mathbf{A}^H] + E[\mathbf{v}\mathbf{s}^H\mathbf{A}^H] + E[\mathbf{A}\mathbf{s}\mathbf{v}^H] + E[\mathbf{v}\mathbf{v}^H] \\
&= \mathbf{A}\mathbf{s}\mathbf{s}^H\mathbf{A}^H + E[\mathbf{v}]\mathbf{s}^H\mathbf{A}^H + \mathbf{A}\mathbf{s}E[\mathbf{v}^H] + E[\mathbf{v}\mathbf{v}^H] \\
&= \mathbf{A}\mathbf{s}\mathbf{s}^H\mathbf{A}^H + E[\mathbf{v}\mathbf{v}^H] \\
&= \mathbf{A}\mathbf{s}\mathbf{s}^H\mathbf{A}^H + \sigma^2\mathbf{I}
\end{aligned} \tag{2-24}$$

where σ^2 is the variance of the noise. The result shown in (2-24) has brought us to the starting point of many published papers on the MUSIC algorithm including [9], [10], and [11]. Now, we want to exploit the eigenstructure in the Hermitian matrix $\mathbf{A}\mathbf{s}\mathbf{s}^H\mathbf{A}^H$.

Therefore, we perform a singular value decomposition on $\mathbf{A}\mathbf{s}\mathbf{s}^H\mathbf{A}^H$ to get [4] [8]

$$\mathbf{R}_y = \mathbf{U}\mathbf{\Sigma}\mathbf{U}^H + \sigma^2\mathbf{I}. \tag{2-25}$$

The matrix \mathbf{U} contains eigenvectors of $(\mathbf{A}\mathbf{s}\mathbf{s}^H\mathbf{A}^H)^2$ and the matrix $\mathbf{\Sigma}$ contains the singular values (square roots of the non-zero eigenvalues) of $\mathbf{A}\mathbf{s}\mathbf{s}^H\mathbf{A}^H$. We can partition the matrix \mathbf{U} into

$$\mathbf{U} = [\mathbf{U}_s, \mathbf{U}_n] \tag{2-26}$$

with the columns of \mathbf{U}_s spanning the so-called ‘‘signal subspace’’ and the columns of \mathbf{U}_n spanning the ‘‘noise subspace.’’ In our example case, we have three incident signals so the $M \times 3$ submatrix \mathbf{U}_s contains the singular vectors associated with the three largest singular values in $\mathbf{\Sigma}$. The $M \times (M-3)$ submatrix \mathbf{U}_n contains the rest of \mathbf{U} .

Mathematically, the subspace \mathbf{U}_s is the column space of $\mathbf{A}\mathbf{s}\mathbf{s}^H\mathbf{A}^H$ (again, denoted $C(\mathbf{A}\mathbf{s}\mathbf{s}^H\mathbf{A}^H)$) while the subspace \mathbf{U}_n is the null-space of $(\mathbf{A}\mathbf{s}\mathbf{s}^H\mathbf{A}^H)^H = \mathbf{A}\mathbf{s}\mathbf{s}^H\mathbf{A}^H$ (denoted $N(\mathbf{A}\mathbf{s}\mathbf{s}^H\mathbf{A}^H)$). Since the signal and noise subspaces are orthogonal by the fundamental theorem of linear algebra [9], vectors spanning the noise subspace will also

be orthogonal to the array manifold evaluated at the signal directions (i.e., $\vec{a}(\theta_i)$ for $i = 0, 1, 2$ in our case of three signals). Therefore, we arrive at the MUSIC spectrum by evaluating

$$S(\theta) = \frac{1}{|\vec{a}^H(\theta)\mathbf{U}_n|^2} \quad (2-27)$$

which will have sharp peaks at the incident directions θ since the denominator evaluates to zero (or nearly zero when we consider noise) at those locations.

The MUSIC algorithm is based on estimating the covariance of the received data since, in practice, we don't know \mathbf{R}_y but we can obtain an estimate (denoted with the hat character ^ in this context) by taking

$$\hat{\mathbf{R}}_y = \frac{1}{K} \sum_{k=1}^K \bar{y}(k)\bar{y}(k)^H = \frac{1}{K} \mathbf{y}\mathbf{y}^H \quad (2-28)$$

We then perform the singular value decomposition on $\hat{\mathbf{R}}_y$ to get

$$\hat{\mathbf{R}}_y = \hat{\mathbf{U}}\hat{\Sigma}\hat{\mathbf{U}}^H \quad (2-29)$$

where $\hat{\mathbf{U}} = [\hat{\mathbf{U}}_s, \hat{\mathbf{U}}_n]$. Lastly, the estimated MUSIC spectrum becomes

$$\hat{S}(\theta) = \frac{1}{|\vec{a}^H(\theta)\hat{\mathbf{U}}_n|^2} \quad (2-30)$$

To obtain a good estimate, we need to take many samples of the incoming signal. In contrast, the maximum likelihood technique only needs one sample (in theory) to give an estimate of the signal directions-of-arrival. Therefore, MUSIC would be a poor choice for detecting very short-duration signals.

The computational advantage that (2-27) provides over (2-17) from the maximum likelihood technique is that (2-27) only needs to search through the angles γ once whereas (2-17) must perform the search for each snapshot. One may wonder if it is possible to determine the directions-of-arrival without performing a search at all. Indeed, so-called search-free techniques have been developed. The ESPRIT technique, discussed in the next section, is one such search-free technique that is a popular choice for real time applications.

The ESPRIT Technique

The acronym ESPRIT is short for **E**stimation of **S**ignal **P**arameters via **R**otational **I**nvariance **T**echnique [12]. ESPRIT is a sub-space technique that does not require a computationally expensive search for the incident angles γ . Compared to the maximum likelihood technique which performs a computationally intensive brute-force search and the MUSIC technique which performs a less intensive search, the ESPRIT technique offers advantages for real time DF applications because it is fast. However, the basic ESPRIT technique can only be used with very specific geometries of the antenna array. Namely, it can only be used when the array is made of two identical and identically oriented subarrays [4]. A generalized ESPRIT technique has been proposed by [13] that reduces the restriction on the array configuration. The authors of [14] have also offered a modified ESPRIT-based algorithm that uses a single “vector sensor” antenna (defined in section 2.5).

Much of the mathematical formulation of ESPRIT is similar to the MUSIC algorithm already discussed. The major difference is that the ESPRIT technique has two

sets of data, one for each subarray, that are related through a rotation operator matrix. The ESPRIT technique takes advantage of the “rotational invariance” between the two data sets. Since the ESPRIT technique won’t be used further in this thesis, and because the mathematical formulation offers no additional insight into the math needed for later work, we will skip the details here. The interested reader is referred to [12] for an easy to understand explanation of the technique.

The three techniques described in this section (maximum likelihood, MUSIC, and ESPRIT) are commonly encountered in the DF literature when attempting to estimate the DOA of multiple co-channel emitters. A basic familiarity of each should aid in understanding the material in the next section which examines pertinent literature on DF using orthogonal antennas.

2.5 LITERATURE REVIEW: DF WITH ORTHOGONAL ANTENNAS

The goal of this literature search has been to identify prior work on mutually orthogonal antennas for use in DF applications. One example of a mutually orthogonal antenna arrangement is a set of three short dipole antennas placed along the x, y, and z coordinate axes as shown in Figure 2 - 2. Some authors, such as [14] and [15], have used the term “tripole” to describe this antenna configuration. The tripole is studied here since it closely resembles the desired arrangement using the wideband antennas described in Chapter 1 (also see Appendix A). (Note: At least one author has used the term “tripole” to describe an entirely different antenna configuration consisting of three coplanar monopoles angled 120° apart [16]. In this thesis, the term tripole will be used to refer to the arrangement shown in Figure 2 - 2.)

The tripole arrangement has at least one significant disadvantage. With the dipoles all centered at the same location, there is no phase shift between the elements due to the propagation delay. Therefore, the methods described in the preceding sections

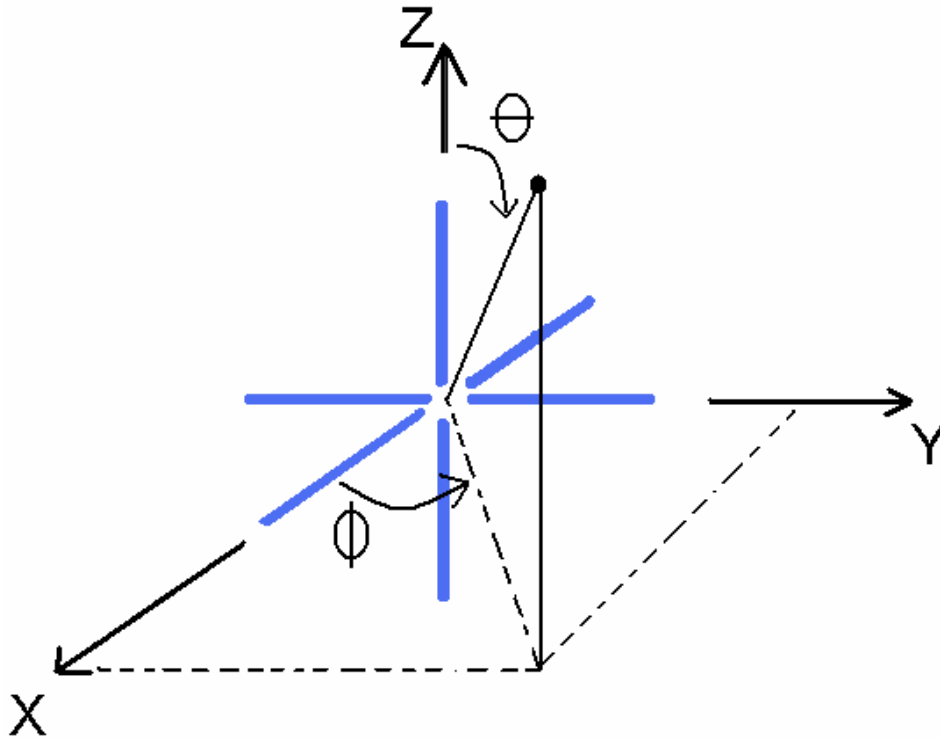


Figure 2 - 2: Three mutually orthogonal dipoles (tripole) with coordinate convention

cannot be applied directly since they relied heavily on the array manifold formed from these phase delays. The possible advantages of the tripole arrangement should become clear, however, as we proceed through the literature review. (Note that there is still a phase difference between antenna elements that is due to the polarization properties of the incident electric fields.)

The tripole under study here appears to be one special case of a “vector sensor” antenna; a term coined by Nehorai and Paldi in their extensively cited article [17]. A vector sensor is any antenna, or set of antennas, “whose output is a vector corresponding

to the complete electric and magnetic fields at the sensor.” Nehorai and Paldi describe how vector sensors, because they measure the complete electromagnetic field at the sensor, can be used to locate the direction of the source by taking the cross product of the electric and magnetic vector components (i.e., obtaining the Poynting vector). The mutually orthogonal arrangement of dipoles is a special case because it provides only the electric, not magnetic, vector components. The reason for this is because each dipole, being linearly polarized along their respective axis, only receives one component of the incident electric field. If we were to add mutually orthogonal loop antennas to each axis, a complete vector sensor could be formed [17]. Two other vector sensor configurations using several dipoles, monopoles, and loop antennas are given in [18] and [19].

Before we place more attention on the tripole, it’s appropriate to say a few words about DF with a complete vector sensor since some of the results are applicable to the tripole. Nehorai and Paldi, when studying vector sensors, developed a direction finding measure of performance called the mean square angular error (MSAE) and showed that it reduces to a simple closed-form expression for the case when only the electric field is measured [17]. They also derived an expression for the Cramer-Rao lower bound on “the minimum attainable variance of unbiased DOA estimators for a general vector-sensor array model and multi-electromagnetic sources that are assumed to be stochastic and stationary.” Both measures are applied to study direction finding with a single, full vector sensor. They show that estimating the DOA of two uncorrelated co-channel sources with a single vector sensor is possible, even if the two sources are located at the same angle, as long as the polarizations are different (rotation sense or axial ratio). An important consequence of their analysis is that when the polarization of the incident

signal approaches a linear polarization, estimating the DOA becomes difficult with a single sensor that measures only the electric field (i.e., the tripole) since the direction of propagation can lie anywhere in the plane perpendicular to the locus of the measured E-field vector.

Others, such as [3], [20], and [21] have built on the work of [17] by proposing methods to use a single full-vector sensor (not a tripole) for direction finding. In [3], the authors used a modified ESPRIT algorithm and a single vector sensor to locate multiple monochromatic, incoherent sources by exploiting the polarization and spatial diversity in each signal. In [20], the authors studied the Cramer-Rao lower bound for source localization variance to discover a minimum vector sensor configuration which requires only two electric and two magnetic sensors. The authors of [21] applied a MUSIC algorithm to study the resolvability of a single vector sensor. They concluded, in agreement with the results in [17], that the maximum number of resolvable, uncorrelated, co-channel signals is two. The methods and conclusions offered by these authors can aid in our understanding of the tripole configuration which we now begin to investigate.

The oldest paper discovered during this literature review was the 1951 article by Morgan and Evans [22]. Using purely geometric arguments, they demonstrate that if we know the sinusoidal, time-varying, three-dimensional vector components of the electric field (E_x , E_y , and E_z) of a single incident plane wave at any point in free space, we can determine its direction of propagation and polarization parameters (axial ratio, magnitude of major axis, tilt, and sense of rotation CW or CCW). They also show how to go in reverse. That is to say, given the polarization parameters and the direction of propagation, they show how one can obtain the x, y, and z-components of the E-field.

Morgan and Evans begin their derivation using the parametric description of an ellipse in a two-dimensional plane. Although they mention the limiting case of a linearly polarized wave, all of their analysis assumes an elliptic polarization. As was typical practice in their time, they used their derived equations to develop a nomogram tool (graphical chart) showing the relationship between the amplitude and phase of two E-field components for various combinations of axial ratio and tilt angle of the ellipse. They then expand their model to three-dimensions and explain, in great detail, how to use their nomogram to determine the direction of propagation and the polarization of any plane wave in three-dimensional space. In the present time, a nomogram would not typically be used, but the conclusion of their work is the same: As long as we can isolate the electric field components of a single elliptically polarized plane wave, we can determine its three-dimensional direction of propagation and the polarization parameters.

Morgan and Evans never specifically proposed a method to extract the E-field vector components from the incident wave. In 1999, the authors of [23] suggested using three mutually orthogonal dipole antennas (i.e., the tripole) to isolate the three vector components of a single incident plane wave. They applied their dipole antenna arrangement and the equations derived by Morgan and Evans to measure the polarization parameters and angle-of-arrival of high frequency (HF) monochromatic electromagnetic waves reflected off the ionosphere. The results of an experimental verification of their method are provided in [24] and [25] where they showed that measurements differed by 2° - 6° when compared to calculated values for both azimuth and elevation angles. They did not, however, consider multipath or multiple co-channel emitters.

Another paper describing DOA estimation using a tripole is presented in [14] where the authors sought to locate the incident direction of astronomical radiation phenomenon. The orthogonal dipoles are used, again, to isolate the x, y, and z-components of the incident waves. Their method begins by using the Unitary Matrix Pencil method (an alternative to Fourier transforms, see [26]) to estimate the frequencies of the incident waves. A least squares solver is then applied to estimate the amplitude and phases of the incident waves in each dimension (x, y, and z). From the amplitude and phase measurements, the DOA is estimated using the generalized Stokes parameters. A simulation of the method shows an average accuracy within 1° for three circularly polarized waves when the signal-to-noise ratio is above 30dB.

The authors of [27] used a set of three mutually orthogonal dipoles in their DF application for wide-banded spread spectrum signals in code-division multiple access (CDMA) cellular telephone systems. Their analysis begins by first formulating the signal and channel models based on the IS-95 communication standard. Since each cell phone user will have a different channel response due to their location relative to the receive antenna, the channel response of each user must be estimated separately. To achieve this, the authors use the reference timing contained in the individual users' PN code along with a maximum likelihood algorithm. Using a linear time-invariant approximation, the received signal on each antenna will be a sum of the n incident signals (corresponding to the n cell phone users), summed over all multipaths for each user, and convolved with the x, y, and z-components of each user's channel impulse response. By comparing the amplitude weights and the multipath propagation delays of each user's signal on each of the three antennas of the tripole, the directions-of-arrival can be estimated. They present

simulation results showing accuracies within 1° for two users, each with five randomly generated multipath reflections.

Although their results are quite accurate, there are several drawbacks to using the approach laid out in [27]. The most significant drawback is that they have assumed some knowledge of the transmitting source. This *a priori* knowledge is critical to estimating the channel response for each individual transmitter. Another drawback is that their algorithm gives multiple directions-of-arrival corresponding to all multipath reflections that have a signal strength above a certain threshold. They give no indication as to which angle-of-arrival is the true line-of-sight bearing of the emitter.

The authors of [15] studied the performance of the tripole at receiving a single desired incident plane wave in the presence of an unwanted interferer, each incident from arbitrary directions. Although they didn't perform DF, their paper is worth mentioning because of the conclusions they draw from their simulations. They show that the mutually orthogonal antenna arrangement is exceptionally well suited to reject an interfering signal if the wanted signal and the interferer are elliptically or circularly polarized. In the special case where the wanted signal and the interferer are both linearly polarized, the wanted signal is very susceptible to interference from a wide range of incident angles.

Kwok-Chiang Ho, et al., studied the linear dependence of steering vectors associated with the tripole [28] and incorporated many ideas from [15]. They prove an important theorem regarding the ability of the tripole to determine the DOA of a signal. It states, in rough terms, that if two signals are impinging on a single tripole, each with its own set of arrival angles and polarization parameters, then the two signals will be linearly

dependent if and only if “the two signals are of opposite DOA’s with conjugate polarizations” OR “the two signals are linearly polarized with parallel electric field.” Their conclusions suggest that judicious placement of a tripole is necessary for accurate DOA estimates. Placing the tripole close to an infinite ground, for example, effectively limits the arrival angles to one hemisphere thereby negating the first condition in the theorem. The second condition of the theorem suggests, in concurrence with [15] and [17], that estimating the DOA of linearly polarized signals would not be effective with a single tripole. This helps explain the accurate results obtained in [14] and [23] which, if you recall, measured the DOA of randomly polarized skywaves (astronomical radiation and reflections of HF radiation off the ionosphere, respectively) using a single tripole placed near earth ground.

Lastly, DF results using a trimmed-down, electrically small vector sensor placed on a small UAV were published in [29]. Although they didn’t use a tripole, the article is worth mentioning since their DF method is very similar to the method employed by the aeronautical systems development company described in Chapter 1. Beginning with an explanation of the mutual coupling problem between the vector sensor antennas and the conducting metal airframe, they suggest reducing the vector sensor elements to only one dipole for elevation measurements and two loop antennas for azimuth measurements. With their UAV mounted on a rotating pedestal inside an anechoic chamber, they measured the magnitude and phase on each antenna while rotating the pedestal in 2° azimuth increments. The measured values for various frequencies are stored in a table. The DOA of a measured signal is then compared to the data in the table using a maximum-likelihood approach to compensate for the difference between the ideal

response and the measured response. The system could detect a single, monochromatic incident signal to within 10° in the worst case and 1.3° in the best case.

2.6 CONCLUSION

This chapter has reviewed some common direction finding (DF) methods and offered a literature review on DF with mutually orthogonal antennas. Since a basic understanding of the DF problem was necessary, we started with a review of the narrowband signal model followed by an overview of the common, array based, DF methods known as the classic beamforming method, the monopulse method, and the phase matching method. Three popular “super-resolution” techniques (maximum likelihood, MUSIC, and ESPRIT) were also introduced. A literature review was then presented which focused on explaining the works of several authors who have used a mutually orthogonal arrangement of antennas to perform direction finding. Since the so-called tripole (three mutually orthogonal dipoles) was the most prevalently used antenna, the literature review emphasized the work of at least seven sets of authors who have worked with this antenna configuration.

The tripole, having linearly polarized small dipole elements with simple radiation pattern and very small cross-polarization (assumed zero), is well suited to extract independent measurements of the electric field components at a single point in space; namely, at the origin of the coordinate system that defines the antenna arrangement (a verification of this fact will be given in Chapter 3). Several authors have shown that simultaneously estimating the DOA of two co-channel sources is possible with a single tripole if the incident waves have different, non-linear, polarizations. However, when the

polarization of the incident waves is linear, the tripole is a poor choice for estimating the directions-of-arrival.

In the following chapters, we continue to investigate the tripole but we also seek to accomplish DF with a mutually orthogonal set of wideband antennas. Ideally, we'd like to use the wideband antennas mentioned in Chapter 1 (also see Appendix A). However, to reduce computation time and to study the mutual coupling problem, we will examine planar bowtie antennas and biconical antennas. Our first task will be to transition from a signal model $s(t)$ to a plane wave model $\tilde{E}(x, y, z; t)$ that allows us to easily work with the polarization properties of the incident electric field. The effective height concept will be employed for this purpose and will be used to formulate and study three DF algorithms.

CHAPTER 3

Approach & Methodology

3.1 INTRODUCTION

This chapter explains the methods used to study direction finding (DF) with an arrangement of mutually orthogonal antennas. As a starting point, the basic uniform plane wave model is introduced and related to the signal model from the previous chapter. Then, the vector effective height of any antenna is defined and used to study the tripole configuration. A simple algorithm is offered to locate the direction-of-arrival of uniform plane waves using the tripole. The effective height is then incorporated into a maximum likelihood-based and a MUSIC-based algorithm that can be used with a set of three non-dipole antennas. To study the maximum likelihood-based and the MUSIC-based algorithms, three bicone antennas as well as three bowtie antennas were placed in the orthogonal arrangement. In all three arrangements (tripole, bicone antennas, and bowtie antennas), testing of the algorithms was accomplished by first irradiating the antennas with numerous plane waves in CST Microwave Studio software and then exporting the received voltage signals to Matlab for processing by the algorithms. Later, in Chapter 4, the results of these simulations will be presented and compared. To begin, let's look at the uniform plane wave model of an electric field.

3.2 UNIFORM PLANE WAVE MODEL

The electric field of a transverse electromagnetic (TEM) uniform plane wave (UPW) traveling in an unbounded lossless media can be written as [30]

$$\vec{E}(x, y, z) = (E_x \hat{x} + E_y \hat{y} + E_z \hat{z}) e^{-j\vec{k} \cdot \vec{r}} \quad (\text{Volts/meter}) \quad (3-1)$$

where $\vec{k} = k_x \hat{x} + k_y \hat{y} + k_z \hat{z}$ is the free space propagation vector that points in the direction of wave travel and contains purely real components k_x, k_y, k_z that represent the phase constants in the x, y, and z directions, respectively. The vector \vec{k} has magnitude given by

$$|\vec{k}| = k = \sqrt{k_x^2 + k_y^2 + k_z^2} = \frac{2\pi}{\lambda} = \sqrt{\epsilon_o \mu_o} \quad (3-2)$$

where λ is the wavelength, $\omega = 2\pi f$ is the angular frequency (f is frequency in Hz), ϵ_o is the free space permittivity, and μ_o is the free space permeability. The vector $\vec{r} = x\hat{x} + y\hat{y} + z\hat{z}$ is a position vector in rectangular coordinates that points to the location in space where we are observing the electric field vector. The rectangular vector components E_x, E_y, E_z are complex quantities in general and can be written with a magnitude and phase as [31: 57]

$$E_x = |E_x| e^{j\phi_x} \quad E_y = |E_y| e^{j\phi_y} \quad E_z = |E_z| e^{j\phi_z} \quad (3-3)$$

Unless otherwise stated, all vector components of field vectors are assumed complex and will be written in this way.

At any point in space defined by \vec{r} , the exact same electric field vector resulting from (3-1) can also be expressed with spherical vector components at that point as

$$\vec{E}(x, y, z) = (E_r \hat{r} + E_\theta \hat{\theta} + E_\phi \hat{\phi}) e^{-j\vec{k} \cdot \vec{r}} \quad (3-4)$$

where the unit vectors \hat{r} , $\hat{\theta}$, and $\hat{\phi}$ depend on \vec{r} . Figure 3 - 1 shows the relationship between the two coordinate systems for an arbitrarily chosen \vec{r} . It should be noted that (3-4) is not a general expression for the plane wave since it contains spherical field components and rectangular vectors \vec{k} and \vec{r} in the exponential.

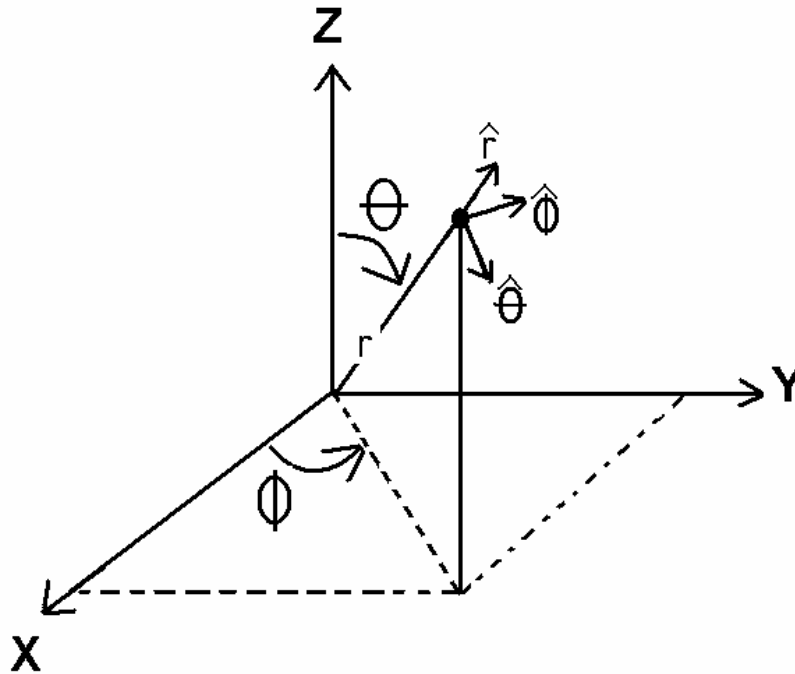


Figure 3 - 1: Coordinate systems

The rectangular vector components in (3-1) are related to the spherical vector components in (3-4) by the 3x3 spherical-to-rectangular matrix transformation given by [6: 1083]

$$\begin{bmatrix} E_x \\ E_y \\ E_z \end{bmatrix} = \begin{bmatrix} \sin(\theta) \cos(\phi) & \cos(\theta) \cos(\phi) & -\sin(\phi) \\ \sin(\theta) \sin(\phi) & \cos(\theta) \sin(\phi) & \cos(\phi) \\ \cos(\theta) & -\sin(\theta) & 0 \end{bmatrix} \begin{bmatrix} E_r \\ E_\theta \\ E_\phi \end{bmatrix} \quad (3-5)$$

Both (3-1) and (3-4) are assumed to be time-harmonic fields (i.e., with time variation of the form $e^{j\omega t}$) that have been written in their complex, time-invariant, spatial form. Their instantaneous forms, denoted with a tilde, are recovered by taking

$$\tilde{E}(x, y, z; t) = \text{Re}\{\tilde{E}(x, y, z)e^{j\omega_c t}\} \quad (3-6)$$

where the $\text{Re}\{\bullet\}$ operator has extracted the real part. Equation (3-6) has been written with the term $e^{j\omega_c t}$ to indicate that the instantaneous form is recovered by using the angular frequency of the carrier. (Recall from the previous chapter, section 2.2, that the signal from the transmitting source was represented as $s(t)e^{j\omega_c t}$ where $s(t)$ was the baseband signal and $\omega_c = 2\pi f_c$ was the angular frequency of the carrier. We also assume that the narrowband signal model described in section 2.2 still applies.)

As this UPW propagates through space, the instantaneous electric field of (3-6) traces out a curve that defines the polarization of the wave. In general, the curve is elliptical with circular and linear polarizations being limiting cases. Also, at any constant point in space, the tip of the electric field will trace out an ellipse as time progresses. This elliptical locus of the electric field vector will reside in a plane that is perpendicular to the direction of wave propagation \hat{k} . The magnitude and phase relationship between the wave's vector components determines the exact nature of the wave's polarization. The reader is assumed to have a basic familiarity with these polarization concepts (see [30: 154-173] for a complete explanation). One polarization parameter of particular importance for later work is the axial ratio defined as the ratio of the major axis to the minor axis of the instantaneous electric field ellipse by

$$AR = \frac{\tilde{E}_{\max}}{\tilde{E}_{\min}} \text{ where } 1 \leq AR < \infty \quad (3-7)$$

For later reference, Figure 3 - 2 shows the relationship between axial ratios of 1, 2, 5, 10, 20, and 80. Although not drawn, an $AR=\infty$ would be a vertical line in the figure. In the next chapter, we will examine the effect of the axial ratio on the performance of our algorithms.

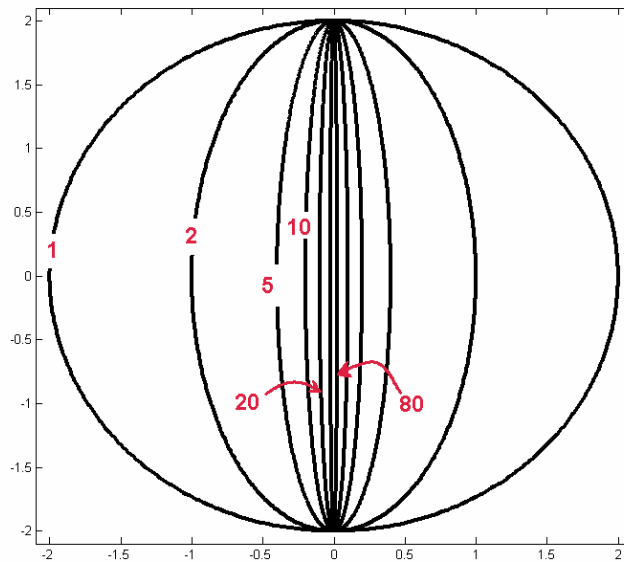


Figure 3 - 2: Axial ratios of an ellipse

In the work that follows, electric fields are assumed to have been radiated from sources that are very far away from the origin of our coordinate system such that we may treat the arriving fields as uniform plane waves. Since these uniform plane waves have an electric field locus that resides in a plane for any constant point in space, it will be convenient to describe the electric field vector using only two vector components instead of three. This will be possible with the proper choice of coordinate system if one axis

points in the direction of wave travel. The natural choice is to use spherical vector components but there must be a restriction on the position vector \vec{r} .

Figure 3 - 3 shows several phase fronts of a uniform plane wave that are incident on the coordinate origin. Two position vectors, \vec{r}_1 and \vec{r}_2 , have been drawn to the points P_1 and P_2 , respectively, that are located on one of the phase fronts. The wave is traveling

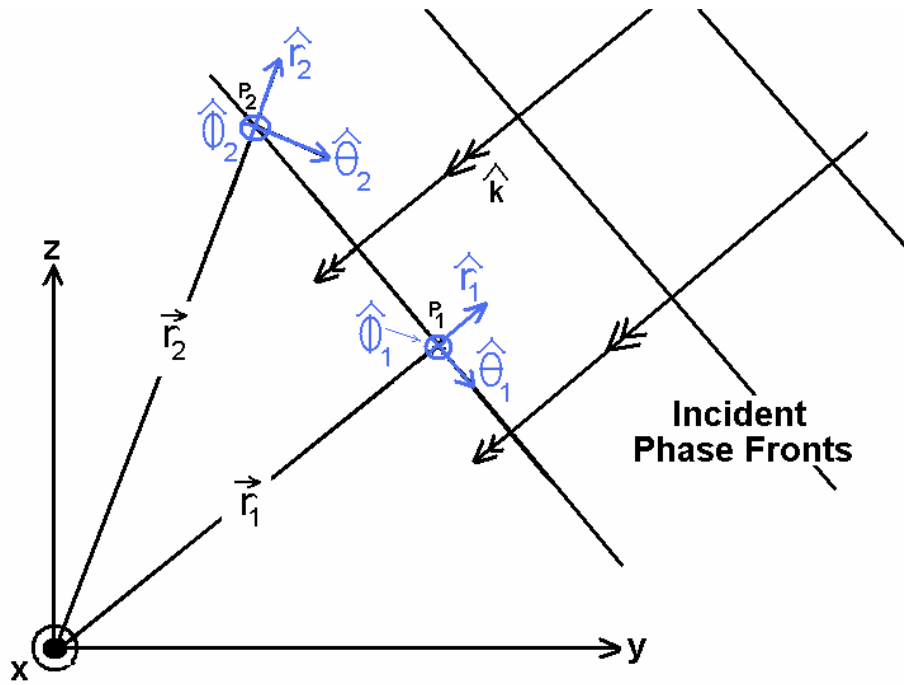


Figure 3 - 3: Phase fronts of a TEM UPW traveling toward the origin

toward the coordinate origin along a radial line such that $\hat{k} = -\hat{r}_1$. At any snapshot in time, the electric field will be physically the same at both P_1 and P_2 because the wave is a UPW which by definition has equal amplitude and equal phase everywhere in the plane. However, the mathematical representation of the electric field's vector components at the

two points will differ when using the spherical representation of (3-4) since the unit vectors \hat{r} , $\hat{\theta}$, and $\hat{\phi}$ are functions of position.

At point P_1 , the radial component E_{r_1} is equal to zero in the spherical representation of (3-4) and the locus of the electric field vector can be completely described using only two components E_{θ_1} and E_{ϕ_1} as desired. At P_2 , we need all three vector components E_{r_2} , E_{θ_2} , and E_{ϕ_2} to describe the electric field vector since the unit vector \hat{r}_2 is not along the same line as \hat{k} . Clearly, we want to restrict our position vector to that of \vec{r}_1 .

At first glance, insisting $\hat{r} = -\hat{k}$ may appear to be an overly restrictive condition since it forces the position vector to reside along a single line extending radially outward from the coordinate origin. However, the next section describes a tool, known as the vector effective height of an antenna, which makes this choice for \hat{r} perfectly natural and very convenient for our work.

3.3 VECTOR EFFECTIVE HEIGHT OF ANY ANTENNA

The vector effective height of any antenna, denoted $\vec{h}(\theta, \phi)$ (meters), is a vector quantity related to the radiated far-zone electric fields $\vec{E}^a = E_{\theta}^a \hat{\theta} + E_{\phi}^a \hat{\phi}$ (Volts/meter) of the antenna by [6: 88]

$$\begin{aligned}\vec{h}(\hat{r}, \theta) &= -\frac{E^a}{j \frac{kI_{in}}{4r} e^{-jkr}} \hat{e}_\theta - \frac{E^a}{j \frac{kI_{in}}{4r} e^{-jkr}} \hat{e}_\phi \\ &= h_\theta \hat{e}_\theta + h_\phi \hat{e}_\phi\end{aligned}\quad (3-8)$$

where I_{in} is the current in the terminals of the antenna, η is the intrinsic impedance of free space, $k = |\vec{k}|$ is the free space propagation constant, and $r = |\vec{r}|$ is the magnitude of the position vector. The components h_θ and h_ϕ are complex quantities in general and can be written in a similar manner to the field vector components in (3-3).

If we dot multiply the effective height with the vector components of an incident electric field $\vec{E}^i(\hat{r}, \theta) = E^i_\theta \hat{e}_\theta + E^i_\phi \hat{e}_\phi$ that has been defined in the same coordinate system as $\vec{h}(\hat{r}, \theta)$ and has a direction of propagation along a radial line toward the origin such that $\hat{r} = -\hat{k}$, then the resulting product is the open-circuited voltage V across the terminals of the antenna

$$V = \vec{h}(\hat{r}, \theta) \cdot \vec{E}^i(\hat{r}, \theta) \quad (\text{Volts}) \quad (3-9)$$

In matrix notation, where \vec{h} and \vec{E}^i are both column vectors, the open-circuited voltage can be written as

$$V = \vec{h}^T \vec{E}^i = h_\theta E^i_\theta + h_\phi E^i_\phi \quad (3-10)$$

where the T superscript is the transpose. The effective height has been defined here with spherical vector components but $V = \vec{h}^T \vec{E}^i$ applies equally well if \vec{h} and \vec{E}^i are both defined with rectangular components. In fact, any right-handed coordinate system can be used but only if the two vectors \vec{h} and \vec{E}^i are both defined in the same coordinate system [31].

Since the vector components of $\vec{h}(\ , \)$ and $\vec{E}^i(\ , \)$ are complex in general, we might be tempted to use the complex conjugate transpose (i.e., Hermitian transpose) in (3-10) by taking $V = \vec{h}^H \vec{E}^i$ instead. This is not correct. According to IEEE STD 145-1983 [32], the effective height is defined in the antenna's transmit mode so that its sense of rotation (right-hand or left-hand polarized) is polarization aligned to an incident wave with the same sense of rotation. The Hermitian transpose reverses the polarization sense of $\vec{h}(\ , \)$. Don't use it when computing the open-circuited voltage V .

The benefit of working with the effective height is that it accounts for the polarization mismatch between the antenna and the incident plane wave. The complete derivation of (3-8) through (3-10) is based on the Lorentz reciprocity theorem and can be found in [33: 294-303]. In the next section, we utilize the effective height to show how the tripole extracts the x, y, and z components of the electric field.

3.4 USING THE TRIPOLE AS A FIELD PROBE

This section shows how the tripole can be used as a far-field probe to extract the x, y, and z-components of an incident plane wave. The literature review in Chapter 2 mentioned several authors who used this fact as a starting point in their work, but none of them offered any proof or confirmation that it is true. The following derivation is based on the effective height described in the previous section. Later, in section 3.6, the effective height is used to analyze a more general set of mutually orthogonal antennas.

Using (3-5) with $E_r^i = 0$ (a valid assumption since $\hat{r} = -\hat{k}$ as discussed in section 3.2 and 3.3), we see that the rectangular components of an incident wave can be written in terms of its spherical components as

$$E_x^i = E^i \cos(\theta) \cos(\phi) - E^\theta \sin(\theta) \quad (3-11)$$

$$E_y^i = E^i \cos(\theta) \sin(\phi) + E^\theta \cos(\theta) \quad (3-12)$$

$$E_z^i = -E^\theta \sin(\theta) \quad (3-13)$$

When this plane wave strikes an antenna, the induced open-circuited voltage at the antenna terminals is given by (3-10). But to use (3-10), we need the effective heights of the short dipole antennas that form the tripole. In the absence of mutual coupling, it's a straight forward application of antenna theory and (3-8) to show that the effective heights of the three short dipoles (i.e., Hertzian dipoles) can be written with spherical vector components as

$$\text{Short dipole along X-axis: } \vec{h}_x = \Delta l \left(\hat{e}_\theta \cos(\theta) \cos(\phi) - \hat{e}_\phi \sin(\theta) \right) \quad (3-14)$$

$$\text{Short dipole along Y-axis: } \vec{h}_y = \Delta l \left(\hat{e}_\theta \cos(\theta) \sin(\phi) + \hat{e}_\phi \cos(\theta) \right) \quad (3-15)$$

$$\text{Short dipole along Z-axis: } \vec{h}_z = \Delta l \left(-\hat{e}_\theta \sin(\theta) \right) \quad (3-16)$$

where Δl is the infinitesimal length of each dipole. (Note: The notation introduced here could cause some confusion between variables such as \vec{h}_x , h_x , and h_x . The quantity \vec{h}_x is a vector representing the effective height of the X-directed antenna. The quantity h_x is the x-component of the effective height of an antenna that has not been specified. The quantity h_x is the x-component of the effective height of the X-directed antenna.)

Now, applying (3-10) to the antenna along the X-axis, we obtain the complex open-circuited voltage V_x as follows

$$\begin{aligned} V_x &= \vec{h}_x^T \vec{E}^i = \Delta l [\cos(\theta) \cos(\phi) \quad -\sin(\phi)] \begin{bmatrix} E^i \\ E^i \end{bmatrix} \\ &= \Delta l (E^i \cos(\theta) \cos(\phi) - E^i \sin(\phi)) \\ &= \Delta l E_x^i \quad (\text{Volts}) \end{aligned} \quad (3-17)$$

where the last step used a direct comparison to equation (3-11). Similarly, the complex open-circuited voltage for the antenna along the Y-axis, denoted V_y , can be found from

$$\begin{aligned} V_y &= \vec{h}_y^T \vec{E}^i = \Delta l [\cos(\theta) \sin(\phi) \quad \cos(\phi)] \begin{bmatrix} E^i \\ E^i \end{bmatrix} \\ &= \Delta l (E^i \cos(\theta) \sin(\phi) + E^i \cos(\phi)) \\ &= \Delta l E_y^i \quad (\text{Volts}) \end{aligned} \quad (3-18)$$

where, again, the last step used a direct comparison to equation (3-12). After applying the same steps as shown above, the complex open-circuited voltage for the antenna along the Z-axis is

$$V_z = \vec{h}_z^T \vec{E}^i = \Delta l E_z^i \quad (\text{Volts}). \quad (3-19)$$

Equations (3-17) through (3-19) demonstrate that the short dipoles essentially *select off* only their respective component of the incident electric field and then scale it by the real constant Δl .

The analysis presented above has neglected the effects of mutual coupling between the dipole elements. However, based on the works of [15], [28], and [34] the

impact of mutual coupling is almost negligible when the short dipoles are arranged in the tripole configuration.

The next section describes a simple algorithm that can be used to compute the direction-of-arrival of multiple plane waves that are incident on the tripole at the same time.

3.5 SIMPLE DF ALGORITHM USING THE TRIPOLE

At any constant point in space, the tip of the electric field modeled by (3-1) will trace out an ellipse as time progresses (circular and linear traces are special cases). This elliptical locus of the electric field vector will reside in a plane that is perpendicular to the direction of wave propagation \hat{k} as mentioned in section 3.2. Therefore, the direction-of-arrival of an incident plane wave can be estimated by finding any vector that is perpendicular to the plane containing the electric field locus. For our case, the point in space we are interested in is the origin of the coordinate system which is the phase center for all three antennas in the tripole. The position vector at this point has magnitude $r = x = y = z = 0$ forcing $e^{j\vec{k}\cdot\vec{r}} = 1$ in (3-1).

To find the direction-of-arrival vector that is perpendicular to the plane containing the electric field locus, we only need to compute the vector cross-product of any two independent vectors that lie in the plane. The vectors that lie in the plane can be obtained by observing the electric field components in time. Using (3-6) and (3-17) through (3-19), we can write the instantaneous electric field of a single incident wave as

$$\begin{aligned}
\tilde{E}^i &= \text{Re}\left\{\left(E_x^i \hat{x} + E_y^i \hat{y} + E_z^i \hat{z}\right)e^{j\omega t}\right\} \\
&= \text{Re}\left\{\left(\frac{V_x}{\Delta l} \hat{x} + \frac{V_y}{\Delta l} \hat{y} + \frac{V_z}{\Delta l} \hat{z}\right)e^{j\omega t}\right\}
\end{aligned} \tag{3-20}$$

which becomes

$$\tilde{E}^i = \hat{x} \frac{|V_x|}{\Delta l} \cos(\omega t + \phi_x) + \hat{y} \frac{|V_y|}{\Delta l} \cos(\omega t + \phi_y) + \hat{z} \frac{|V_z|}{\Delta l} \cos(\omega t + \phi_z) \tag{3-21}$$

where ϕ_x , ϕ_y , and ϕ_z are the phase angles of the complex open-circuited voltages (and also of the electric field components since the angles were not altered when scaled by the real quantity Δl).

Computing (3-21) at any two points in time (eg: $\omega t = 0$ and $\omega t = \pi/2$) will yield two vectors, \tilde{a}_1 and \tilde{a}_2 , existing in the plane containing the electric field locus.

Therefore, we have

$$\tilde{a}_1 = \hat{x} \frac{|V_x|}{\Delta l} \cos(\phi_x) + \hat{y} \frac{|V_y|}{\Delta l} \cos(\phi_y) + \hat{z} \frac{|V_z|}{\Delta l} \cos(\phi_z) \tag{3-22}$$

and

$$\tilde{a}_2 = \hat{x} \frac{|V_x|}{\Delta l} \cos\left(\frac{\pi}{2} + \phi_x\right) + \hat{y} \frac{|V_y|}{\Delta l} \cos\left(\frac{\pi}{2} + \phi_y\right) + \hat{z} \frac{|V_z|}{\Delta l} \cos\left(\frac{\pi}{2} + \phi_z\right) \tag{3-23}$$

The vector that points toward the direction-of-arrival of the incident wave, \tilde{a}_{DOA} , is therefore given by

$$\tilde{a}_{DOA} = \tilde{a}_1 \times \tilde{a}_2 \tag{3-24}$$

The simple approach presented here only works when certain assumptions are satisfied. The first assumption is that the incident plane wave arrives from a predetermined hemisphere of the coordinate system containing the tripole. This

assumption is necessary since there will be a 180° ambiguity in the computed direction-of-arrival from the cross-product in (3-24). The ambiguity is avoided by selecting the solution that exists in the chosen hemisphere. This assumption seems reasonable if the tripole is, for example, placed near earth ground and directed to look for incident skywaves. Another example is if the tripole is placed on an aircraft and directed to look for signals coming from the ground. In this thesis work, the upper hemisphere of the coordinate system was chosen ($0^\circ \leq \theta \leq 90^\circ$, $0^\circ \leq \phi < 360^\circ$).

The second necessary assumption is that the incident plane wave must have some ellipticity in its polarization (it cannot be linearly polarized). If the incident wave is purely linearly polarized, the vectors \tilde{a}_1 and \tilde{a}_2 will be scalar multiples of each other and the \tilde{a}_{DOA} will be zero (assuming no noise). Another way to think about it is that, for a linearly polarized wave, the vectors \tilde{a}_1 and \tilde{a}_2 won't span the plane containing the electric field locus. This appears to be a somewhat restrictive assumption since many signals are transmitted with linearly polarized electric fields. In the next chapter, simulation results are presented which show how close the incident wave can come to being linearly polarized before this algorithm fails.

When the above assumptions are satisfied, this approach can also be used when multiple waves are incident on the tripole, but only if the incident waves can be separated in the frequency domain. If they can, then the magnitude and phase of each component of each incident wave can be obtained by computing the fast Fourier transform on each element of the tripole. The direction-of-arrival of each wave can then be processed using the algorithm described above.

Testing of this algorithm was accomplished by irradiating the tripole with various plane waves in CST Microwave Studio and then processing the received voltage signals in Matlab. CST Microwave Studio was used since it includes all mutual coupling effects. However, since CST Microwave Studio doesn't currently offer the ability to simulate multiple plane waves simultaneously, plane waves were simulated one-at-a-time and the response from each plane wave was summed in Matlab. The fast Fourier transform was used to extract the frequencies of the incident waves as well as the magnitude and phase terms for each electric field component. Although the development above did not include the effects of random noise, the simulation results in Chapter 4 will be given for various signal-to-noise ratios (SNRs) (defined by (3-32) in section 3.7).

To summarize this section and the previous, we restate the main points. The tripole configuration of short dipole antennas can extract the x, y, and z components of the instantaneous electric field vector of an incident plane wave. Since we are measuring this field at a single point in space, the electric field's tip will trace an elliptical shape that resides in a plane that is perpendicular to the direction of wave travel. The algorithm for estimating the direction-of-arrival of a single incident plane wave using the tripole is as follows:

- 1) Measure the open-circuited voltages on the tripole.
- 2) Use (3-22) and (3-23) to find two vectors in the plane of the electric field locus.
- 3) Compute \tilde{a}_{DOA} using (3-24).
- 4) Select the solution to \tilde{a}_{DOA} that exists in the predetermined hemisphere.

This approach works because the dipoles maintain the same radiation pattern for all frequencies of interest (assuming they stay Hertzian). However, when the antenna elements are not short dipoles, the effective heights of each antenna will vary with

frequency and the open-circuited voltages will not be proportional only to a single field component. Therefore, we cannot use the simple algorithm presented here. Since one of the goals of this thesis was to determine if the wideband blade antennas mentioned in Chapter 1 could be used in the orthogonal arrangement, the following section develops two algorithms that can be used (in theory) with an arbitrary set of three mutually orthogonal antennas.

3.6 DF WITH THREE NON-DIPOLE ANTENNAS

One aim of this thesis was to consider other antennas, besides the tripole, that could be used in the orthogonal arrangement with the eventual goal of attempting this arrangement on the wideband antennas described in Chapter 1 (also see Appendix A). Toward this end, we now describe two algorithms that were developed for use with an arbitrary set of three mutually orthogonal antennas that are assumed to have the same phase center. The algorithms are based on the maximum likelihood technique and the MUSIC technique described in section 2.4. The algorithms were tested on the antenna configurations shown in Figure 3 - 4(a) and (b). Figure 3 - 4(a) shows three biconical antennas (with hemispherical end caps) that have been placed in the proposed arrangement. A biconical antenna is similar to a dipole but has a broadband characteristic determined by the cone angle α shown in Figure 3 - 5 (see section 3.7). Figure 3 - 4(b) shows three bowtie antennas in the orthogonal arrangement. The bowtie antennas were studied because they closely resemble the wideband antennas suggested by the sponsor of this thesis. They can also be simulated quickly in CST Microwave Studio (much faster than the actual wideband antenna model described in Appendix A).

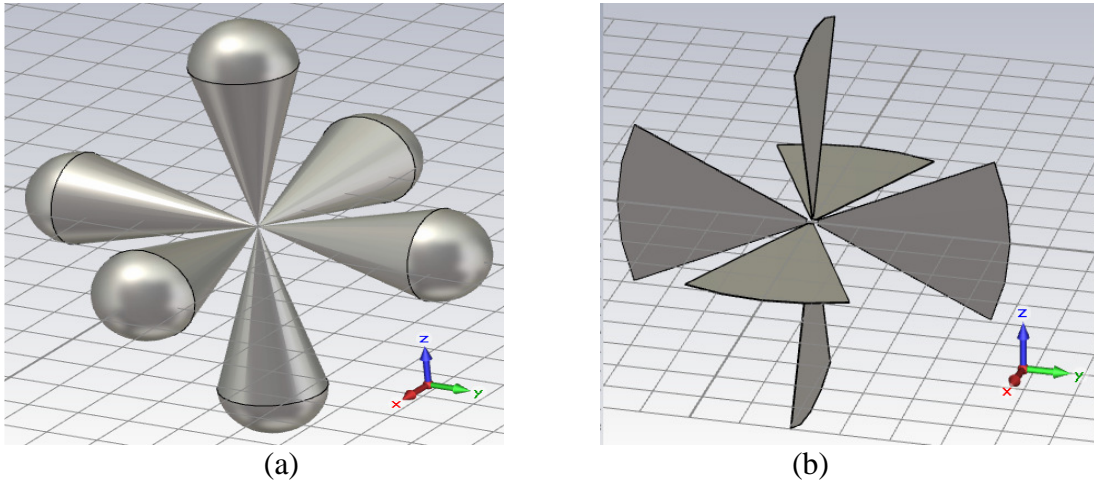


Figure 3 - 4: Orthogonal antennas
(a) Biconical antennas
(b) Bowtie antennas

When the antenna elements are not short dipoles, we can apply (3-10) to each antenna and form the following matrix equation for a single incident wave

$$\begin{bmatrix} V_x \\ V_y \\ V_z \end{bmatrix} = \begin{bmatrix} h_x & h_x \\ h_y & h_y \\ h_z & h_z \end{bmatrix} \begin{bmatrix} E^i \\ E^i \end{bmatrix} + \begin{bmatrix} v_x \\ v_y \\ v_z \end{bmatrix} \quad (3-25)$$

or, in short hand, we can write $\vec{V} = \mathbf{H}\vec{E}^i + \vec{v}$ where the bold \mathbf{H} denotes the 3×2 matrix of effective heights that is a function of ω , θ , and ϕ of the incident wave and \vec{v} is a 3×1 complex Gaussian noise vector with uncorrelated elements having zero mean and variance of σ^2 . The frequency ω , we assume, can be found using a Fourier transform on the measured voltage, but (3-25) still has four unknowns (θ , ϕ , E^i , and E^i) and only

three equations. In both the maximum likelihood algorithm and the MUSIC algorithm outlined below, we reduce the number of unknowns in (3-25) to only two by searching through a tabled grid of θ and ϕ values where we know the value of \mathbf{H} .

We first describe the maximum likelihood algorithm. Following the procedure outlined in section 2.4 for the noise-free case, we can attempt to minimize the difference equation g (arbitrarily named) given by

$$g = \|\vec{V} - \mathbf{H}\vec{E}^i\|^2 \quad (3-26)$$

For each combination of (θ, ϕ) , we apply least squares to (3-25) (without the noise) and write the electric field as

$$\vec{E}^i = (\mathbf{H}^H \mathbf{H})^{-1} \mathbf{H}^H \vec{V} \quad (3-27)$$

where the superscript $(\bullet)^H$ denotes the Hermitian transpose. Substituting (3-27) into (3-26) and performing some linear algebra, we have

$$\begin{aligned} g &= \left\| \vec{V} - \mathbf{H}(\mathbf{H}^H \mathbf{H})^{-1} \mathbf{H}^H \vec{V} \right\|^2 \\ &= \left\| \left(\mathbf{I} - \mathbf{H}(\mathbf{H}^H \mathbf{H})^{-1} \mathbf{H}^H \right) \vec{V} \right\|^2 \\ &= \left\| (\mathbf{P}^\perp) \vec{V} \right\|^2 \\ &= (\mathbf{P}^\perp \vec{V})^H (\mathbf{P}^\perp) \vec{V} \\ &= \vec{V}^H \mathbf{P}^\perp \vec{V} \end{aligned} \quad (3-28)$$

where $\mathbf{P}^\perp = \mathbf{I} - \mathbf{H}(\mathbf{H}^H \mathbf{H})^{-1} \mathbf{H}^H$ is the orthogonal projection and \mathbf{I} is the 3×3 identity matrix. Applying a brute force 2-D search will produce a g -value for all selected

combinations of (θ, ϕ) . The (θ, ϕ) corresponding to the smallest g -value will, in theory, tell us the angles-of-arrival.

The steps involved in performing the maximum likelihood-based algorithm are as follows:

- 1) Determine the effective heights of each antenna for each combination of ω , θ , and ϕ anticipated.
- 2) Measure the open-circuited voltages on each antenna.
- 3) Find the carrier frequency of the wave using a Fourier transform (fft) on the measured voltages.
- 4) Compute the g -value in (3-28) for each combination of θ and ϕ .
- 5) Choose the smallest g -value which corresponds to the estimated angles-of-arrival θ and ϕ .

In this thesis, the effective heights were stored in a table for discrete combinations of ω , θ , and ϕ . Note that in practice, the minimum g -value is obtained using interpolation [4: 18, 47-48] on the computed g -values in the table. However, for this thesis, we omit this interpolation step by testing our algorithm using incident waves arriving with ω , θ , and ϕ values that we have stored in our table.

In addition to the maximum likelihood algorithm, we have also employed a MUSIC-based algorithm to study the orthogonal arrangement of antennas. Applying the MUSIC procedure outlined in section 2.4 for the K snapshots of our measured voltages, we estimate the covariance matrix of (3-25) as

$$\hat{\mathbf{R}}_v = \frac{1}{K} \sum_{k=1}^K \vec{V}(k) \vec{V}(k)^H = \frac{1}{K} \mathbf{V} \mathbf{V}^H \quad (3-29)$$

We then perform a singular value decomposition on the $\hat{\mathbf{R}}_v$ to get

$$\hat{\mathbf{R}}_v = \hat{\mathbf{U}} \hat{\mathbf{\Sigma}} \hat{\mathbf{U}}^H \quad (3-30)$$

from which we partition the matrix $\hat{\mathbf{U}} = [\hat{\mathbf{U}}_s, \hat{\mathbf{U}}_n]$ into the signal and noise subspaces.

Finally, for each combination of θ and ϕ in the applicable frequency table, we compute the MUSIC spectrum as

$$\hat{S}(\theta, \phi) = \frac{1}{|\mathbf{H}^H(\theta, \phi)\hat{\mathbf{U}}_n|^2} \quad (3-31)$$

which will have sharp peaks at the incident directions. Before we move to the next section which describes how these algorithms were tested, we summarize the steps in using the MUSIC-based algorithm:

- 1) Determine the effective heights of each antenna for each combination of ω , θ , and ϕ anticipated.
- 2) Measure the open-circuited voltages on each antenna.
- 3) Find the carrier frequency of the wave using a Fourier transform (fft) on the measured voltages.
- 4) Compute the covariance matrix $\hat{\mathbf{R}}_v$ using (3-29).
- 5) Perform singular value decomposition on $\hat{\mathbf{R}}_v = \hat{\mathbf{U}}\hat{\mathbf{\Sigma}}\hat{\mathbf{U}}^H$.
- 6) Partition $\hat{\mathbf{U}} = [\hat{\mathbf{U}}_s, \hat{\mathbf{U}}_n]$.
- 7) Compute the \hat{S} -value in (3-31) for each combination of θ and ϕ .
- 8) Choose the largest \hat{S} -value which corresponds to the estimated angles-of-arrival θ and ϕ .

3.7 TESTING THE ALGORITHMS

Testing of the DF algorithms was carried out in several steps. The first step was to model the antennas in CST Microwave Studio and to simulate their radiated far-zone electric field. The dimensions of each antenna are shown in Figure 3 - 5 (next page).

The dipole antennas were modeled with a length $L = 15\text{mm}$ and a width of $a = 0.1\text{mm}$. The bowtie antennas were modeled with a length of $L = 8.1\text{inches} = 205.7\text{mm}$. The angular spacing was set to $\alpha = 45^\circ$. These dimensions are similar to those of the

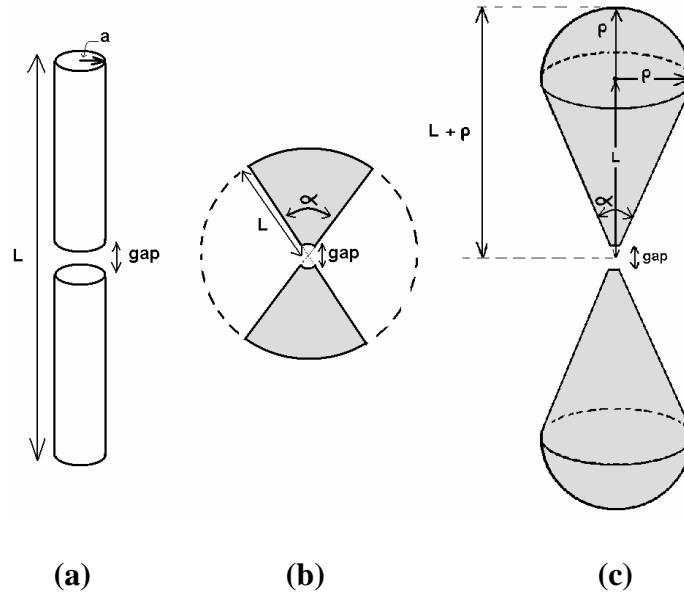


Figure 3 - 5: Antenna dimensions

(a) Dipole

(b) Bowtie

(c) Biconical with spherical end caps

wideband antennas suggested by the sponsor of this thesis (see Appendix A). The thickness of the bowties was set to 0.1mm. For the biconical antennas, the length was set to $2(L + \rho) = 8.1\text{inches} = 205.7\text{mm}$ for one data set and $2(L + \rho) = 50\text{mm}$ for a second data set. The angular spacing α was varied between $\alpha = 1^\circ, 10^\circ, 20^\circ, 30^\circ, 40^\circ,$ and 50° and the far field pattern was recorded. The idea with using the biconical antennas and adjusting the angle α was to see when the algorithm would fail due to mutual coupling effects. Lastly, the gap spacing between the two halves of each antenna was somewhat arbitrarily chosen to be 0.2 mm in all cases. The impact of this gap spacing was not studied.

For simplicity and fast computation time in the simulations, a discrete port was used at the feed point. Even when using the discrete port, CST simulations generally take

much longer to run than a simple Matlab script. Therefore, only the far-zone electric fields for the antenna along the Z-axis were simulated using CST. The far-zone fields for the X-directed and the Y-directed antennas, since they are merely rotated versions of the Z-directed pattern, were obtained in Matlab using the rotation transform described in Appendix B. Also, the far-zone electric fields were simulated for the Z-antenna without it being in the presence of the other two antennas so as to avoid the effects of mutual coupling. As will be described below, this decision allowed us to run simulations both with and without mutual coupling effects. Lastly, the simulated far-zone electric fields were then converted to effective heights using (3-8) with $I_{in} = 1$ Amp, $r = 1$ meter, and $k = 2\pi/\lambda_c$.

The second major step in testing the algorithms was to irradiate the mutually orthogonal arrangement with plane waves in CST and to record the induced voltages on the terminals of the antennas. The simulations were completed both with and without mutual coupling effects. To compute the results without mutual coupling effects, uniform plane waves were radiated toward each antenna while the other two antennas were removed from the simulation. To include mutual coupling effects, all three antennas were included in the simulation at the same time. The TIME DOMAIN solver simulated the voltage response for 50ns with an accuracy threshold of -50dB. The voltage was monitored across 50Ω lumped element loads attached to the antenna terminals. The plane waves were defined using the PLANEWAVE EXCITATION feature of CST with a purely sinusoidal input signal at the desired frequency. The background was set to NORMAL (free space with $\epsilon_r = 1$, $\mu_r = 1$) and the boundary conditions were set to OPEN (ADD SPACE). The mesh grid used a HEXAHEDRAL

mesh with a MESHLINE RATIO LIMIT of 40 and LINES PER WAVELENGTH of 10. Since CST can not simulate multiple incident plane waves from different incident angles at the same time, the plane waves were simulated one at a time and the recorded voltages were then superposed in Matlab.

The third major step was to process the recorded voltages in Matlab for various signal-to-noise ratios (SNRs). In this thesis work, the SNR was computed as

$$\text{SNR} = 10 \log_{10} \left(\frac{|V_{pk}|^2}{\sigma^2} \right) = 20 \log_{10} \left(\frac{|V_{pk}|}{\sigma} \right) \quad (3-32)$$

where σ is the standard deviation of any sample of the noise and $|V_{pk}|$ is the peak magnitude of the induced voltage. The next chapter presents detailed results for each algorithm (also see Appendix C).

To compare the performance of each algorithm, we can compute the angular error ζ by taking

$$\zeta = \cos^{-1} \left(\frac{\vec{a}_{known} \cdot \vec{a}_{est}}{\|\vec{a}_{known}\| \|\vec{a}_{est}\|} \right) \quad (3-33)$$

where \vec{a}_{known} is the known direction-of-arrival vector and \vec{a}_{est} is the estimated vector. By running through each algorithm N times, we obtain a set of angular errors $\zeta_1, \zeta_2, \dots, \zeta_N$ from which we can compute the root-mean-squared error (RMSE) as

$$\text{RMSE} = \text{sqr}t \left(\frac{\sum_{n=1}^N (\zeta_n)^2}{N} \right) \quad (3-34)$$

The next chapter will present performance comparisons based on (3-34).

3.8 CONCLUSION

This chapter has described the approach and methodology used during this thesis to study direction finding (DF) with a set of mutually orthogonal antennas. First, the uniform plane wave model was defined to model the incident waves arriving at the antennas. Then, we introduced the vector effective height and used it to analyze the tripole configuration. From this analysis, we saw that the tripole can be used as a far-zone electric field probe. A simple algorithm was then pursued which can be used to locate the directions-of-arrival of incident plane waves using the tripole. The effective height was then incorporated into a maximum likelihood-based and a MUSIC-based algorithm. Finally, we explained how these algorithms were tested by first irradiating the antennas with uniform plane waves in CST Microwave Studio and then exporting the recorded voltages to Matlab for processing. The following chapters present and discuss detailed results from these simulations.

CHAPTER 4

Results & Discussion

4.1 INTRODUCTION

This chapter presents and discusses the results of the direction finding (DF) simulations described in Chapter 3. Section 4.2 gives the results of the simple direction finding algorithm offered by Equations (3-20) through (3-24) for use with the tripole. The results are compared for different signal-to-noise ratios (SNR) (as defined by (3-32)) and different axial ratios (AR) (as defined by (3-7)) of the incident plane waves. Section 4.3 contains the results from applying the maximum likelihood algorithm in Equations (3-26) through (3-28) to the mutually orthogonal dipoles, bowties, and biconical antennas for various SNR levels. Section 4.4 presents similar results obtained from applying the MUSIC algorithm from Equations (3-29) through (3-31) to the biconical antennas only. Lastly, section 4.5 presents a performance comparison based on (3-33) and (3-34)

4.2 SIMPLE TRIPOLE ALGORITHM RESULTS

In this section we examine two sets of data that were processed using the simple tripole DF algorithm described in section 3.5. The first set of data was acquired by irradiating the tripole with eight uniform plane waves (UPWs) from various directions in CST Microwaves Studio. The second set of results examines the performance of this algorithm as we increase the axial ratio of three UPWs until they are nearly linearly

polarized. To obtain this second set of data, a series of Matlab simulations were conducted. Let us begin by examining the first set of data from the eight UPWs in CST.

The eight UPW that were radiated toward the tripole in CST had the same electric field magnitude but had different axial ratios, different frequencies, and different arrival angles. Table 4 - 1 lists the parameters of each wave.

TABLE 4 - 1: Parameters of the eight UPWs incident on the tripole					
	Frequency (GHz)	Antenna Length	AR	Incident θ°	Incident ϕ°
Signal 1	0.1	0.005λ	1	10	85
Signal 2	0.3	0.015λ	3	13	320
Signal 3	0.6	0.030λ	4	29	220
Signal 4	0.9	0.045λ	1	31	220
Signal 5	1.1	0.055λ	1	30	215
Signal 6	1.2	0.060λ	1	45	20
Signal 7	1.65	0.083λ	3	68	175
Signal 8	2.2	0.110λ	2	87	5

The voltages measured on each tripole arm in CST (assumed noiseless) were exported to Matlab where random noise was added to each sample point. The noisy voltages were processed by the algorithm described in Equations (3-20) through (3-24) for SNR levels of ∞ , 40dB, 35dB, 30dB, 25dB, 20dB, 15dB, and 10dB. Figure 4 - 1 shows the power spectrum with no noise ($SNR = \infty$) where the solid red horizontal line is a simple detection threshold. Figure 4 - 2 shows a comparison between the known (circles) and estimated (plus signs) angles-of-arrival of the eight UPWs for the noise-free case. Table 4 - 2 shows the difference in degrees between the known and estimated angles-of-arrival. Figure 4 - 3 through Figure 4 - 9 show the results after running the algorithm 20 times at the SNR levels mentioned above.

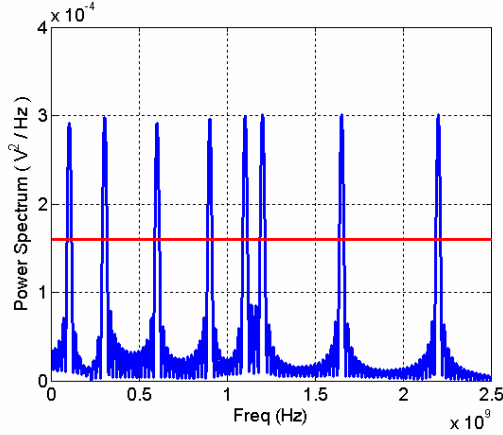


Figure 4 - 1: Noise free power spectrum of the eight UPWs simulated in CST

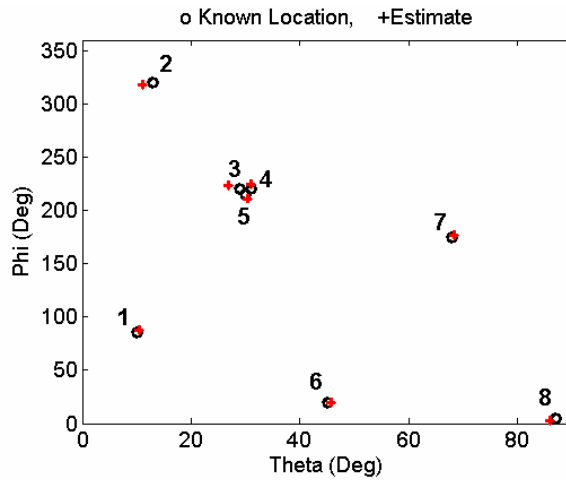


Figure 4 - 2: Known (circles) and estimated (plus signs) directions-of-arrival of the eight (numbered) UPWs for the noise free case

TABLE 4 - 2: Angular difference between known and estimated angles-of-arrival for noise-free case		
	θ - difference (deg)	ϕ - difference (deg)
Signal 1	0.44	2.49
Signal 2	-1.95	-1.54
Signal 3	-2.06	3.66
Signal 4	0.03	4.13
Signal 5	0.32	-4.12
Signal 6	0.78	-0.14
Signal 7	0.39	1.79
Signal 8	-1.01	-1.90
Root-mean-squared error	1.13	2.80

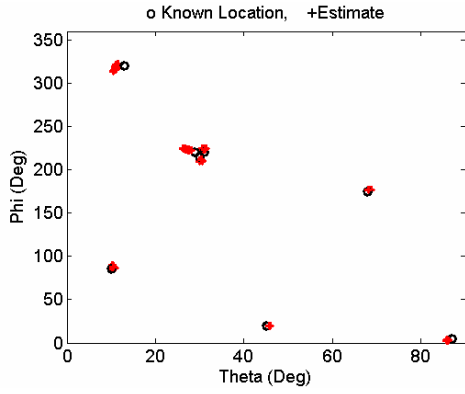


Figure 4 - 3: SNR = 40dB

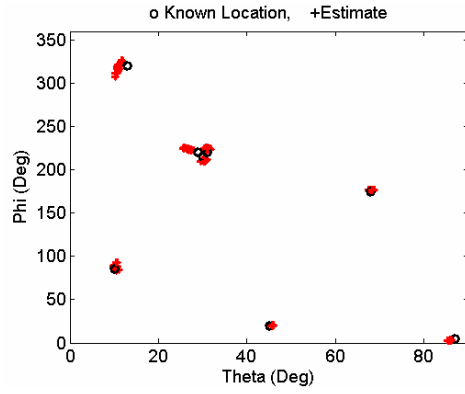


Figure 4 - 4: SNR = 35dB

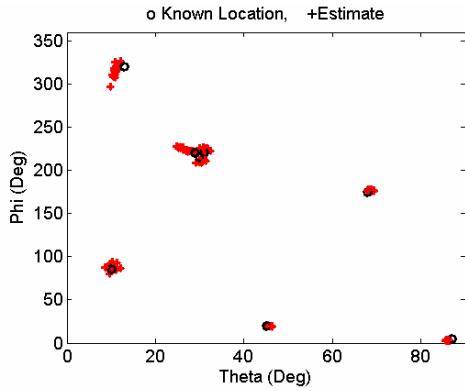


Figure 4 - 5: SNR = 30dB

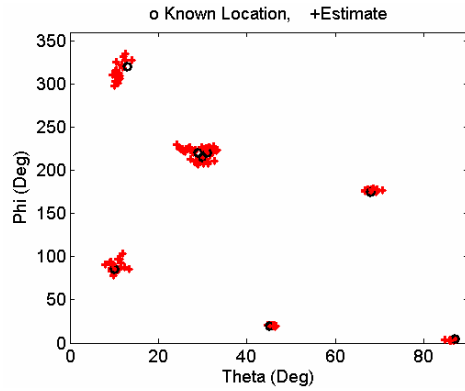


Figure 4 - 6: SNR = 25dB

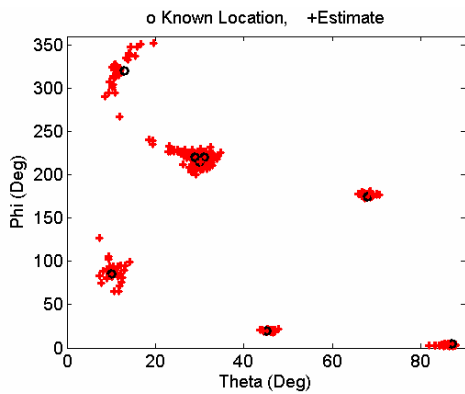


Figure 4 - 7: SNR = 20dB

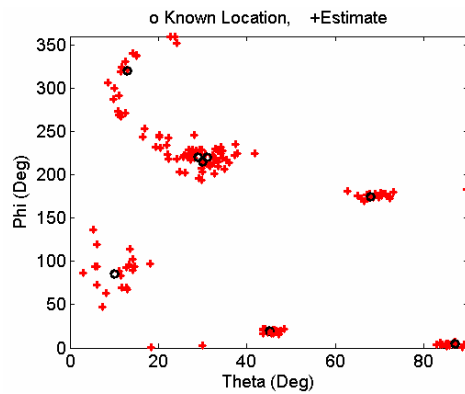


Figure 4 - 8: SNR = 15dB

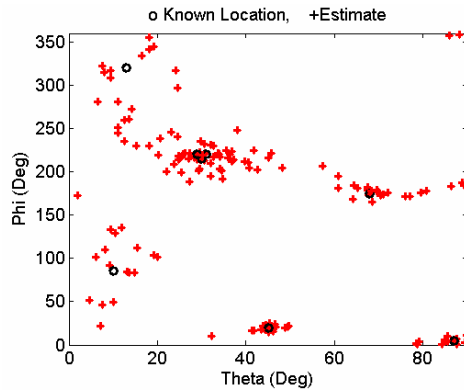


Figure 4 - 9: SNR = 10dB

The figures above give us a good feel for how much variation we can expect at the different SNR levels when using the simple tripole algorithm. The algorithm performs very well at high SNR levels where we see that the estimated angles-of-arrival are closely clustered near the noise-free estimates. When the SNR drops near 30dB and lower, we begin to see large variations in the estimates. Since the noise is assumed Gaussian with zero mean, averaging multiple estimates could be used to reduce the error. Again, the simulations above included all mutual coupling effects so we can surmise that mutual coupling is not a large problem when the SNR is high enough.

We now examine the results from applying this algorithm to three incident waves while we varied their axial ratios. The voltage on each tripole arm was simulated in Matlab using the axial ratios shown in Figure 3 - 2 with $SNR = 30dB$. The three incident waves had the same magnitude but different frequencies and arrived from (θ, ϕ) angles of $(5^\circ, 180^\circ)$, $(50^\circ, 10^\circ)$, and $(85^\circ, 345^\circ)$ respectively. Figures 4 - 10 through 4 - 15 show the results after running the simulation 50 times for each setting. Again, the circles represent the known locations of the emitters and the plus signs indicate the estimates.

SNR = 30dB

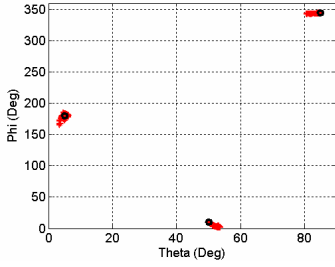


Figure 4 - 10: SNR 30dB, AR 1

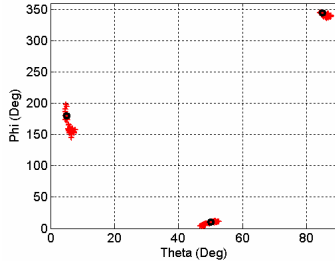


Figure 4 - 11: SNR 30dB, AR 2

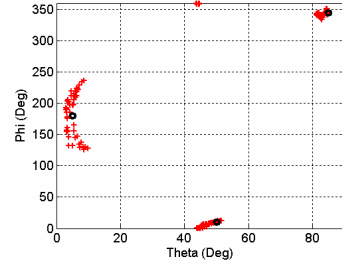


Figure 4 - 12: SNR 30dB, AR 5

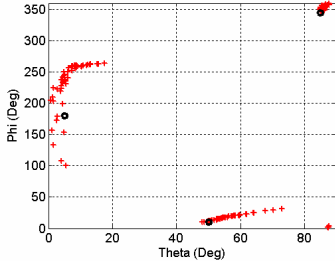


Figure 4 - 13: SNR 30dB, AR 10

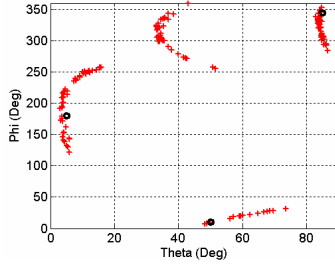


Figure 4 - 14: SNR 30dB, AR 20

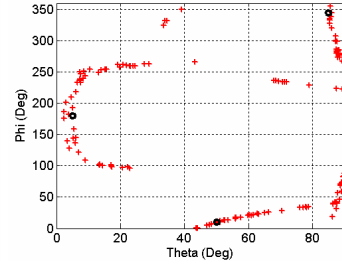


Figure 4 - 15: SNR 30dB, AR 80

These results confirm the expected poor performance of the simple tripole algorithm for highly linearly polarized waves even at high SNR levels. However, we also see that the algorithm performs very well for circularly polarized waves ($AR = 1$). Finally, we direct attention to the signal at $\theta = 5^\circ$ whose estimates begin to vary much sooner than the other two signals. From this result, we can conclude that the accuracy of the algorithm degrades as the arrival angle $\theta \rightarrow 0^\circ$. Again, this algorithm is only applicable to the tripole configuration as explained in Chapter 3. We now move to the simulation results obtained by using the maximum likelihood algorithm which is applied to the tripole, the bowtie antennas, and the biconical antennas in the orthogonal arrangement.

4.3 MAXIMUM LIKELIHOOD (ML) ALGORITHM RESULTS

This section contains and discusses the results obtained by applying the maximum likelihood (ML) algorithm outlined by Equations (3-26) through (3-28) to the orthogonal arrangement of dipole (the tripole), bowtie, and biconical antennas. For clarity, we consider only one incident wave at a time for all simulations in this section. We'll start by applying the maximum likelihood algorithm to the tripole.

ML on the Tripole

To study the performance of the maximum likelihood algorithm applied to the tripole configuration, we'll separately look at three incident signals from angles-of-arrival (θ, ϕ) of $(10^\circ, 120^\circ)$, $(45^\circ, 60^\circ)$, and $(80^\circ, 340^\circ)$ each with $AR = 1$. These UPWs were simulated in CST and noise was later added in Matlab for SNR levels of 40dB, 30dB, 20dB, and 10dB. Recall that in the maximum likelihood algorithm we seek to locate the smallest g -value from (3-28). Figures 4 - 16 through 4 - 27 show typical g -values computed at each (θ, ϕ) in the range $0^\circ \leq \theta \leq 90^\circ$ and $0^\circ \leq \phi \leq 360^\circ$ in 5° increments. Dark blue areas are relatively small g -values and dark red areas are relatively large g -values. The red circle is the known direction-of-arrival and the green plus sign is the estimated direction-of-arrival. Notice that the figures for the signal at $(80^\circ, 340^\circ)$ also have low g -values near $\phi = 180^\circ$. The reason is that the angles $(100^\circ, 160^\circ)$ also give a mathematical solution since they equate to a DOA vector opposite to that of $(80^\circ, 340^\circ)$. However, we reject this solution based on the assumption that our signal arrives from a known hemisphere. From these figures we see that the maximum likelihood gives good estimates of the direction-of-arrival when using the tripole.

ML Tripole Result: Signal at (10°, 120°)

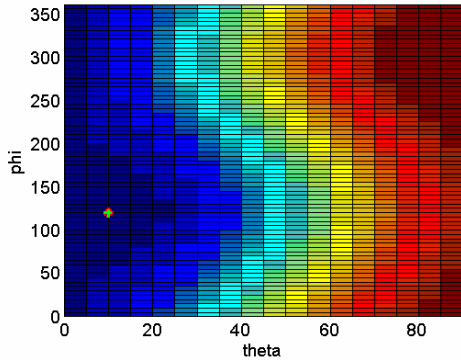


Figure 4 - 16: SNR = 40dB

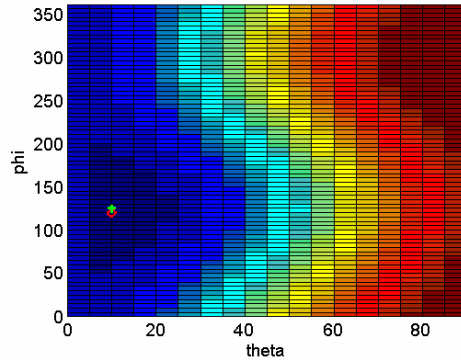


Figure 4 - 17: SNR = 30dB

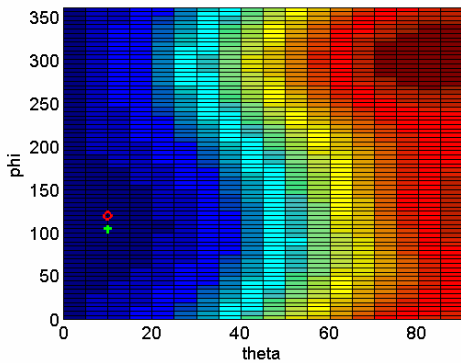


Figure 4 - 18: SNR = 20dB

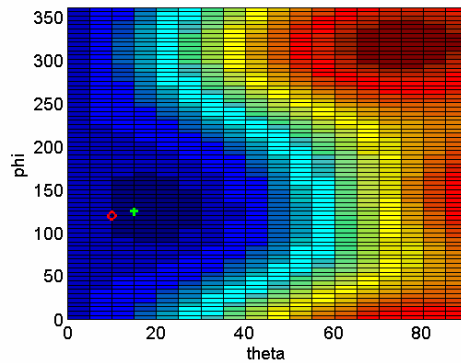


Figure 4 - 19: SNR = 10dB

ML Tripole Result: Signal at (45°, 60°)

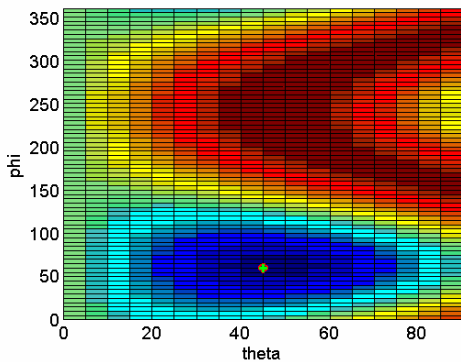


Figure 4 - 20: SNR = 40dB

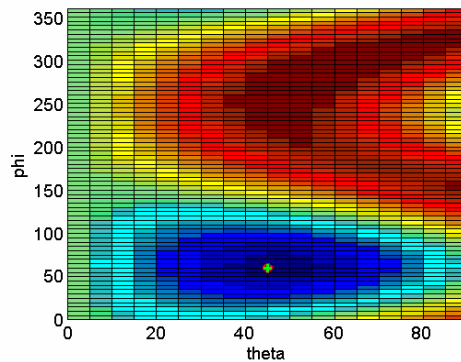


Figure 4 - 21: SNR = 30dB

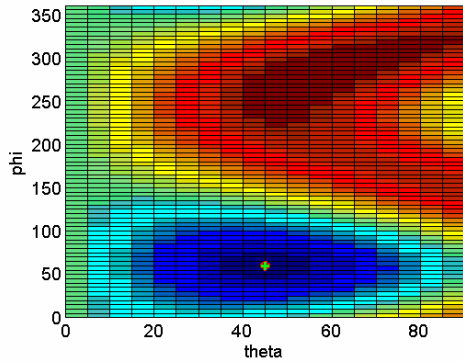


Figure 4 - 22: SNR = 20dB

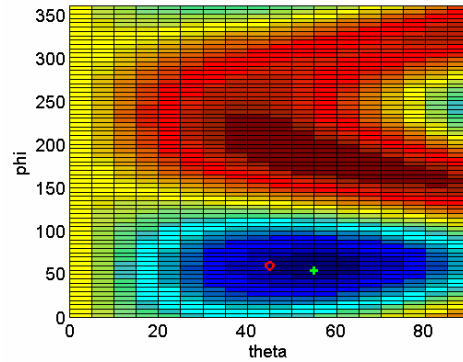


Figure 4 - 23: SNR = 10dB

ML Tripole Result: Signal at (80°, 340°)

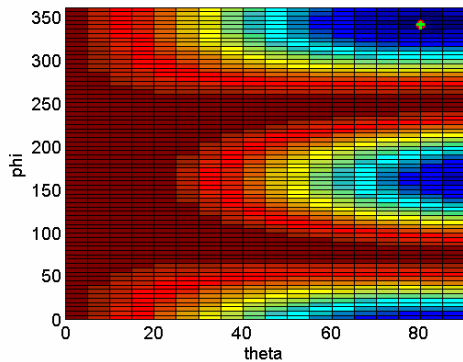


Figure 4 - 24: SNR = 40dB

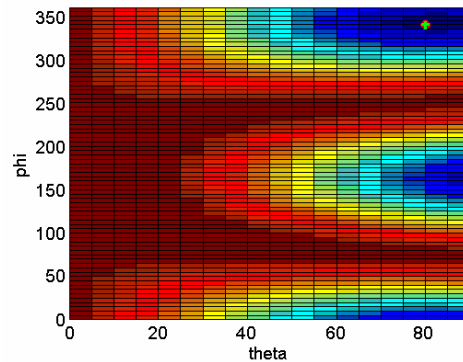


Figure 4 - 25: SNR = 30dB

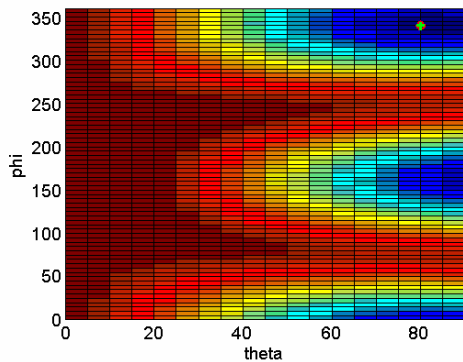


Figure 4 - 26: SNR = 20dB

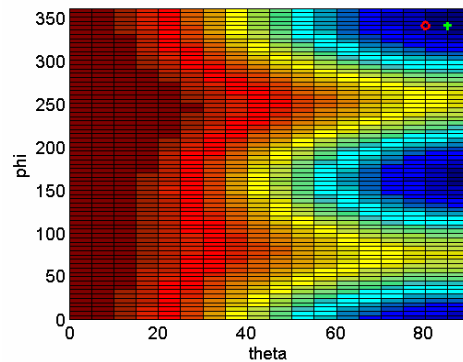


Figure 4 - 27: SNR = 10dB

It is also worth looking at how the tripole performs with the maximum likelihood algorithm when the axial ratio of the incident wave is varied. Here we take the signal at (45°, 60°) with $AR = 1, 2, 5, 10, 20,$ and 80 . Since we only want to observe the general behavior of the g -value contour plot for varying axial ratios, the SNR was set to infinity.

Figures 4 - 28 through 4 - 33 show the simulated results from which we see that the blue areas on the graph grow in size as $AR \rightarrow \infty$ which suggests there are many (θ, ϕ) combinations with relatively low g -values for highly linearly polarized waves.

ML Tripole Result: Varying AR

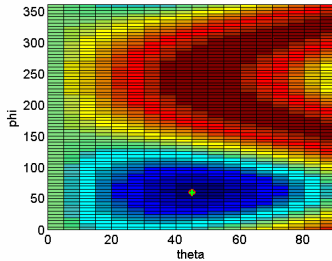


Figure 4 - 28: AR = 1

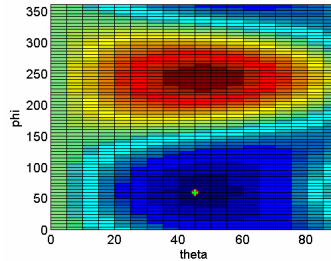


Figure 4 - 29: AR = 2

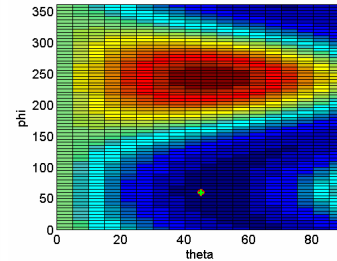


Figure 4 - 30: AR = 5

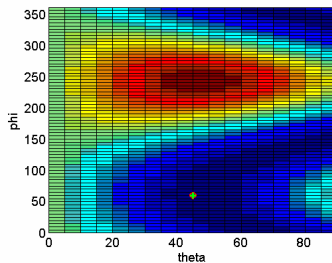


Figure 4 - 31: AR = 10

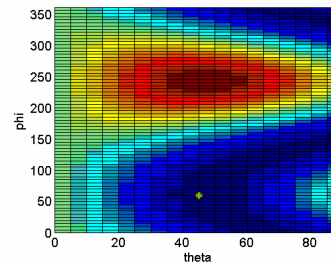


Figure 4 - 32: AR = 20

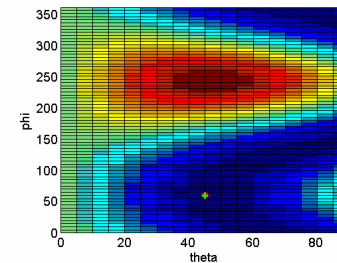


Figure 4 - 33: AR = 80

ML on Bowtie Antennas

We turn now to an examination of the results from applying the maximum likelihood algorithm to the simulated voltages on the bowtie antennas of Figure 3 - 5 with angular spacing $\alpha = 45^\circ$. To study this configuration, the bowtie antennas were irradiated with nine circularly polarized ($AR = 1$) UPWs with the parameters listed in table 4 - 3. The UPWs had the same electric field magnitude and were simulated one-at-a-time in CST. No noise was added ($SNR = \infty$) and the simulated voltages were not superposed in Matlab. Figures 4 - 34 through 4 - 42 show the results where, again, the red circle is the known location of the source and the green plus sign is the estimate.

TABLE 4 - 3: Parameters of the nine UPWs incident on the bowties				
	Frequency (GHz)	Antenna Length	Incident θ°	Incident ϕ°
Signal 1	0.7	0.96λ	45	120
Signal 2	1.0	1.37λ	45	0
Signal 3	1.3	1.78λ	80	340
Signal 4	1.5	2.06λ	45	300
Signal 5	1.8	2.47λ	10	120
Signal 6	2.1	2.88λ	60	30
Signal 7	2.4	3.29λ	70	80
Signal 8	2.8	3.84λ	20	160
Signal 9	3	4.11λ	35	250

ML Bowtie Antenna Results

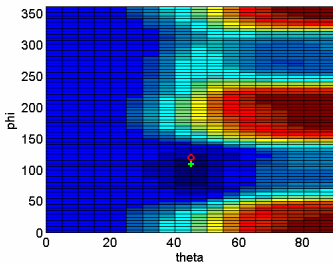


Figure 4 - 34: Signal 1

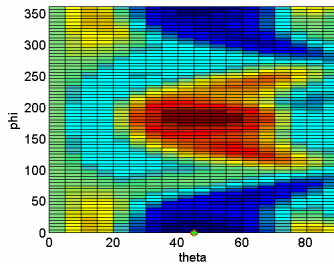


Figure 4 - 35: Signal 2

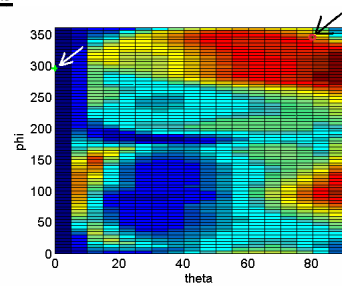


Figure 4 - 36: Signal 3

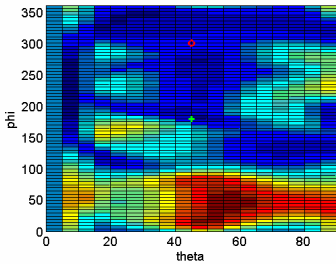


Figure 4 - 37: Signal 4

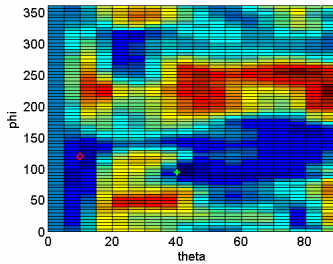


Figure 4 - 38: Signal 5

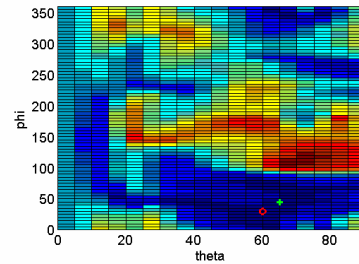


Figure 4 - 39: Signal 6

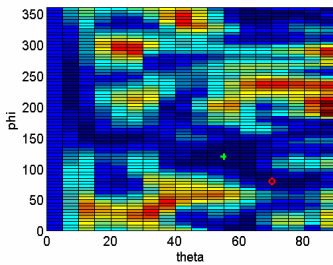


Figure 4 - 40: Signal 7

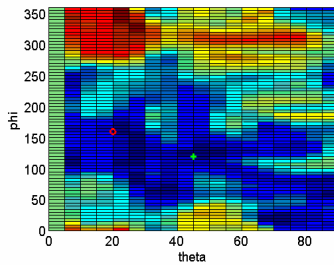


Figure 4 - 41: Signal 8

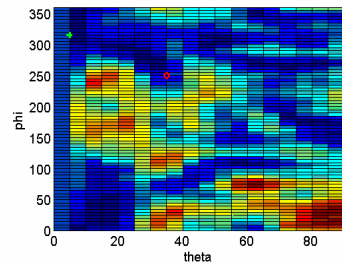


Figure 4 - 42: Signal 9

Although the directions-of-arrival for signal 1 and signal 2 were estimated fairly well, the other figures above show the general poor performance of the ML algorithm

when applied to the bowtie antennas as we have done. In signals 4 through 9, there are many (θ, ϕ) combinations that produce relatively low g -values as indicated by the blue areas that are scattered almost randomly throughout the surface. These surfaces also make sharp transitions between the large and small g -values. Contrast this with the dipole results in Figures 4 - 16 through 4 - 27 which showed a smooth and gradually changing surface.

Upon seeing these poor results, the author could think of two possible causes. The first possible cause was that the mutual coupling between the bowtie antenna elements was distorting their radiation characteristics. As explained in Chapter 3, the radiation pattern of each bowtie antenna was simulated in CST when not in the presence of the other two antennas so that no mutual coupling was included when computing their effective heights. When the bowties were irradiated with the UPWs to test the algorithm, all three antennas were present and mutual coupling was included. This was the same approach that was applied to the dipoles where we saw that the mutual coupling did not present a large problem. The second possible cause considered by the author was that the poor results were due to the bowtie antennas being too large compared to the incident wavelength. With a tip-to-tip length of 16.2 inches (≈ 411 mm), they are electrically 0.96λ at the lowest frequency of 0.7GHz and they are 4.1λ at the highest frequency of 3.0GHz (λ is the wavelength). Contrast this with the tripole case where the dipole elements, being only 15mm in total length (0.15λ at 3GHz), were very small compared to the incident signals' wavelengths. When the antennas are electrically large, we are no longer measuring the electric field at a single point in space as desired.

To examine these two possible causes, we work with biconical antennas instead of the bowties. The biconical antennas were selected because they are very similar to the dipole antennas when the angle α (see Figure 3 -5) is small. Since the mutual coupling was not a large problem with the tripole case, we expect that we should be able to gradually widen α until the mutual coupling causes errors. In addition, using two sizes (a 205.7mm set and a 50mm set) allows us to study the impact of the antenna's electrical size. The next section describes the results.

ML on the Biconical Antennas

Two sets of biconical antennas were studied (see Figure 3 - 5 for the antenna dimensions). The first set of antennas each had a tip-to-tip length of $2(L + \rho) = 8.1$ inches = 205.7mm which is close to the size of the wideband antennas mentioned in Chapter 1 (also see Appendix A). The second set of biconical antennas had a length of $2(L + \rho) = 50$ mm. The cone angle α was varied between $\alpha = 1^\circ, 10^\circ, 20^\circ, 30^\circ, 40^\circ,$ and 50° for each of the incident UPWs listed in table 4 - 4. All UPW were circularly polarized ($AR = 1$) with the same electric field magnitude. No noise was added ($SNR = \infty$) to the simulated voltages. The results were obtained both with and without mutual coupling effects. To compute the results without mutual coupling effects, uniform plane waves were radiated toward each antenna while the other two antennas were removed from the simulation. To include mutual coupling effects, all three antennas were included in the simulation at the same time. Figures 4 - 43 through 4 - 48 show a few representative examples from which to draw our conclusions. The complete listing of results is presented in Appendix C.

TABLE 4 - 4: Parameters of the UPWs incident on the biconical antennas					
	Frequency (GHz)	205.7mm antenna length	50mm antenna length	Incident θ°	Incident ϕ°
Signal 1	0.5	0.34λ	0.08λ	50	210
Signal 2	1.0	0.69λ	0.17λ	50	210
Signal 3	1.5	1.03λ	0.25λ	50	210
Signal 4	2.0	1.37λ	0.33λ	50	210
Signal 5	2.5	1.71λ	0.42λ	50	210
Signal 6	3.0	2.06λ	0.50λ	50	210

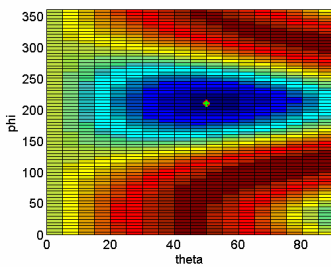


Figure 4 - 43: 205mm antenna, $f=0.5\text{GHz}$, $\alpha=50^\circ$, no mutual coupling

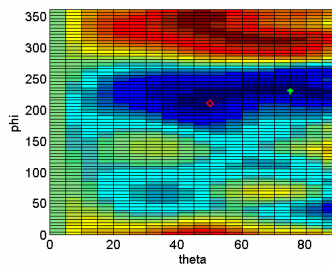


Figure 4 - 44: 205mm antenna, $f=3\text{GHz}$, $\alpha=50^\circ$, no mutual coupling

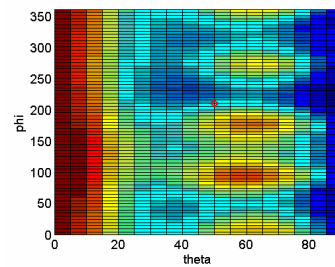


Figure 4 - 45: 205mm antenna, $f=3\text{GHz}$, $\alpha=50^\circ$, mutual coupling included

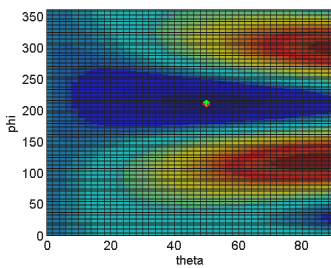


Figure 4 - 46: 50mm antenna, $f=0.5\text{GHz}$, $\alpha=50^\circ$, mutual coupling included

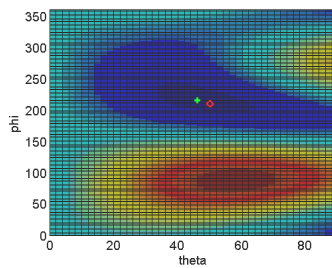


Figure 4 - 47: 50mm antenna, $f=1.5\text{GHz}$, $\alpha=50^\circ$, mutual coupling included

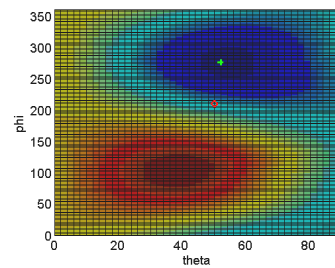


Figure 4 - 48: 50mm antenna, $f=3\text{GHz}$, $\alpha=50^\circ$, mutual coupling included

From these figures, we see that even when no mutual coupling is included, the 205mm antennas inaccurately estimate the direction-of-arrival when the size of the antennas is large compared to wavelength. This suggests that the large electrical size is indeed problematic. To see the impact of mutual coupling, we can compare two plots that have identical parameters except that one has been computed without mutual coupling and the other has included mutual coupling effects. Figures 4 - 44 and 4 - 45

are two representative examples which look significantly different from each other. This suggests that mutual coupling is also a problem; especially when the electrical size of the antennas is increased.

Examining the 50mm antenna results, we see that they accurately estimate the direction-of-arrival for all signals in table 4-4 when no mutual coupling is included (not shown here, see Appendix C). However, when mutual coupling effects are included, their performance degrades as the electrical size of the antennas is increased. We also see that the cone spacing α has very little impact on the performance even when mutual coupling is included in the simulation.

From these observations, we can deduce that our arrangement of mutual orthogonal antennas works best when the size of the antenna elements is small compared to the wavelength of the incident signal's carrier frequency. In the following section, we apply the MUSIC algorithm to the 50mm antennas.

4.4 MUSIC ALGORITHM RESULTS

This section presents the results from applying the MUSIC algorithm outlined in Equations (3-29) through (3-31) to the same simulated data described in the previous section. In these results, all mutual coupling effects were included and the $SNR = 35\text{dB}$. To save space, we only present a few representative results using the 50mm biconical antennas and the same six incident signals contained in table 4 - 4. See Appendix C for a more complete listing of results.

Recall that in the MUSIC algorithm we are trying to locate the peaks of the MUSIC spectrum expressed by (3-31). Figure 4 - 49 shows an image of the MUSIC

spectrum for signal 1 with $\alpha = 1^\circ$. Although we clearly see the sharp peak near the incident direction, it is difficult to see if the peak aligns with the known direction-of-arrival. To clearly compare the known against the estimated direction-of-arrival, a zoomed-in 2D plot of the same simulation result is shown in Figure 4 - 50 where the circle is the known direction-of-arrival and the green plus is the estimate. Figures 4 - 51 and 4 - 52 show a couple more 2D images of typical results.

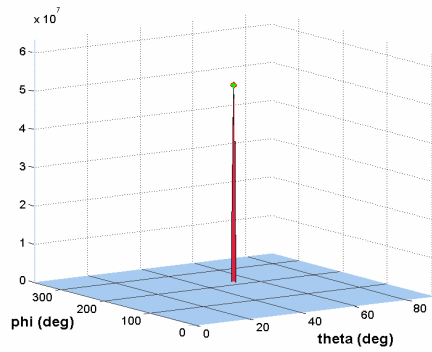


Figure 4 - 49: MUSIC spectrum of signal 1 ($\alpha=1^\circ$) showing sharp peak at the direction-of-arrival

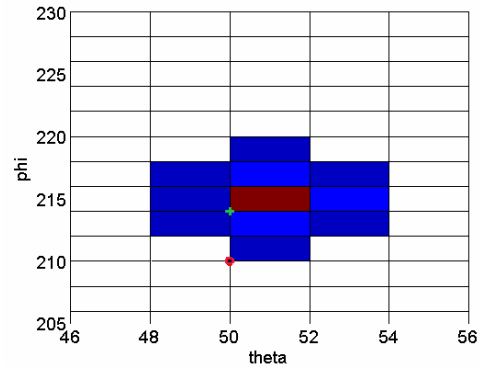


Figure 4 - 50: 2D version of the MUSIC spectrum of signal 1 ($\alpha=1^\circ$) which clearly shows the difference between the known (circle) and estimated (plus) direction-of-arrival

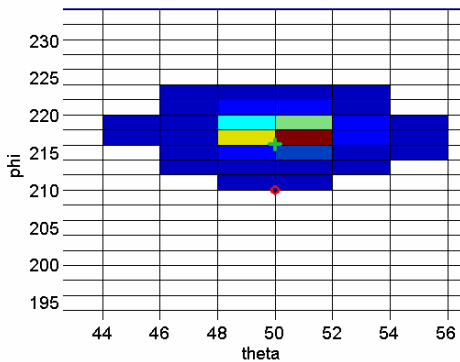


Figure 4 - 51: MUSIC spectrum of signal 3 ($\alpha=30^\circ$)

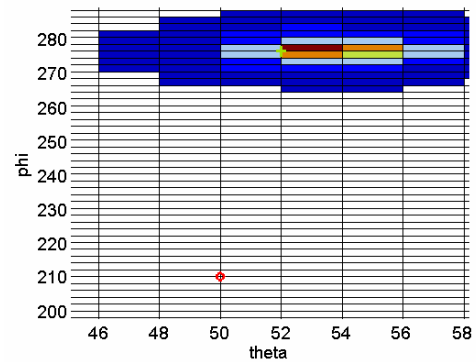


Figure 4 - 52: MUSIC spectrum of signal 6 ($\alpha = 50^\circ$)

These results show that the MUSIC algorithm estimated the direction-of-arrival to within 5° for the biconical configuration when the frequency of the incident wave was

0.5GHz. It should be noted that more accurate estimates are likely since the effective heights were saved in 5° increments which restricted the possible direction-of-arrival estimates to those locations. However, the estimates clearly degrade rapidly when the frequency is increased.

4.5 PERFORMANCE COMPARISON

In this section we present a brief performance comparison based on (3-33) and (3-34). Each of the three algorithms was applied to the tripole configuration for a signal that was incident from known angles $(\theta, \phi) = (40^\circ, 50^\circ)$ with a circularly polarized electric field. To compute the root-mean-squared error (RMSE) from (3-34), each algorithm was executed $N = 200$ times for $0 < SNR \leq 60$ dB. Figure 4 - 53 shows a comparison plot from which we see that the maximum likelihood provides the most accurate estimates. We also notice that the RMSE does not reach zero as SNR increases which indicates some bias is present in the direction-of-arrival estimates.

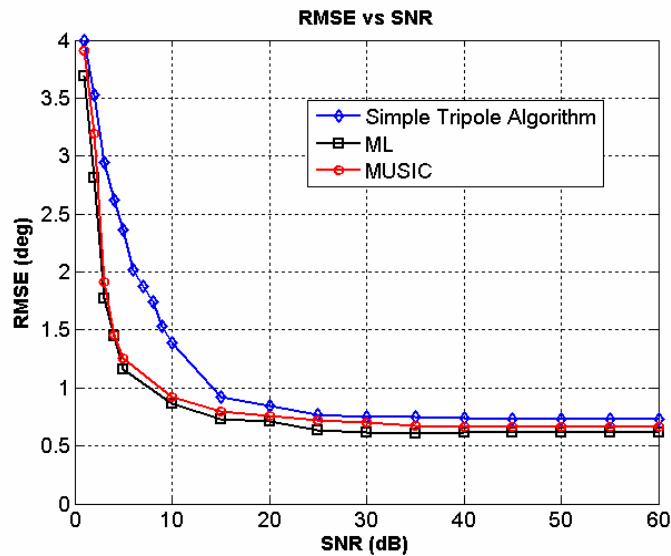


Figure 4 - 53: RMSE (deg) vs SNR (dB), $(\theta, \phi) = (40^\circ, 50^\circ)$

4.6 FURTHER DISCUSSION

For each of the algorithms studied in this thesis, we are attempting to estimate the direction-of-arrival using only the polarization information at a single point in space for each incident plane wave. One may wonder if there is an optimal antenna that can obtain the best possible measurement of the polarization properties. A search for this optimal antenna was not conducted during this thesis. However, based on the simulation results, we see that small dipole or small biconical antennas are well suited for this application. Being electrically small, they are close to satisfying the assumption that we are measuring the electric field at a single point in space. In addition, the problem of mutual coupling between antenna elements is minor when the antennas are small as seen from the simulations. If they remain electrically small for all frequencies of interest, their effective heights remain essentially unchanged. This would be very beneficial since it would negate the requirement to build numerous tables containing the effective heights at each frequency and each (θ, ϕ) combination of interest.

Another point of discussion is the fact that we are using both the maximum likelihood and MUSIC algorithms to locate the direction-of-arrival of a single UPW. This is very different from the conventional practice which utilizes these algorithms to estimate the directions-of-arrival of several signals that have the same carrier frequency. By applying the two algorithms to the mutually orthogonal arrangement of antennas, we have achieved a much smaller array size at the cost of a high computational burden. The maximum likelihood algorithm in particular, since it must perform a grid search over all (θ, ϕ) for each of the K snapshots, is very computationally expensive. The MUSIC algorithm only needs to perform the grid search once but requires many snapshots of data

in order to estimate the covariance matrix. Both algorithms are slower than more efficient classical methods using spatially separated antennas to estimate the direction-of-arrival for a single incident wave.

4.7 CONCLUSION

This chapter has presented the simulation results for each of the three direction finding algorithms studied in this thesis. The simple tripole algorithm was able to estimate the direction-of-arrival of uniform plane waves to within 1° in the absence of noise when the waves were circularly polarized. The performance was shown to degrade as the axial ratio of the incident wave is increased, the arrival angle $\theta \rightarrow 0^\circ$, or the *SNR* $\rightarrow 0$.

The results from the maximum likelihood algorithm were quite varied. When applied to the short dipoles, the maximum likelihood algorithm produced smooth looking *g*-value plots having a global minimum near the known direction-of-arrival. Performance degradation was similar to the simple tripole algorithm. However, when the maximum likelihood algorithm was applied to electrically large antennas (bowties and biconicals), the resulting *g*-value plots produced erroneous estimates of the direction-of-arrival. Although the large size of the antennas was shown to be the main cause of the problem, distortions due to mutual coupling were also present. However, the simulation results also suggest that the mutual coupling problem is less severe when the antenna elements are small compared to the incident signal's wavelength.

The MUSIC algorithm was shown to estimate the direction-of-arrival to within 5° when applied to the 50mm biconical antennas for a circularly polarized wave at 0.5GHz.

However, more accurate estimates are likely since the effective heights were saved in 5° increments which restricted the possible direction-of-arrival estimates to those locations.

From the simulation results presented, we can conclude that the arrangement of mutual orthogonal antennas works best when the size of the antenna elements is small compared to the incident wavelength. A performance comparison using the tripole configuration showed that each algorithm can estimate the direction-of-arrival with a root-mean-squared error of 1° or less when the incident wave is circularly polarized, the antennas are small compared to wavelength, and the signal-to-noise ratio is above 20dB.

CHAPTER 5

Concluding Remarks and Future Work

5.1 CONCLUDING REMARKS

This thesis has examined direction finding (DF) with three mutually orthogonal antennas. Since the thesis sponsor's eventual goal was to use a set of wideband blade antennas in the envisioned system described in Chapter 1, the DF problem was formulated using the vector effective height concept from antenna theory. The hope was that this approach would allow for easy incorporation of any antenna into the model.

With this goal in mind, three algorithms and three types of antennas were studied. Each algorithm relies entirely on the information contained in the incident electric field's polarization behavior since no propagation delay can be measured. In all the algorithms, we assume that the narrowband signal model applies and that we can separate multiple incident waves in the frequency domain before processing each signal separately.

The first algorithm that was developed during this thesis is only applicable to the mutually orthogonal arrangement of short (Hertzian) dipoles (i.e., the tripole). It works by measuring the electric field locus at a single point in space and then computing a direction-of-arrival (DOA) vector that is perpendicular to the plane containing the locus. The fast Fourier transform is used to locate signals in the frequency domain and a closed form expression is used to compute the DOA. This approach appears considerably simpler than previous solutions by other researchers who have studied this antenna configuration.

The second and third algorithms are based on the maximum likelihood (ML) technique and the MUSIC technique, respectively. In the literature, these two algorithms have been used in conjunction with many antenna elements to locate several signals that have the same carrier frequency. However, in this thesis, these two algorithms were adapted to the mutually orthogonal arrangement of antennas and used to locate a single signal. In doing so, we have achieved a much smaller antenna arrangement at the cost of a higher computational burden.

The formulation of the ML and MUSIC algorithms in this thesis was intended to allow them to be adapted to any antenna that is placed in the orthogonal arrangement. However, this proved to be unsuccessful since it was discovered that the electric size of the antennas is a critical factor in the performance of these algorithms. The algorithms were developed with the assumption that we are measuring the electric field at a single point in space. When the frequency is low and the antennas are small compared to wavelength, this approximation is valid as evidenced from the simulation results. However, when the frequency of operation is increased, the electrical size also increases and the *single point in space* assumption no longer applies. Mutual coupling is also noticeable when the antennas are large. Therefore, these two algorithms, as formulated in this thesis, should only be applied to antennas that are electrically small.

For the envisioned system, which is intended to operate from 0.03 GHz to 3 GHz, the physical size of the wideband antennas mentioned in Chapter 1 (also see Appendix A) reach a half-wavelength at roughly 0.73 GHz. In other words, they become *large* quickly as the frequency is increased. Operating (or receiving) at frequencies near and above this level will give inaccurate DOA estimates. Based on the performance of the bowtie and

biconical antennas that were sized to closely match the wideband antennas, we can safely recommend that the wideband antennas should not be used in the orthogonal arrangement. However, other antennas such as dipoles or biconical antennas should work well in this arrangement if they are kept small compared to wavelength.

Simulation-based testing of each algorithm, as carried out in CST Microwave Studio and Matlab, showed that each algorithm performs best when the incident waves are circularly polarized (axial ratio $AR = 1$), the signal-to-noise ratio is relatively high ($SNR \geq 20\text{dB}$), and the antenna elements are small compared to the incident wavelength. When these conditions are met, direction-of-arrival estimates with a root-mean-squared error within 1° or less are possible with each algorithm. However, the accuracy of the estimates degrades as the $AR \rightarrow \infty$ or the $SNR \rightarrow 0$. The accuracy also degrades when the incident angle $\theta \rightarrow 0^\circ$ but this can be avoided by physically rotating the z-axis away from the direction-of-arrival.

5.2 FUTURE WORK POSSIBILITIES

The theoretical development contained in this thesis has left room for many possibilities of future work. One area of future work is to develop the theory for dealing with multipath reflections. In this thesis, the detected signals were assumed to have arrived at our receiving antennas from a straight line-of-sight path. In practice, the signal could follow multiple paths before striking our antennas. For a stationary receiver on the ground, a 2-ray model could be incorporated to account for the reflection of the plane wave along the ground. If the receiver is attached to a UAV platform, the reflections caused by mountainous terrain could be studied. Other possibilities for future theoretical

improvements could be to incorporate the Doppler effect into the model since the envisioned system described in Chapter 1 would be attached to a moving UAV platform. If several UAVs are equipped with the system, someone could study methods to coordinate their measurements to perform geolocation of the transmitting source.

One problem with all the algorithms presented in this thesis is that they break down for linearly polarized waves. To combat this problem, an area of future research could be to look for ways to intentionally change the incident linearly polarized waves into elliptically polarized (or circularly polarized) waves. One idea to achieve this effect is to develop a radome structure that converts the linearly polarized waves to elliptically polarized waves without changing the direction-of-arrival. Another idea is to take advantage of naturally occurring phenomenon that change the polarization such as reflecting signals off the ionosphere.

Another way to overcome the problem of linearly polarized waves is to investigate the performance of several sets of mutually orthogonal antennas that are arranged into an array. Using multiple sets of spatially separated tripoles, for example, would add propagation delay information which, in addition to the polarization information captured by each tripole, could yield better direction-of-arrival estimates.

Still another future work possibility is to research an ESPRIT-like algorithm for use with our antenna arrangement. Recall that the ESPRIT technique exploits the *rotational invariance* of several identical antenna arrays that have been shifted in space but not rotated. Intuition suggests that there should be a *spatial invariance* approach that exploits the fact that our identical antennas have been rotated but not shifted in space. The rotation transform matrix described in Appendix B provides a starting point to

investigate this idea. Another approach would be to develop the theory using quaternions instead of the Euler angles from the rotation transform.

Finally, for those who are interested in working with hardware, a future AFIT thesis possibility could focus on integrating the antennas, receivers, and DF algorithms into the prototype system envisioned in Chapter 1. Testing the prototype system in an outdoor range could be accomplished using simple, hand-held push-to-talk radios that have been modified to radiate electromagnetic fields with user-defined axial ratios.

APPENDIX A

Wideband Antenna Simulations & Measurements

A.1 INTRODUCTION

This appendix describes the modeling, simulation, and measurement of the wideband antennas mentioned in the main body of the thesis. These antennas were developed by an aeronautical systems contractor for use in a direction finding (DF) system. The sponsor of this thesis wanted to know if these antennas could be used in a mutually orthogonal arrangement. Although the focus of this thesis work was on DF with an arbitrary set of mutually orthogonal antennas in general, there was still some work aimed at understanding the performance of these particular antennas. That work is summarized here and should be useful for future researchers at AFIT and AFRL who plan to incorporate these antennas into a prototype system.

There were actually two types of wideband antennas developed by the contractor. Figure A-1 shows a photograph of the two antenna types. The larger antennas, referred to as type 1, are intended to operate from 0.03GHz to 0.5GHz. These type 1 antennas were designed to be conductively mounted on an aircraft which allows them to use the currents excited in the airframe skin from the incident electromagnetic signals. The type 1 antennas require this *structural excitation* at frequencies below 0.2GHz. The smaller of

the two types, referred to as type 2, are specified for operation from 0.5GHz to 3GHz. The type 2 antennas do not use the structural excitation technology.

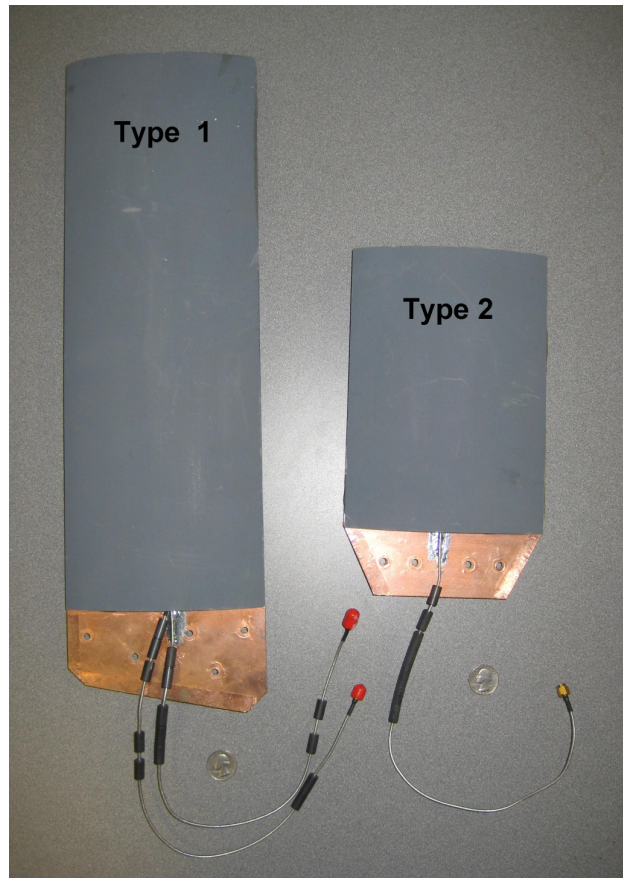


Figure A - 1: Photograph of the two different types of wideband antennas.

In the presentation that follows, only the type 2 antennas will be considered. There were several reasons for this decision. First, the lower operating frequency of the type 1 antennas prevents them from being measurable inside the locally available anechoic chambers. Second, since the type 2 antennas don't need the structural excitation, they can be studied without mounting them on an airframe. Third, the type 2 antennas have a single feed line whereas the type 1 antennas have the added complexity of two feed lines. Fourth, the type 2 antennas are specified to operate over their entire frequency range with

out any matching circuitry when connected to a standard 50Ω load. Lastly, the smaller size of the type 2 antennas allows for faster simulations in CST Microwave Studio software.

The modeling and simulation of the type 2 antennas was carried out in CST Microwave Studio software where the current distribution, far-field pattern, and scattering parameters (reflection coefficient S_{11}) were studied. The far-field pattern and the S_{11} were then measured in the AFRL's RASCAL anechoic chamber. Note that the physical measurements on the far-field pattern were limited to frequencies above 1GHz due to the size of the anechoic chamber. In the next section, we begin the modeling and simulation discussion by examining the mathematical expression for the antenna's shape.

A.2 MATHEMATICAL EXPRESSION FOR THE ANTENNA SHAPE

In order to model the behavior of the wideband type 2 antennas, it was necessary to know the physical geometry of the radiating structure. However, the radiating structure of these antennas was covered by protective foam which prevented direct measurements of antenna's shape. Therefore, several x-ray images were taken to reveal the shape of the antenna. The physical dimensions of the antenna were then approximated by overlaying a grid on an x-ray image and measuring several sample points along the outer parameter of the radiating structure. Figure A-2(b) shows a photograph of the x-ray image. The light, oval, *paddle* shape is the radiating copper while the darker surrounding areas are the dielectric. The bright white spot at the bottom of the image is the thin center conductor of the coax feed line that has been covered with electrical solder. The

radiating copper only exists on one side of the dielectric (contrast this with a typical patch antenna that has a ground plane under the radiating structure [35: 210]).

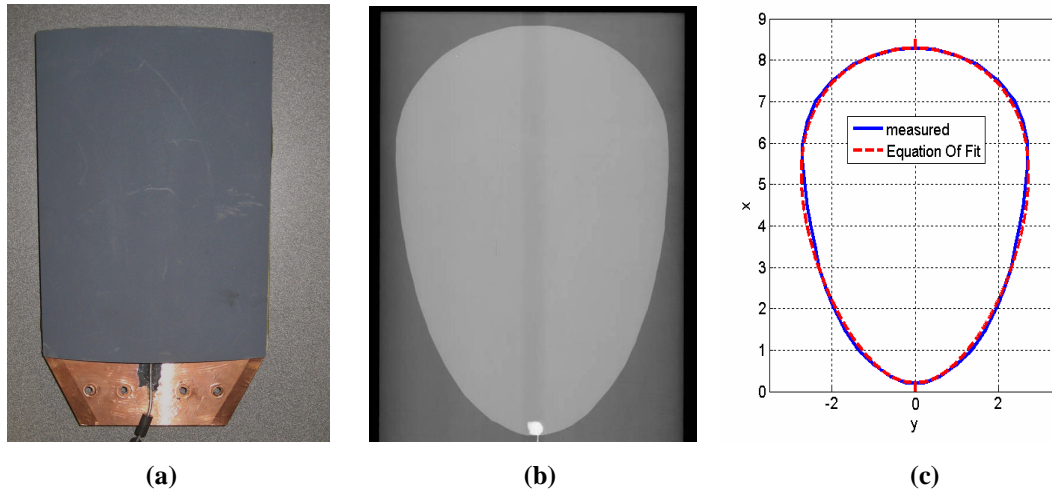


Figure A - 2: Type 2 antenna

- (a) Photograph
- (b) X-ray image
- (c) Plot showing equation of fit (axes in inches)

The radiating structure resembles an ellipse that has been modified into the shape of a flattened egg. Using the measured points on the grid, along with the equation for a modified ellipse, the following equation was obtained to mathematically describe the antenna shape

$$y = \sqrt{\frac{4}{e^{-0.13x}} \cdot \frac{1 - (x - 4.05)^2}{16.3}} \quad (\text{A-1})$$

The expression in (A-1) is valid only for positive x and y values. However, by reflecting this equation across the x-axis, we can reconstruct a shape similar to the measured dimensions. Plotting (A-1) in Matlab (along with the reflection through the x-axis)

produces the plot in Figure A-2(c) which closely resembles the real antenna shape. This expression was used to define the shape of the antenna in CST Microwave Studio software which is discussed next.

A.3 MODELING & SIMULATION OF THE WIDEBAND ANTENNAS

This section examines the modeling and simulation of the wideband antennas as carried out in CST Microwave Studio software. The modeling of the structure will be described first followed by a description of the relevant simulation parameters. An examination of the current distribution at various frequencies is also included here. The far-field patterns and the reflection coefficient (S11) are presented in section A.5 where they are compared to the measured data.

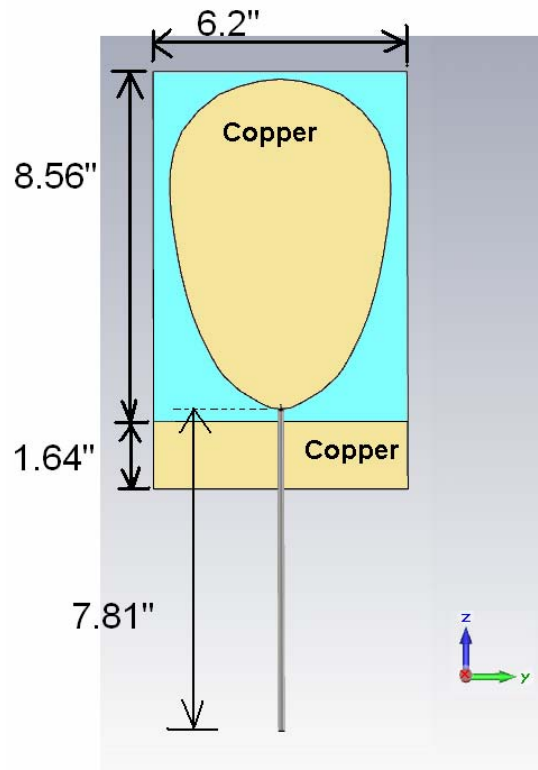


Figure A - 3: CST model of the type 2 antenna with important dimensions

The model began by building the radiating and dielectric structures inside the CST software. Figure A-3 shows an image of the antenna model with the important physical dimensions measured in inches. Using equation (A-1), the radiating *paddle* structure (0.0135 inches thick) was defined using the “extrude” command and the material was set to copper. The *paddle* was placed on a rectangular dielectric block having an assumed duroid 5880 composition (relative permittivity of $\epsilon_r = 2.2$, loss tangent $\tan\delta = 0.0009$). The dielectric block (blue color in Figure A-3) was built with physical dimensions of $10.2'' \times 6.2'' \times 0.1''$. The lower end of the dielectric block, which will be referred to as the ground, was covered with another thin copper layer.

Several details about the antennas were either assumed or ignored in the model. Most importantly, the electrical parameters for the dielectric (assumed Duroid 5880) and the outer protective foam were assumed since measuring these parameters would have required destroying an antenna. Since the outer protective foam had an assumed relative permittivity and relative permeability of $\epsilon_r = 1$ and $\mu_r = 1$ respectively, it was not included in the CST model. Lastly, the actual antennas use some kind of adhesive bonding glue to attach the radiating paddle to the dielectric. This glue was not modeled.

Once the main structure was defined, work began on building the coaxial cable and connecting it to the radiating structure. Using the dimensions listed in the data sheet of the Belden-N1671A coax cable connected to the actual antennas, the coaxial line was modeled in CST with the dimensions $a = 0.02''$, $b = 0.062''$, and $c = 0.085''$ as shown in

Figure A-4. The outer and inner conductor were modeled with PEC and the dielectric was modeled with Teflon ($\epsilon_r = 2.1$, $\mu_r = 1.0$, $\tan\delta = 0.0002$).

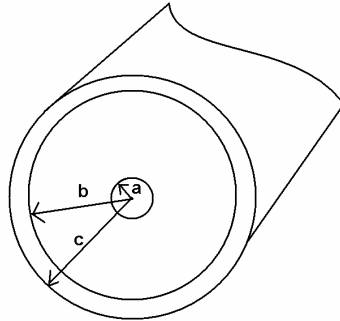


Figure A - 4: Coax cable dimensions

The outer shield of the coax was attached to the ground by overlapping the two metal layers slightly (i.e., physical contact). The center conductor of the coax line was connected to the *paddle* metallization in a similar way. The connecting solder that holds these connections on the real antenna was not modeled in CST. Finally, a waveguide port was used as the feed port in the simulations. Figure A-5 shows the spacing dimensions of the connection between the coaxial feed line and the paddle structure. Figure A-6 shows an alternative perspective of the feed connection.

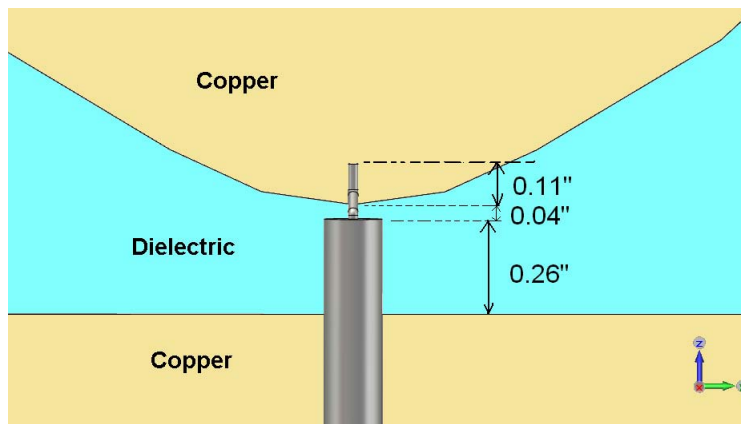


Figure A - 5: Feed point with important dimensions

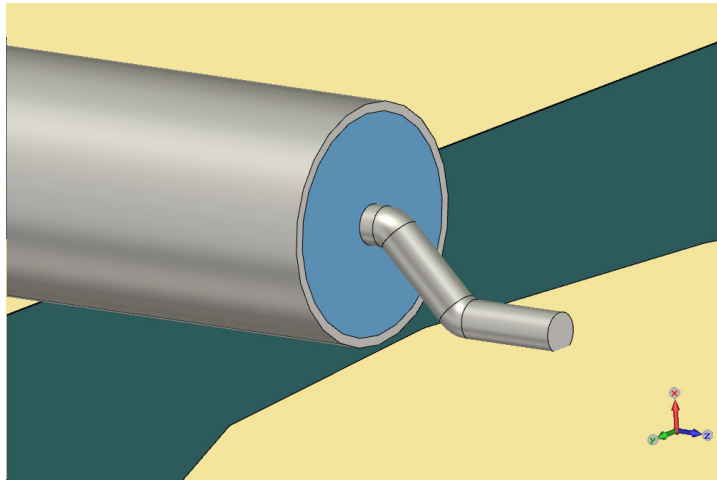


Figure A - 6: Alternative view of the feed point

Simulations were carried out using CST Microwave Studio's time domain solver with the default Gaussian input signal and an accuracy threshold of -40dB. The background was set to NORMAL (free space with $\epsilon_r = 1$, $\mu_r = 1$). The boundary conditions were set to OPEN (ADD SPACE) to allow for accurate simulation of the far-field pattern. The mesh grid used a HEXAHEDRAL mesh with a MESHLINE RATIO LIMIT of 20. The frequency of the simulations was set to 0.3GHz to 3.0GHz. The primary field monitors were set to FARFIELD (BROADBAND) and H-FIELD (SURFACE CURRENT).

The current distribution, the far-field radiation pattern, and the scattering parameters (S11) were studied in the simulations. Figures A-7 through A-11 show some typical current distributions at several frequencies in the range 0.3GHz to 3.0GHz. The current follows the outer contours of the radiating paddle as expected but there is also considerable current in the ground structure. Before presenting the far-field pattern

results and the S11 plots, we move now to an explanation of the antenna measurement arrangement. The far-field results and S11 plots will be compared in section A.5.

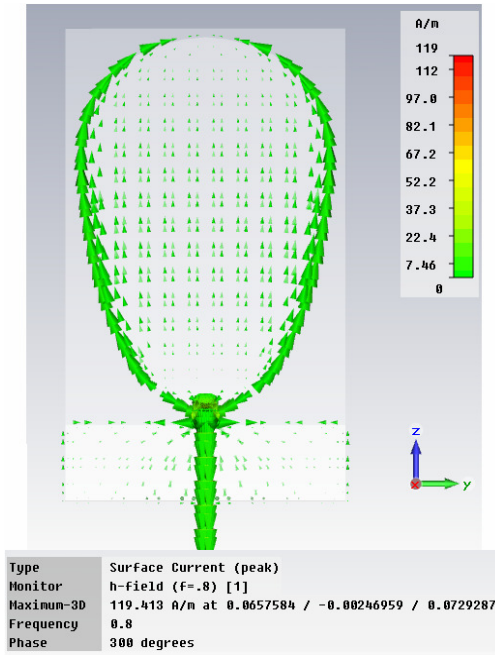


Figure A - 7: Current at 0.8 GHz

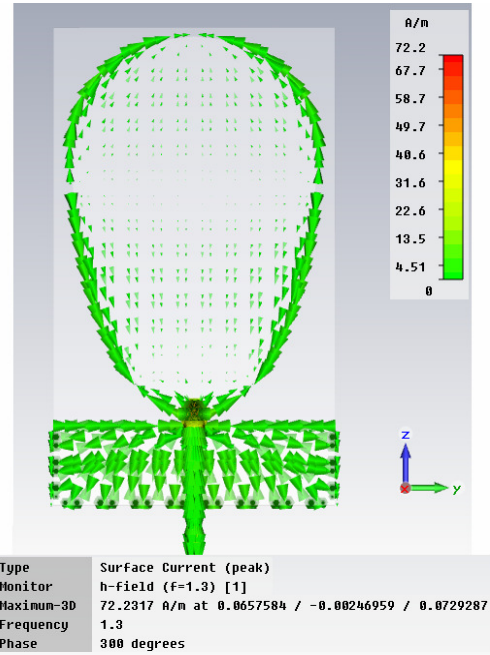


Figure A - 8: Current at 1.3 GHz

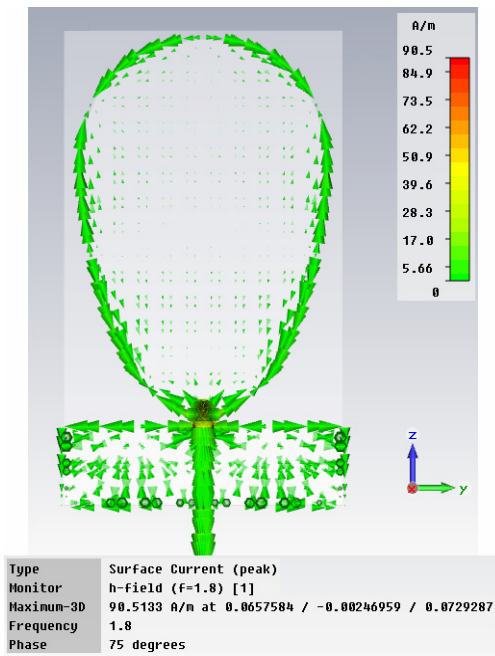


Figure A - 9: Current at 1.8 GHz

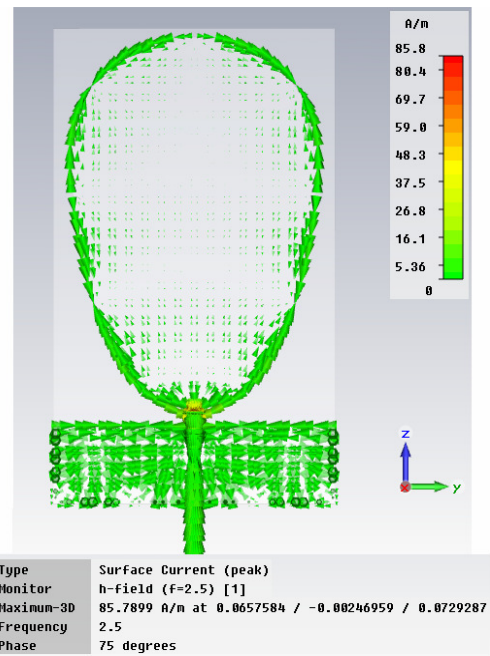


Figure A - 10: Current at 2.5 GHz

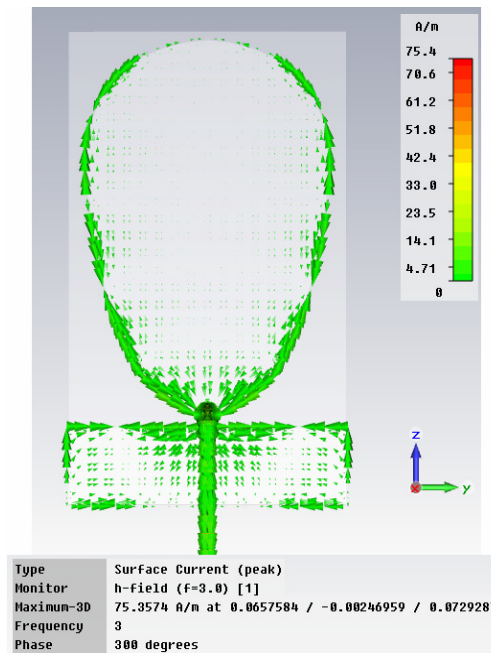


Figure A - 11: Current at 3.0 GHz

A.4 ANTENNA MEASUREMENT ARRANGEMENT

This section describes the arrangement used to measure the far-field radiation pattern and the scattering parameters (S11) of the type 2 antennas. The measurements were conducted in the Air Force Research Laboratory's RASCAL anechoic chamber for frequencies in the range 1.0GHz to 3.0GHz. Note that measurements were not taken below 1.0 GHz since they are not considered reliable in the compact RASCAL range. The results of these measurements will be presented in the following section.

To measure the far-field pattern, the antenna was attached to a moveable mounting assembly that rotated in azimuth and elevation. Figures A-12 and A-13 show some images of the arrangement.

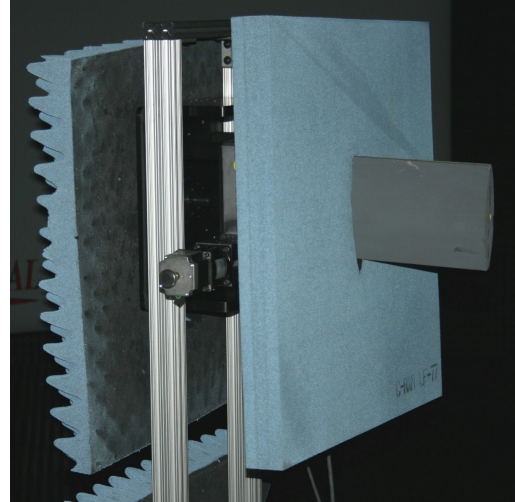
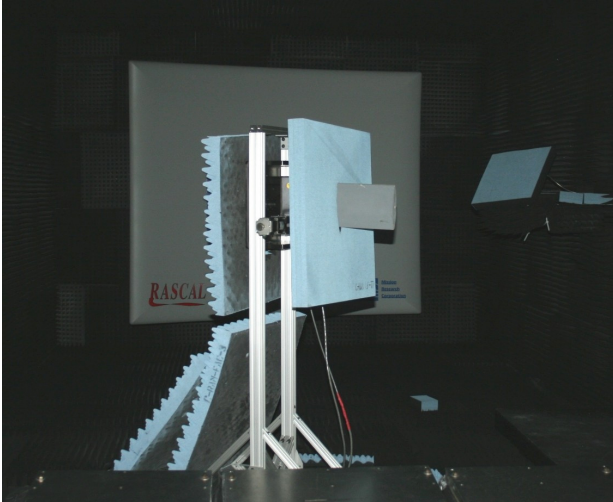


Figure A - 12: Measurement arrangement

Figure A - 13: Close-up of mount

For convenience of explanation, Figure A-14 shows a drawing of an equivalent arrangement with the antenna oriented along the Z-axis. In the equivalent arrangement, it's easiest to think of the antenna as sitting still while the transmitting source moves through angles $0^\circ \leq \theta \leq 90^\circ$ and $-180^\circ \leq \phi \leq 180^\circ$ in 5° and 1° increments, respectively. These angles provided a good upper hemispherical dome ($z > 0$) of measurements.

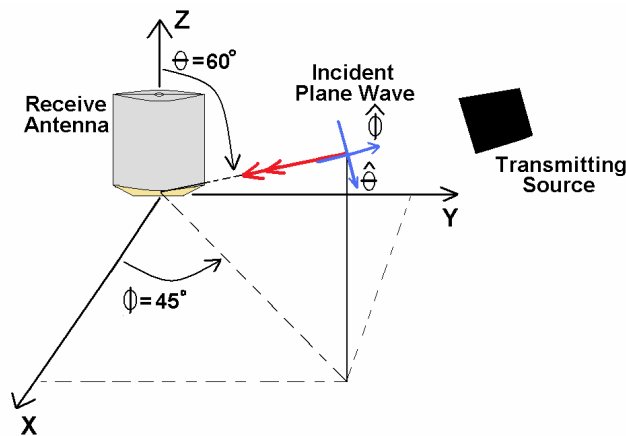


Figure A - 14: Equivalent arrangement with example incident wave at $\theta=60^\circ$, $\phi=45^\circ$

The transmitting source shown in Figure A-14 was configured to radiate vertical-only, linearly polarized waves (E_v) toward the antenna. Horizontally polarized waves (E_h) were not used due to an unfortunate miscommunication during the measurement process. Regrettably, there was not enough time to schedule another measurement session to obtain the E_h component. Nonetheless, the measured data is still very useful for two reasons. First, as we see from the current distribution presented in the previous section, the current is mostly vertically directed on the paddle structure leading us to expect that the E_v component would be much more intense than the E_h component in the far-field pattern. Indeed, CST simulations show the E_v component to be as much as 20dB higher than the E_h component. Therefore, the E_v component alone still gives us a good representation of the antenna's radiation characteristics. Second, one of the main reasons for measuring this pattern was to compare it to the CST simulation to see how accurately the CST model predicts the antenna's performance. Comparing the simulated E_v component against the measured E_v component suits this purpose well.

The reflection coefficient (S_{11}) was measured on two separate occasions. The first measurement was conducted in the absence of a ground plane. For this measurement, the antenna was mounted on a wooden rod in AFIT's microwave lab and the S_{11} was measured using an Agilent E8362B network analyzer. In the second measurement, the antenna was mounted on a simulated infinite ground plane constructed of a four foot diameter metal structure that resembles a large *donut* (no image available). The measurement was conducted in the RASCAL anechoic chamber using an HP8510C

network analyzer. In both cases, the network analyzers were calibrated at the end of the coax line to a 50Ω load. The comparisons of the reflection coefficient, as well as the far-field pattern comparisons, are presented in the next section.

A.5 COMPARISON OF S11 AND FAR-FIELD PATTERNS

Herein we compare the simulated and measured reflection coefficient S11 as well as the far-field patterns for E . Up first is the comparison of the S11 data contained in Figure A-15 which shows the measured versus the simulated S11 in the frequency range from 0.5GHz to 3.0 GHz.

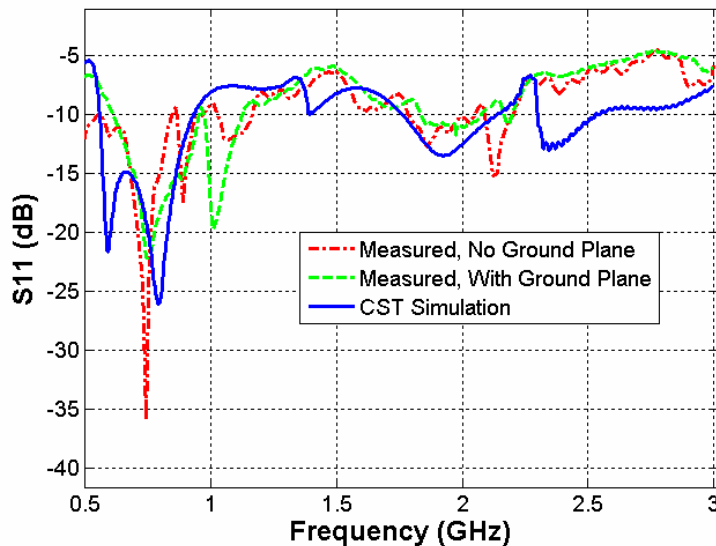


Figure A - 15: Measured vs. simulated S11

Although we would expect the simulated S11 line to match more closely with the data taken without the ground plane since no ground plane was included in the CST model, we see from Figure A-15 that the simulated line follows both sets of measured data fairly well. There are some notable disparities however. The first resonance below -15dB for

the measured data sets, for example, occurs near the second resonance of the simulated data. Also, the simulated plot above roughly 2.25GHz drops below -10dB and stays roughly 5dB below the measured data thereafter. The differences could be due to inaccuracies in the model or because the antenna was interacting with the metal structures in the rooms where the measurements were taken.

The far-field pattern comparisons are presented next. Figures A-16 through A-20 show a few 3D patterns of the relative magnitude of the measured E in the far-field at several frequencies (the simulated 3D patterns are not shown). Note that the Z-axis scale changes in some of the figures. Figure A-16 includes a drawing of the antenna orientation for reference.

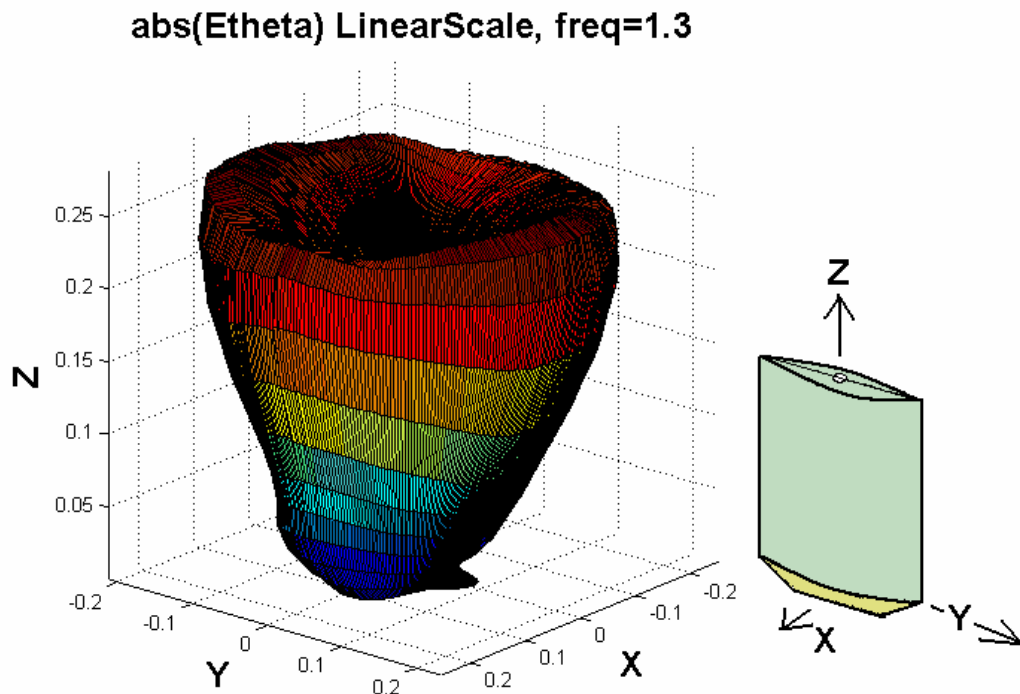


Figure A - 16: abs(E_{θ}) at 1.3GHz (with antenna drawn for reference)

abs(Etheta) LinearScale, freq=1.8

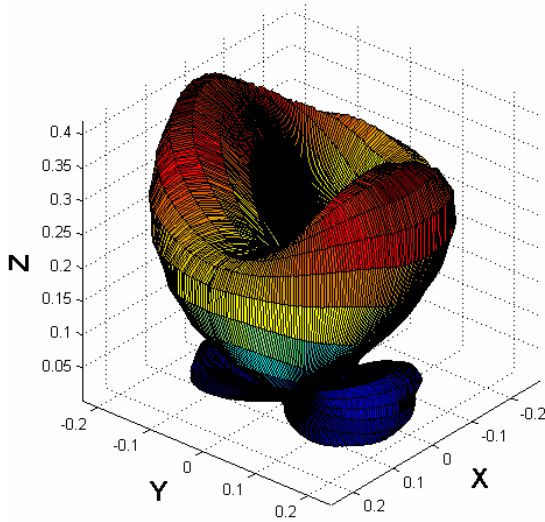


Figure A - 17: $abs(E_{\theta})$ at 1.8GHz

abs(Etheta) LinearScale, freq=2.1

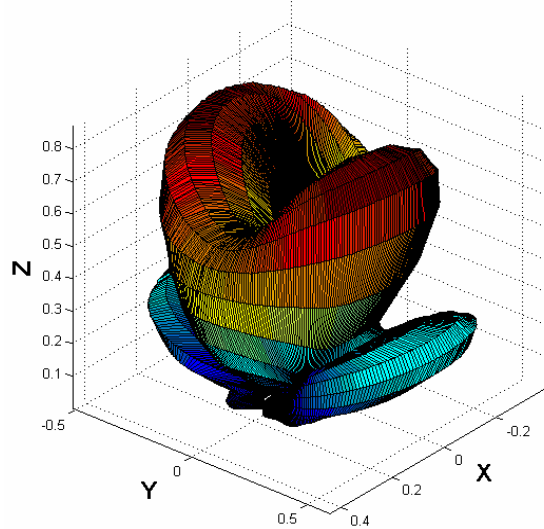


Figure A - 18: $abs(E_{\theta})$ at 2.1GHz

abs(Etheta) LinearScale, freq=2.5

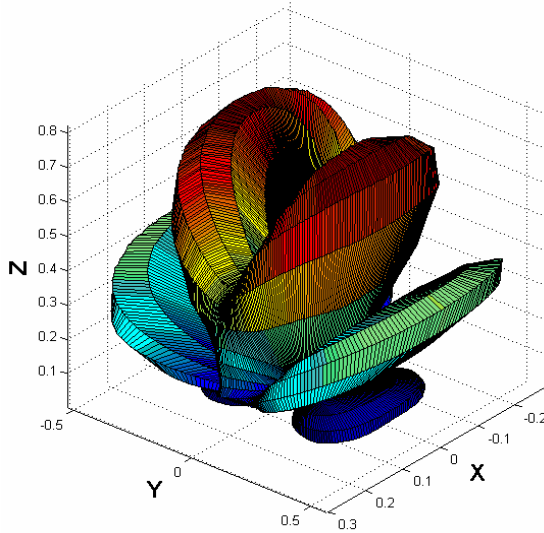


Figure A - 19: $abs(E_{\theta})$ at 2.5GHz

abs(Etheta) LinearScale, freq=3

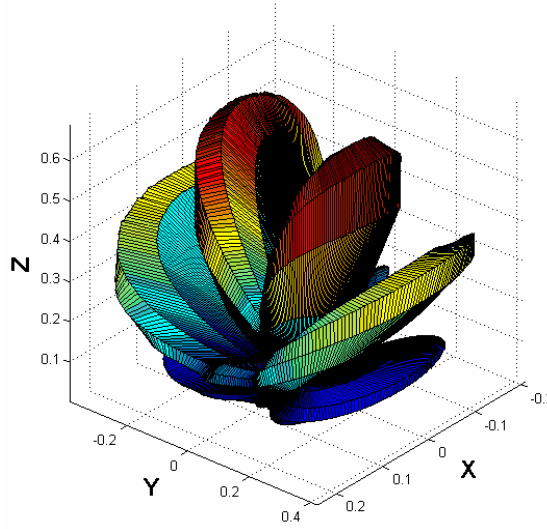


Figure A - 20: $abs(E_{\theta})$ at 3.0GHz

The 3D figures shown above, while useful for getting a feel for where the energy is radiated, are not very helpful for comparison to the simulated patterns. Therefore, Figures A-21 through A-64 on the following pages show some 2D cuts of $|E_{\theta}|$ at various frequencies. The measured and simulated plots have been normalized to their own

respective maximums. In all the plots below, the value for θ was specified and the angle ϕ was swept from -180° to 180° . It should be noted that these results assume a constant temperature ($\sim 72^\circ\text{F}$). If these high band antennas were to be used on an airframe, the temperature differences occurring during flight will likely change the antenna patterns [4; 99] enough to require some form of onboard calibration technique in any finalized system.

Frequency: 1.0GHz

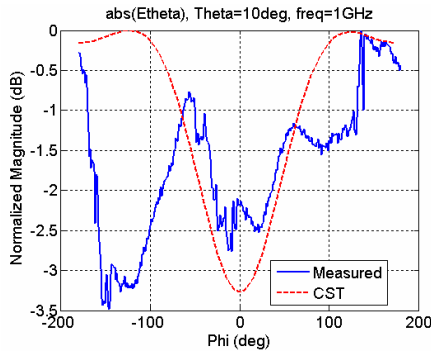


Figure A - 21: $\theta = 10^\circ$

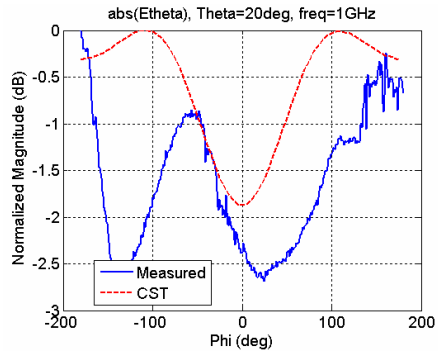


Figure A - 22: $\theta = 20^\circ$

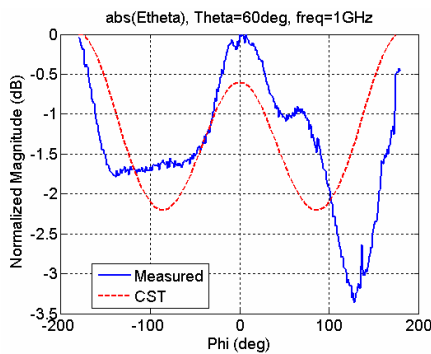


Figure A - 23: $\theta = 60^\circ$

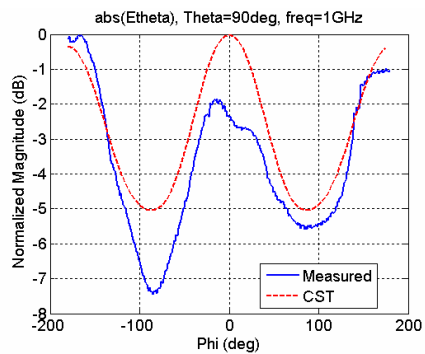
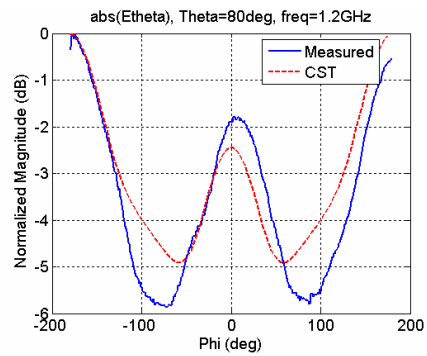
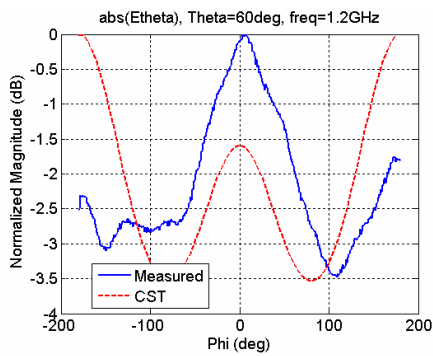
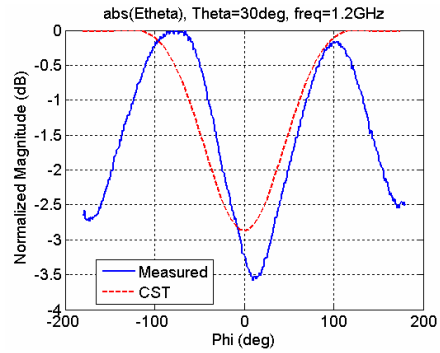
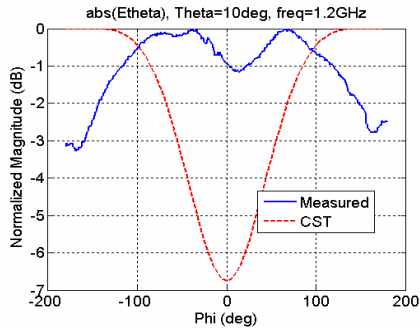
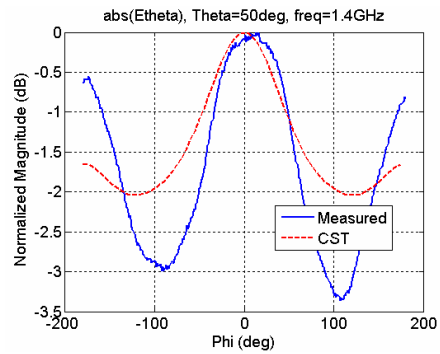
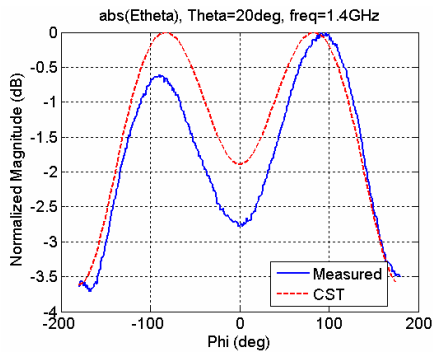


Figure A - 24: $\theta = 90^\circ$

Frequency: 1.2GHz



Frequency: 1.4GHz



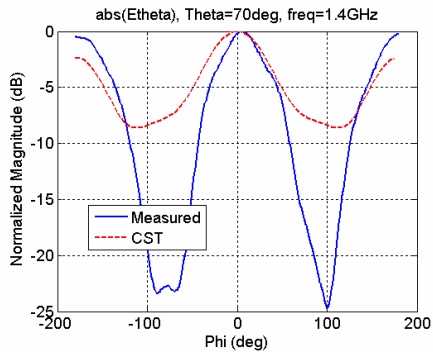


Figure A - 31: $\theta = 70^\circ$

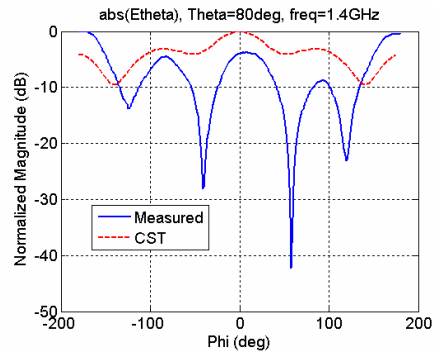


Figure A - 32: $\theta = 80^\circ$

Frequency: 1.6GHz

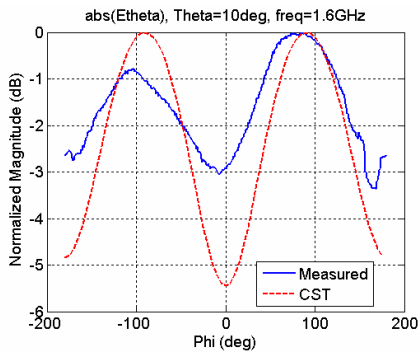


Figure A - 33: $\theta = 10^\circ$

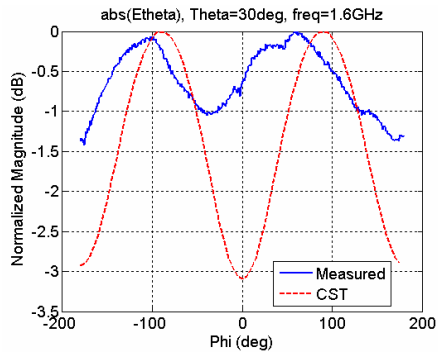


Figure A - 34: $\theta = 30^\circ$

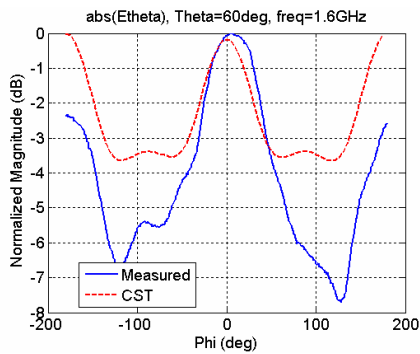


Figure A - 35: $\theta = 60^\circ$

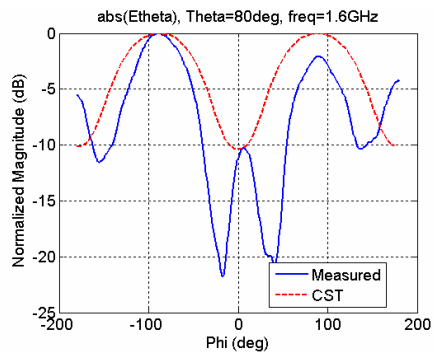


Figure A - 36: $\theta = 80^\circ$

Frequency: 1.8GHz

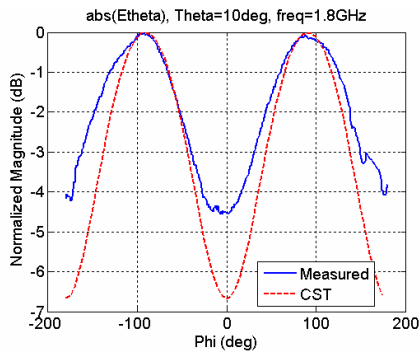


Figure A - 37: $\theta = 10^\circ$

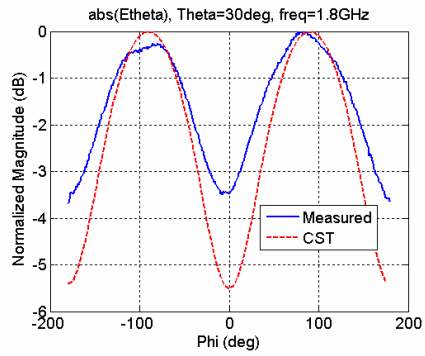


Figure A - 38: $\theta = 30^\circ$

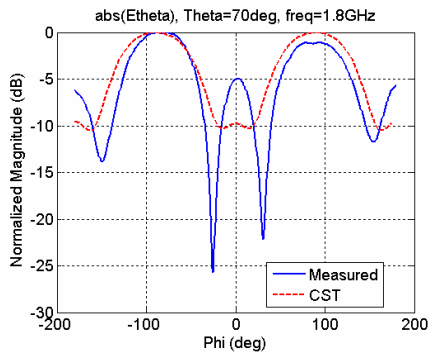


Figure A - 39: $\theta = 70^\circ$

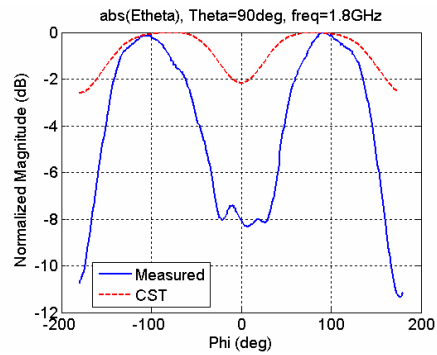


Figure A - 40: $\theta = 90^\circ$

Frequency: 2.0GHz

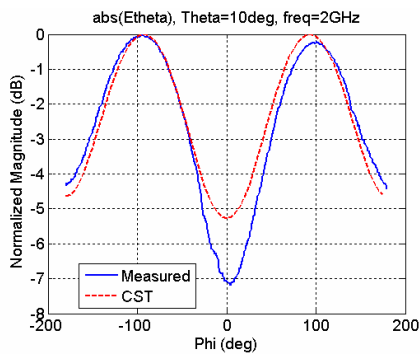


Figure A - 41: $\theta = 10^\circ$

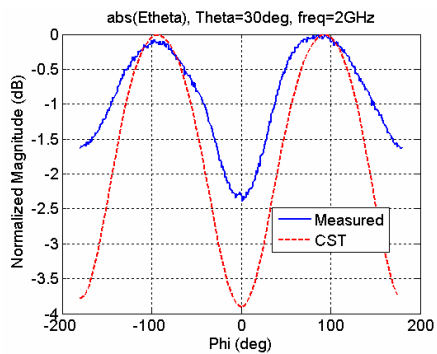


Figure A - 42: $\theta = 30^\circ$

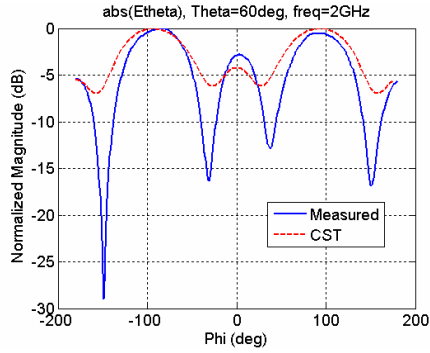


Figure A - 43: $\theta = 60^\circ$

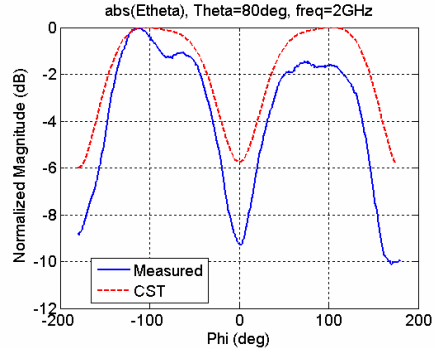


Figure A - 44: $\theta = 80^\circ$

Frequency: 2.2GHz

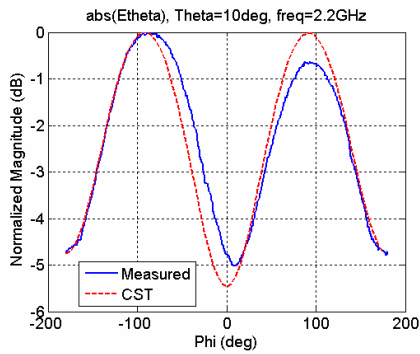


Figure A - 45: $\theta = 10^\circ$

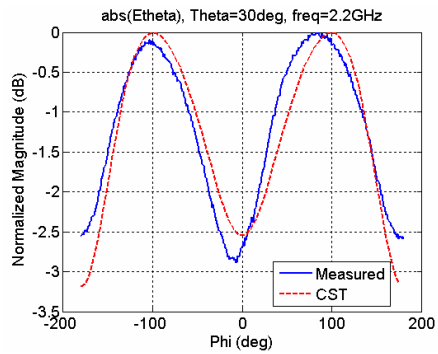


Figure A - 46: $\theta = 30^\circ$

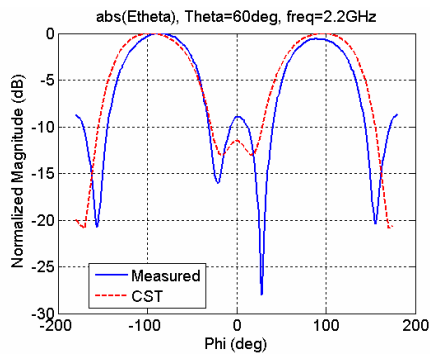


Figure A - 47: $\theta = 60^\circ$

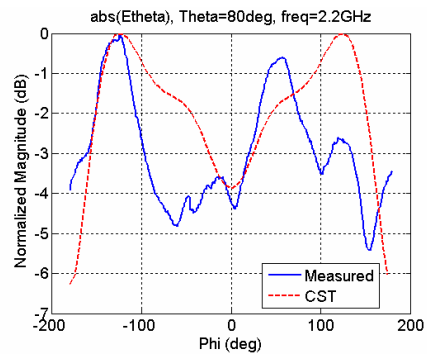


Figure A - 48: $\theta = 80^\circ$

Frequency: 2.4GHz

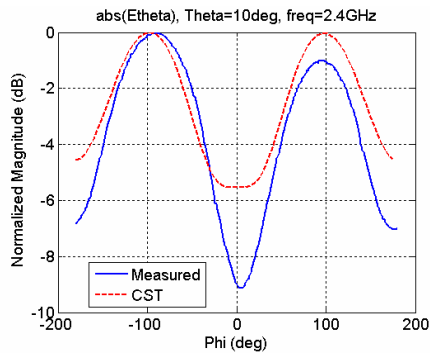


Figure A - 49: $\theta = 10^\circ$

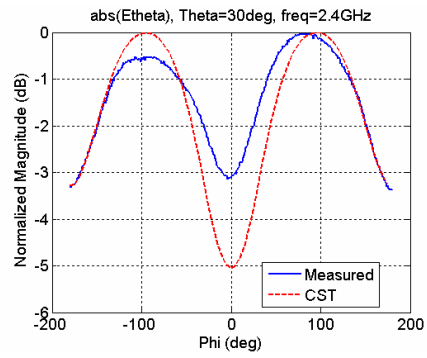


Figure A - 50: $\theta = 30^\circ$

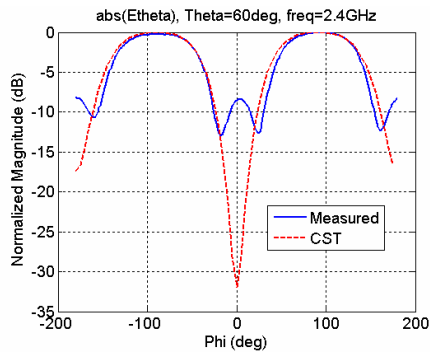


Figure A - 51: $\theta = 60^\circ$

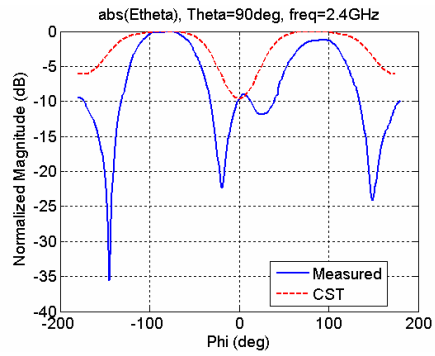


Figure A - 52: $\theta = 90^\circ$

Frequency: 2.6GHz

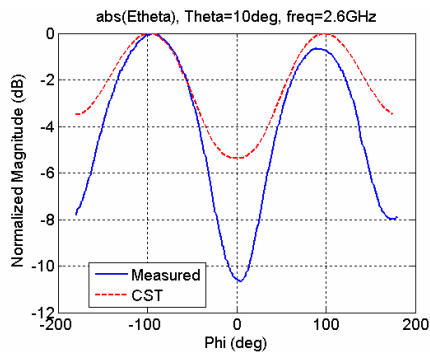


Figure A - 53: $\theta = 10^\circ$

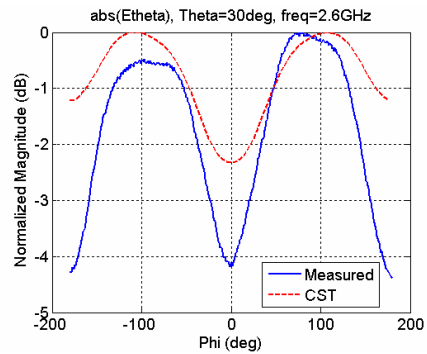


Figure A - 54: $\theta = 30^\circ$

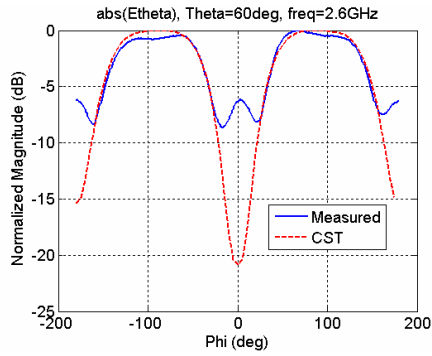


Figure A - 55: $\theta = 60^\circ$

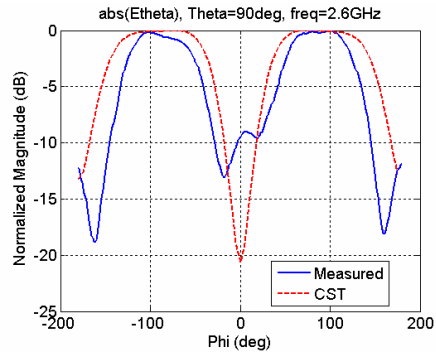


Figure A - 56: $\theta = 90^\circ$

Frequency: 2.8GHz

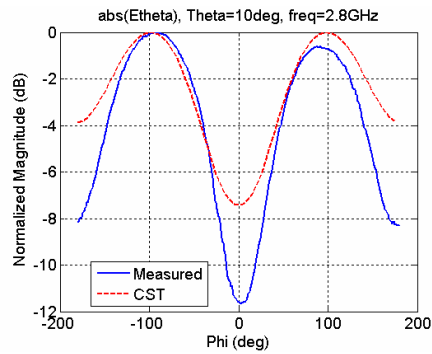


Figure A - 57: $\theta = 10^\circ$

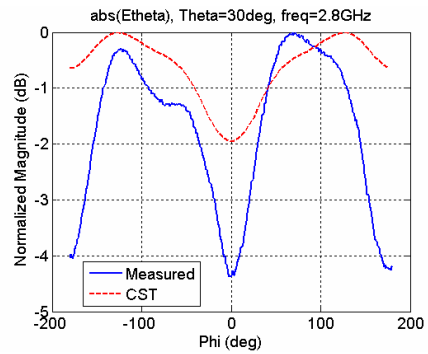


Figure A - 58: $\theta = 30^\circ$

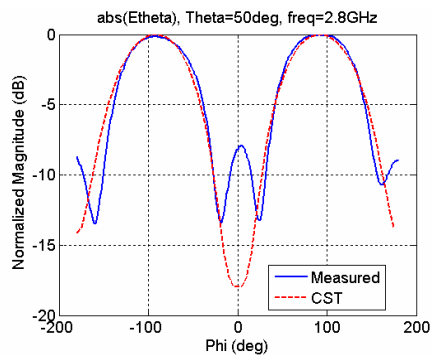


Figure A - 59: $\theta = 50^\circ$

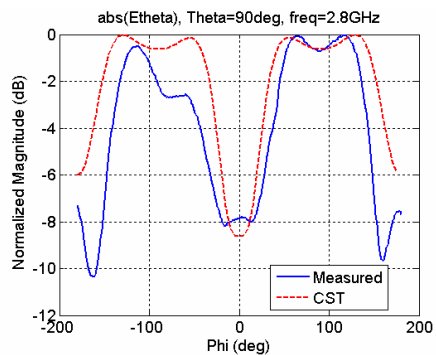


Figure A - 60: $\theta = 90^\circ$

Frequency: 3.0GHz

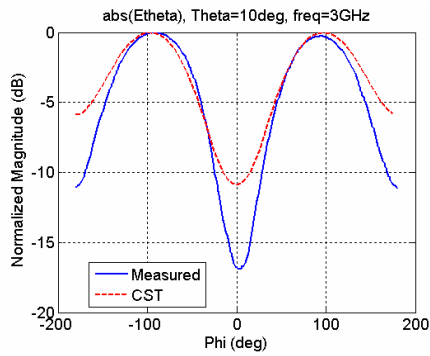


Figure A - 61: $\theta = 10^\circ$

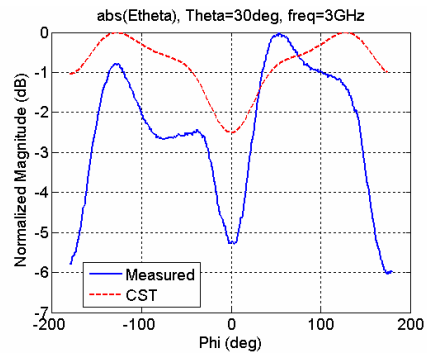


Figure A - 62: $\theta = 30^\circ$

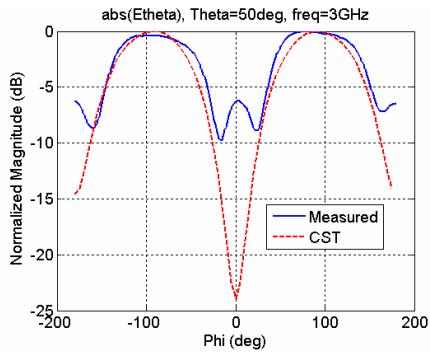


Figure A - 63: $\theta = 50^\circ$

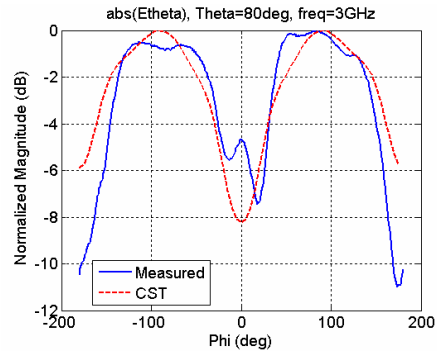


Figure A - 64: $\theta = 80^\circ$

Many of the pattern cuts shown above look quite good which suggests the CST model is fairly closely representing the behavior of the actual antenna. However, a few of the comparisons look very poor indicating that some fine tweaking of the model is needed.

A.6 CONCLUSION

This appendix has discussed the work accomplished to model, simulate, and measure the performance of the wideband antennas described in the main body of this thesis work.

The modeling and simulation was realized in CST Microwave Studio software using its time-domain solver. Measurements of the reflection coefficient (S_{11}) and the far-field E_θ

pattern were accomplished at AFRL's RASCAL anechoic chamber. The reflection coefficient showed fairly good agreement between the simulated data and the two measured data sets (with and without a ground plane). The far-field E_θ pattern showed excellent agreement between the simulated and measured data for some conical cuts at certain frequencies. However, at other frequencies the measured data differed greatly from the simulated data. Clearly, tweaking of the model could be accomplished to yield results more closely aligned with the measurements.

APPENDIX B

The Rotation Transform Matrix

A rotation transform is a general 3×3 matrix that relates the rectangular (or spherical, cylindrical, etc) vector components in one coordinate system to the rectangular vector components in another coordinate system. There are several well-known variations of the rotation transform in popular use. A more complete description of the one summarized in this appendix can be found in [36].

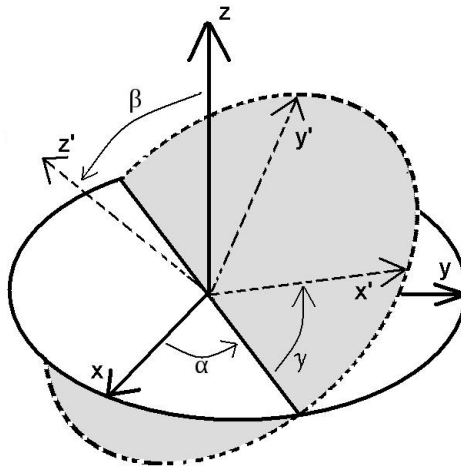


Figure B - 1: Two coordinate systems related by rotation angles α , β , and γ

Figure B-1 shows the two coordinate systems and the angles of rotation α , β , and γ . The first coordinate system is referred to as the unprimed or r -coordinate system (the r is for *rectangular*) and has axis denoted x , y , and z . The second coordinate system, referred to as the primed or r' -coordinate system, originally started out perfectly aligned with the r -

coordinate system but has now been rotated by the angles α , β , and γ as shown. The axes of the r' -coordinate system are denoted x' , y' , and z' . The origins of the two coordinate systems still coincide after the rotation has been applied.

To visualize the rotations, begin with the two coordinate systems aligned so that $x=x'$, $y=y'$, and $z=z'$. Then rotate the x' -axis counterclockwise by angle α while keeping the $z=z'$ axes fixed. Next, hold the x' -axis fixed at its new position and rotate the z' -axis counterclockwise away from the z -axis by the angle β . Finally, hold the z' -axis fixed once again and rotate the x' -axis counterclockwise (away from the xy -plane) by the angle γ . When the rotations are applied in that order, the matrix describing the complete rotation from the r -coordinate system to the r' -coordinate system is

$${}^{r'}\mathbf{A}^r = \begin{bmatrix} \cos(\alpha) & \sin(\alpha) & 0 \\ -\sin(\alpha) & \cos(\alpha) & 0 \\ 0 & 0 & 1 \end{bmatrix} \begin{bmatrix} 1 & 0 & 0 \\ 0 & \cos(\beta) & \sin(\beta) \\ 0 & -\sin(\beta) & \cos(\beta) \end{bmatrix} \begin{bmatrix} \cos(\gamma) & \sin(\gamma) & 0 \\ -\sin(\gamma) & \cos(\gamma) & 0 \\ 0 & 0 & 1 \end{bmatrix} \quad (\text{B-1})$$

The choice of notation in ${}^{r'}\mathbf{A}^r$ is handy since, as demonstrated in the examples below, the right superscript will be *touching* a vector in the r -coordinate system while the left superscript is *touching* the vector representation in the r' -coordinate system. To rotate back to the r -coordinate system from the r' -coordinate system, we simply take the inverse as

$${}^r\mathbf{A}^{r'} = \left({}^{r'}\mathbf{A}^r \right)^{-1} \quad (\text{B-2})$$

Often, the rotation transform matrix is applied in conjunction with rectangular-to-spherical or spherical-to-rectangular transformations. A review of the rectangular-to-spherical transformations can be found in [6] and are repeated here for convenience.

Rectangular-to-spherical transform:

$${}^s \mathbf{T}^r = \begin{bmatrix} \sin(\alpha) \cos(\beta) & \sin(\alpha) \sin(\beta) & \cos(\alpha) \\ \cos(\alpha) \cos(\beta) & \cos(\alpha) \sin(\beta) & -\sin(\alpha) \\ -\sin(\alpha) & \cos(\alpha) & 0 \end{bmatrix} \quad (\text{B-3})$$

Spherical-to-rectangular transform:

$${}^r \mathbf{T}^s = \left({}^s \mathbf{T}^r \right)^{-1} = \begin{bmatrix} \sin(\alpha) \cos(\beta) & \cos(\alpha) \cos(\beta) & -\sin(\alpha) \\ \sin(\alpha) \sin(\beta) & \cos(\alpha) \sin(\beta) & \cos(\alpha) \\ \cos(\alpha) & \cos(\alpha) & 0 \end{bmatrix} \quad (\text{B-4})$$

The following examples will illustrate the usefulness of these transforms. The first two examples demonstrate how the rotation transform can be used to obtain the far-field radiation pattern of a short dipole along the y-axis by using the known radiation pattern of an identical short dipole that has been oriented along the z-axis. The third example applies the rotation transform to a bowtie antenna and explains how to find the rotated 3-dimensional pattern from a known pattern that has only been computed at discrete points.

Example 1: Suppose we have a short (Hertzian) dipole placed along the z-axis as shown in Figure B-2(a) where the r' -coordinate system is perfectly aligned with the r -coordinate system. If we rotate the r' -coordinate system by angles $\alpha = 90^\circ$, $\beta = 90^\circ$, and $\gamma = 0^\circ$, we have the situation shown in Figure B-2(b). The far-field radiation pattern is the same in

both figures since the dipole's physical radiation characteristics have not changed. Now, however, it appears as though we have a short dipole placed along the y' -axis thereby giving us the radiation pattern of a y' -directed dipole.

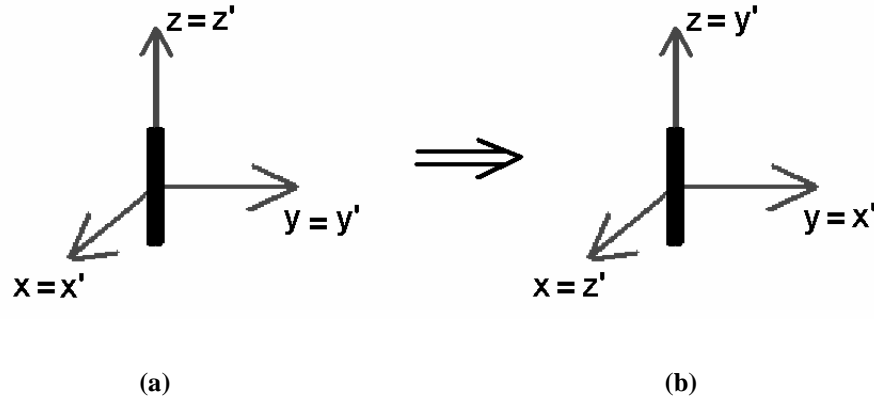


Figure B - 2: Intuitive rotation for a dipole along the Z-axis

This example, while intuitive, has resulted in the desired far-field pattern being expressed in the r' -coordinate system. The following example, although it may appear backwards at first, illustrates how to ensure that the final solution is in the r -coordinate system as desired.

Example 2: From antenna theory, the expressions for the far-field radiation patterns of short dipoles along the z' -axis and y -axis are known to be [6]

$$\text{Short dipole along } z'\text{-axis: } \vec{E}_{z'} \approx \hat{z}' \sin(\theta) \quad (\text{B-5})$$

$$\text{Short dipole along } y\text{-axis: } \vec{E}_y \approx -\hat{y} \cos(\theta) \sin(\phi) - \hat{z} \cos(\theta) \cos(\phi) \quad (\text{B-6})$$

In this example, we want to apply the rotation transform to $\vec{E}_{z'}$ in order to obtain \vec{E}_y in the unprimed coordinate system.

Starting in the r' -coordinate system, we place the z -directed dipole with the known radiation pattern along the z' -axis as shown in Figure B-3(a). We then place the y -directed dipole with the desired (assumed unknown) radiation pattern in the r -coordinate system as shown in Figure B-3(b).

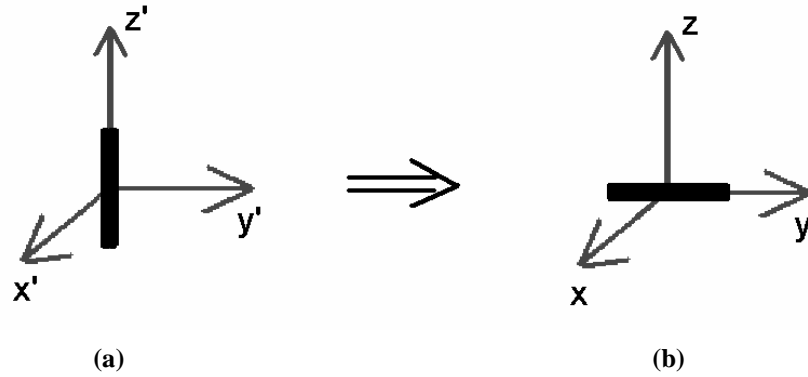


Figure B - 3: Rotation that produces a solution in the unprimed coordinate system

Referencing Figure B-3(b), if we rotate the r -coordinate system by angles $\alpha = 180^\circ$, $\beta = 90^\circ$, and $\gamma = 0^\circ$, we would arrive at the orientation in Figure B-3(a) where the z' -axis is directed along the antenna. Therefore, based on equation B-1, the rotation matrix from the r -coordinate system to the r' -coordinate system is given by

$${}^{r'}\mathbf{A}^r = \begin{bmatrix} -1 & 0 & 0 \\ 0 & 0 & 1 \\ 0 & 1 & 0 \end{bmatrix} \quad (\text{B-7})$$

The rotation from the r' -coordinate system to the r -coordinate system is

$${}^r\mathbf{A}^{r'} = ({}^{r'}\mathbf{A}^r)^{-1} = \begin{bmatrix} -1 & 0 & 0 \\ 0 & 0 & 1 \\ 0 & 1 & 0 \end{bmatrix} \quad (\text{B-8})$$

To express the far-field pattern of the y -directed antenna in the r -coordinate system, we need to relate the spherical angles (θ', ϕ') to (θ, ϕ) . In general, any unit vector in the r -coordinate system can be written as $\hat{u} = u_x \hat{x} + u_y \hat{y} + u_z \hat{z}$ where the components are given by

$$u_x = \sin(\theta) \cos(\phi) \quad (\text{B-9})$$

$$u_y = \sin(\theta) \sin(\phi) \quad (\text{B-10})$$

$$u_z = \cos(\theta) \quad (\text{B-11})$$

Converting \hat{u} to the r' -coordinate system we have

$$\hat{u}' = \begin{bmatrix} u_{x'} \\ u_{y'} \\ u_{z'} \end{bmatrix} = {}^{r'}\mathbf{A}^r \begin{bmatrix} u_x \\ u_y \\ u_z \end{bmatrix} = \begin{bmatrix} -1 & 0 & 0 \\ 0 & 0 & 1 \\ 0 & 1 & 0 \end{bmatrix} \begin{bmatrix} \sin(\theta) \cos(\phi) \\ \sin(\theta) \sin(\phi) \\ \cos(\theta) \end{bmatrix} = \begin{bmatrix} -\sin(\theta) \cos(\phi) \\ \cos(\theta) \\ \sin(\theta) \sin(\phi) \end{bmatrix} \quad (\text{B-12})$$

The spherical angles in the r' -coordinate system are

$$\theta' = \cos^{-1}(u_{z'}) = \cos^{-1}(\cos(\theta) \sin(\phi)) \quad (\text{B-13})$$

$$\phi' = \tan^{-1}\left(\frac{u_{y'}}{u_{x'}}\right) = \tan^{-1}\left(\frac{\cos(\theta)}{-\sin(\theta) \cos(\phi)}\right) \quad (\text{B-14})$$

which are completely specified by the desired angles (θ, ϕ) in the r -coordinate system.

Putting it all together, the desired radiation pattern of the y -directed dipole in the unprimed spherical coordinate system is

$$\begin{bmatrix} E_r \\ E_\theta \\ E_\phi \end{bmatrix} = {}^s\mathbf{T}^{r'} {}^r\mathbf{A}^{r'} {}^{r'}\mathbf{T}^{s'} \begin{bmatrix} E_{r'} \\ E_{\theta'} \\ E_{\phi'} \end{bmatrix} = {}^s\mathbf{T}^{r'} {}^r\mathbf{A}^{r'} {}^{r'}\mathbf{T}^{s'} \begin{bmatrix} 0 \\ \sin(\theta') \\ 0 \end{bmatrix} \quad (\text{B-15})$$

Figures B-4 through B-7 compare a few conical cuts of the radiation pattern of the y-directed dipole using equation B-6 (from theory) and B-15 (from the rotation). From these figures, we see that the rotation matrix gives the same far-field pattern as predicted by the general antenna theory.

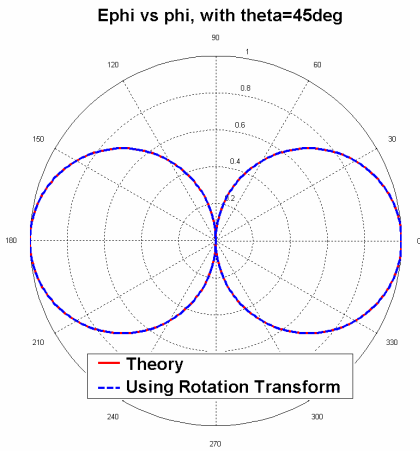


Figure B - 4: Y-directed dipole pattern
 E_ϕ vs ϕ , with $\theta=45^\circ$

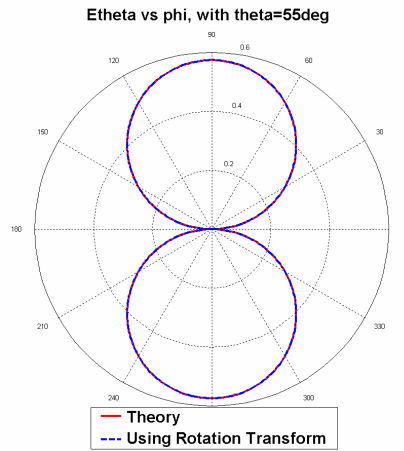


Figure B - 5: Y-directed dipole pattern
 E_θ vs ϕ , with $\theta=55^\circ$

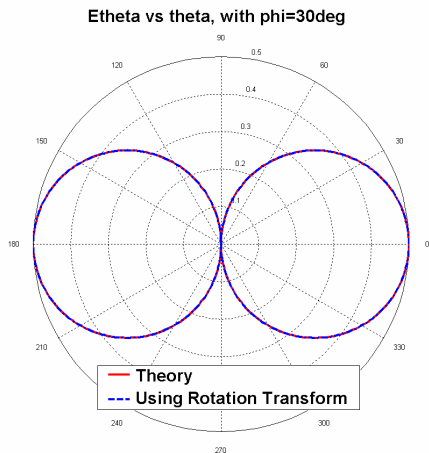


Figure B - 6: Y-directed dipole pattern
 E_θ vs θ , with $\phi=30^\circ$

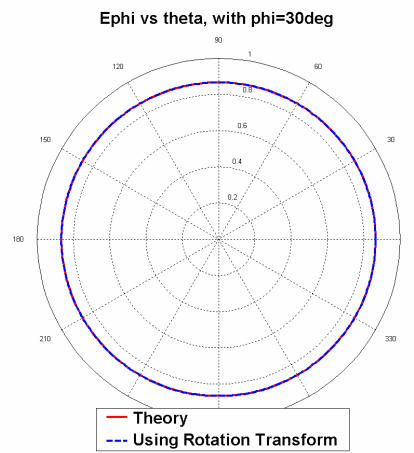


Figure B - 7: Y-directed dipole pattern
 E_ϕ vs θ , with $\phi=30^\circ$

Example 3: In the previous examples, the known far-field radiation pattern was available in a closed-form expression that allowed us to directly map the far-field pattern from one coordinate system to another. When the far-field pattern is only known for discrete combinations of the angles θ and ϕ , as computed in CST Microwave Studio for example, we can use interpolation to map the desired field points from one coordinate system to the other. For this thesis, the interpolation was implemented in Matlab using the *interp2* function. Some results, as applied to a simple bowtie antenna, are shown in the following figures.

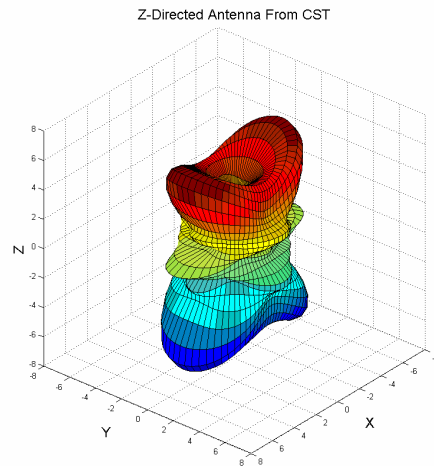


Figure B - 8: Z-directed bowtie pattern computed in CST

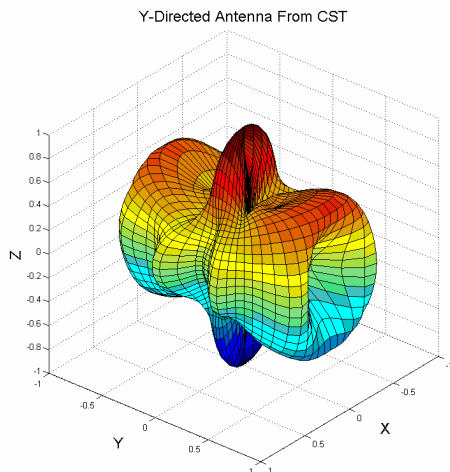


Figure B - 9: Y-directed bowtie pattern computed in CST

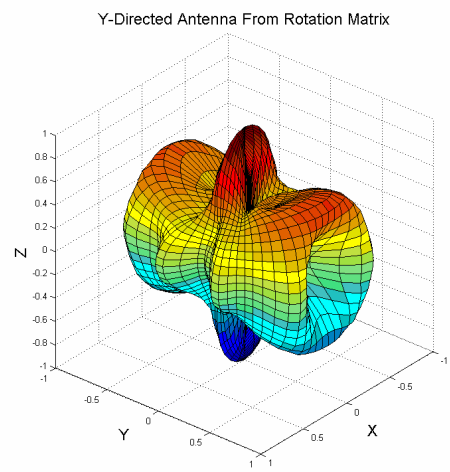


Figure B - 10: Y-directed bowtie pattern obtained by applying the rotation transform

Figure B-8 shows the simulated far-field pattern (magnitude only) of a bowtie antenna when it is placed along the z -axis in CST Microwave Studio. The pattern was computed at discrete points (θ, ϕ) in the range $\theta = 0^\circ, 5^\circ, \dots, 175^\circ, 180^\circ$ and $\phi = 0^\circ, 5^\circ, \dots, 350^\circ, 355^\circ$. Figure B-9 shows the far-field pattern of the exact same antenna when it has been oriented along the y -axis and simulated in CST Microwave Studio. Figure B-10 shows the far-field pattern as a result of applying the rotation transform to the pattern in Figure B-8. A point-by-point numerical comparison of the difference between the far-field patterns depicted in Figures B-9 and B-10 shows them to have a maximum difference of less than 1%.

In this thesis, the rotation transform was used to rotate the far-field radiation pattern of an antenna to any arbitrary orientation. This is particularly convenient for our application since it allows us to obtain the far-fields of all three antennas by solving for only one of them via simulation in CST Microwave Studio.

APPENDIX C

Maximum Likelihood and MUSIC Algorithm Results

This appendix contains a listing of the results of the maximum likelihood and MUSIC algorithms when applied to the biconical antennas as described in Chapters 3 and 4. The maximum likelihood results are presented with and without mutual coupling effects for both the 205mm antennas and the 50mm antennas for different angular spacings of α (1° , 10° , 20° , 30° , 40° , and 50°). To compute the results without mutual coupling effects in CST Microwave Studio, uniform plane waves were radiated toward each antenna while the other two antennas were removed from the simulation. To include mutual coupling effects, all three antennas were included in the simulation at the same time. No noise was added to the maximum likelihood simulations. In the images contained below, the blue areas represent relatively small g -values and the red areas are relatively large g -values. The red circle is the known location of the emitter and the green plus sign is the estimated location. Starting on page C-12, the MUSIC algorithm results are presented for the case of the 50mm biconical antennas with mutual coupling effects included and an $SNR = 35\text{dB}$. For all simulations, the incident signal had arrival angles ($\theta = 50^\circ$, $\phi = 210^\circ$).

Maximum Likelihood Results 205mm Antennas

0.5GHz, no mutual coupling

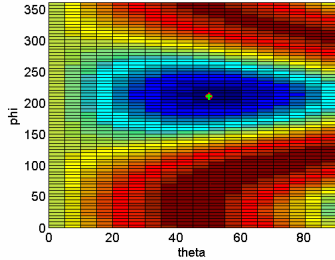


Figure C - 1: $\alpha = 1^\circ$

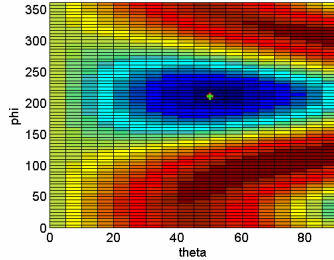


Figure C - 2: $\alpha = 10^\circ$

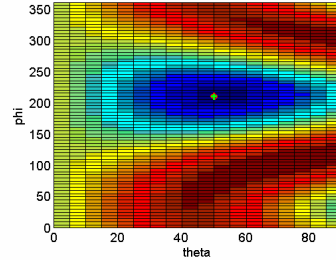


Figure C - 3: $\alpha = 20^\circ$

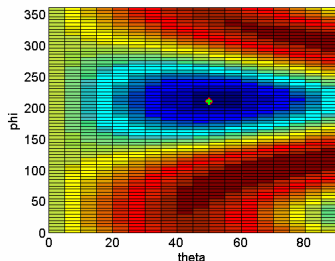


Figure C - 4: $\alpha = 30^\circ$

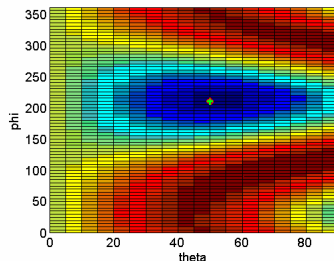


Figure C - 5: $\alpha = 40^\circ$

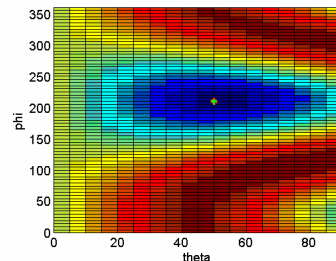


Figure C - 6: $\alpha = 50^\circ$

0.5GHz, with MUTUAL COUPLING

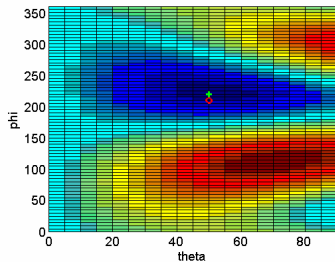


Figure C - 7: $\alpha = 1^\circ$

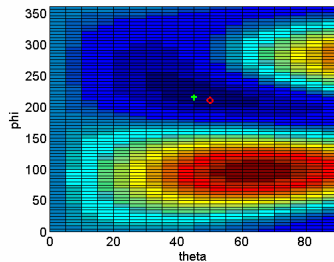


Figure C - 8: $\alpha = 10^\circ$

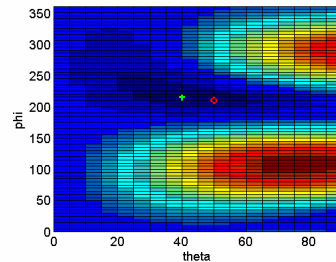


Figure C - 9: $\alpha = 20^\circ$

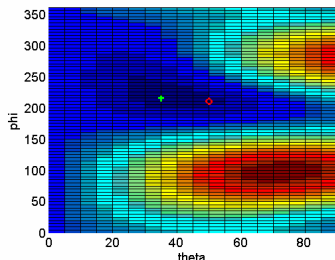


Figure C - 10: $\alpha = 30^\circ$

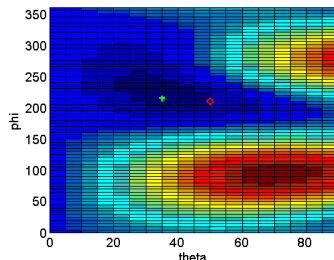


Figure C - 11: $\alpha = 40^\circ$

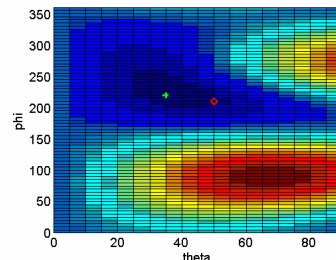


Figure C - 12: $\alpha = 50^\circ$

Maximum Likelihood Results 205mm Antennas

1GHz, no mutual coupling

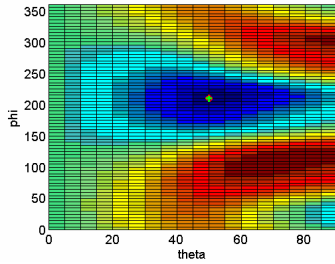


Figure C - 13: $\alpha = 1^\circ$

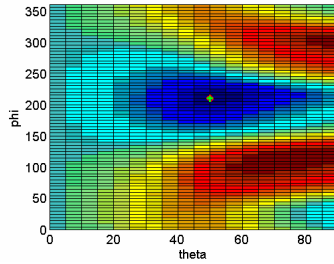


Figure C - 14: $\alpha = 10^\circ$

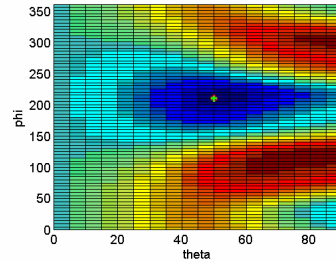


Figure C - 15: $\alpha = 20^\circ$

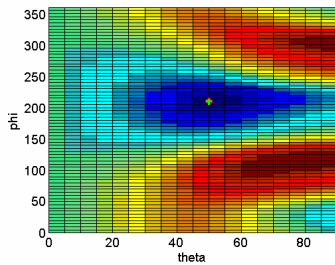


Figure C - 16: $\alpha = 30^\circ$

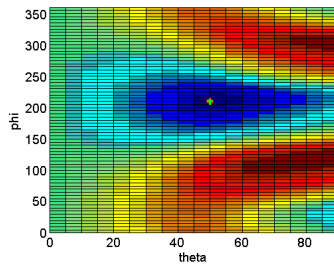


Figure C - 17: $\alpha = 40^\circ$

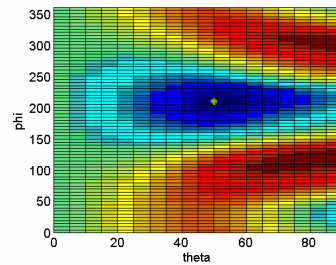


Figure C - 18: $\alpha = 50^\circ$

1GHz, with MUTUAL COUPLING

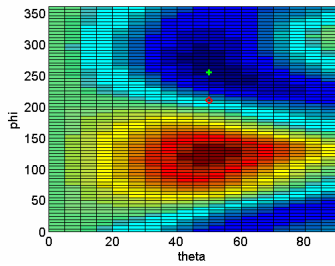


Figure C - 19: $\alpha = 1^\circ$

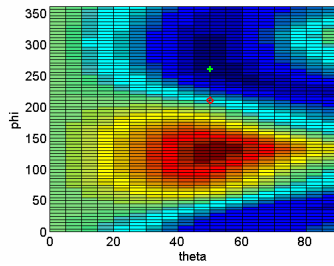


Figure C - 20: $\alpha = 10^\circ$

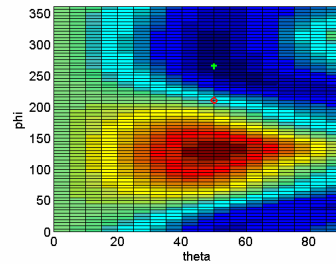


Figure C - 21: $\alpha = 20^\circ$

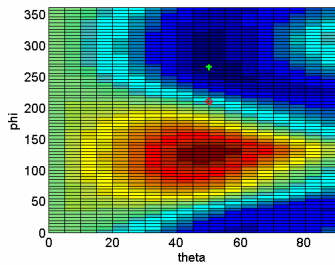


Figure C - 22: $\alpha = 30^\circ$

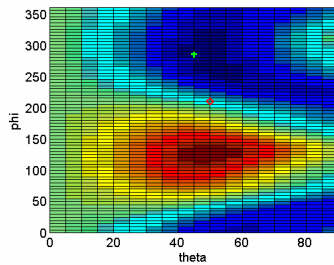


Figure C - 23: $\alpha = 40^\circ$

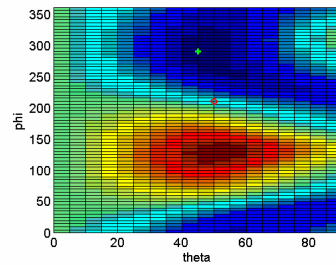


Figure C - 24: $\alpha = 50^\circ$

Maximum Likelihood Results 205mm Antennas

1.5GHz, no mutual coupling

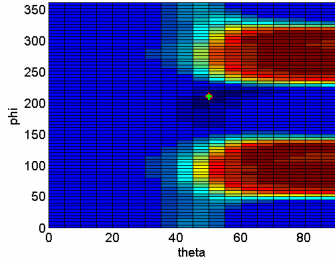


Figure C - 25: $\alpha = 1^\circ$

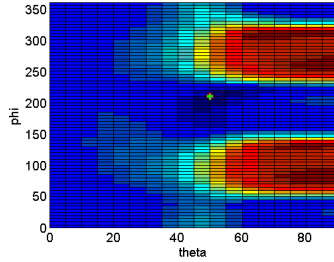


Figure C - 26: $\alpha = 10^\circ$

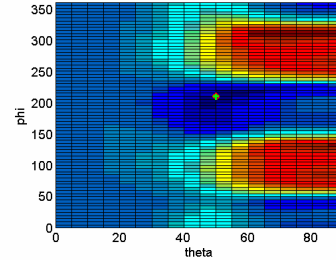


Figure C - 27: $\alpha = 20^\circ$

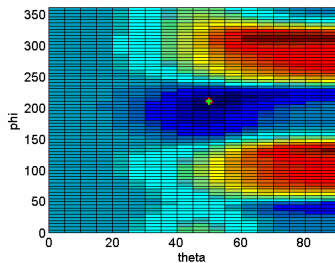


Figure C - 28: $\alpha = 30^\circ$

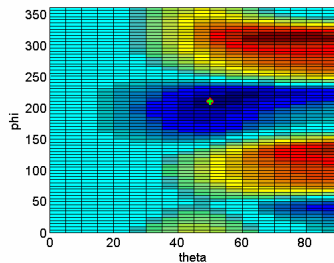


Figure C - 29: $\alpha = 40^\circ$

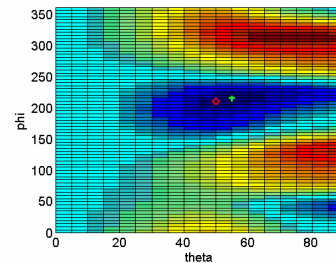


Figure C - 30: $\alpha = 50^\circ$

1.5GHz, with MUTUAL COUPLING

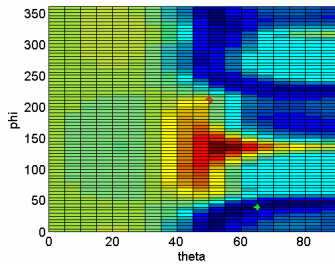


Figure C - 31: $\alpha = 1^\circ$

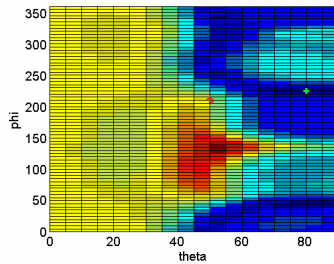


Figure C - 32: $\alpha = 10^\circ$

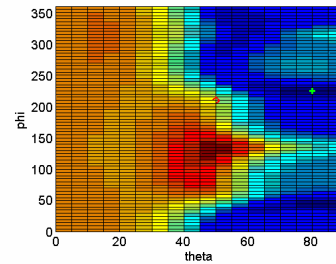


Figure C - 33: $\alpha = 20^\circ$

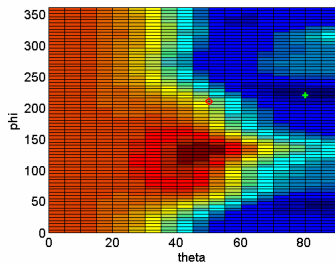


Figure C - 34: $\alpha = 30^\circ$

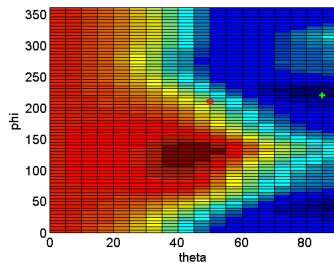


Figure C - 35: $\alpha = 40^\circ$

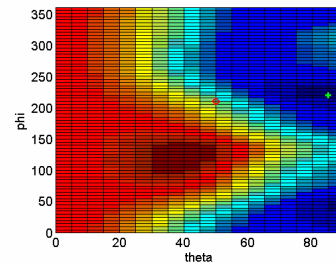


Figure C - 36: $\alpha = 50^\circ$

Maximum Likelihood Results 205mm Antennas

2GHz, no mutual coupling

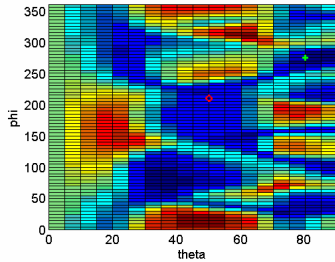


Figure C - 37: $\alpha = 1^\circ$

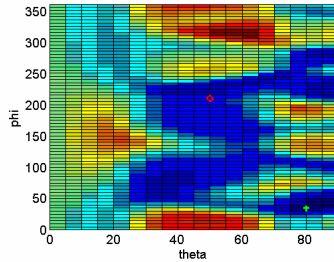


Figure C - 38: $\alpha = 10^\circ$

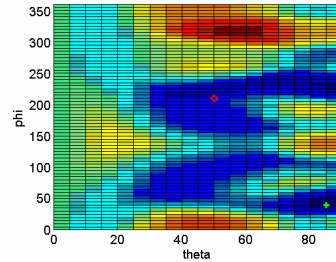


Figure C - 39: $\alpha = 20^\circ$

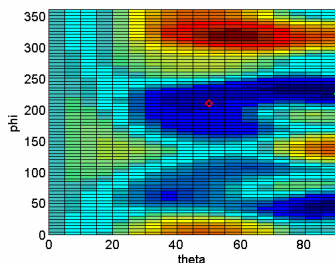


Figure C - 40: $\alpha = 30^\circ$

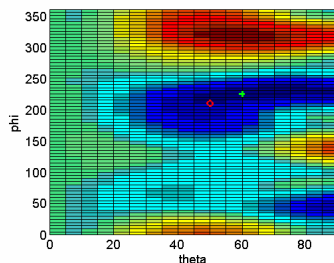


Figure C - 41: $\alpha = 40^\circ$

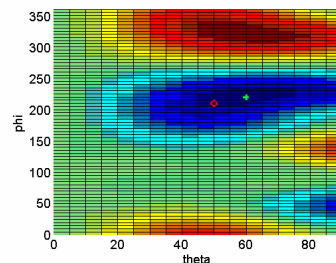


Figure C - 42: $\alpha = 50^\circ$

2GHz, with MUTUAL COUPLING

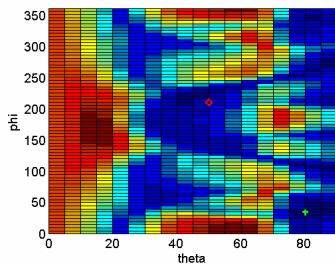


Figure C - 43: $\alpha = 1^\circ$

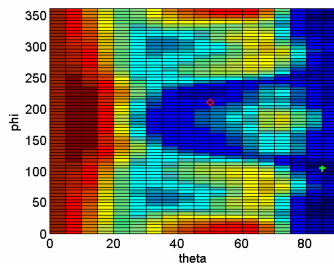


Figure C - 44: $\alpha = 10^\circ$

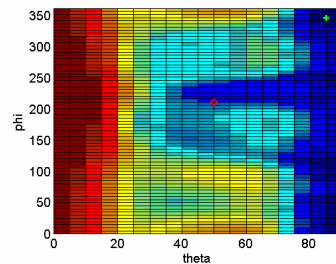


Figure C - 45: $\alpha = 20^\circ$

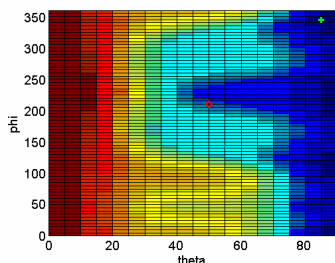


Figure C - 46: $\alpha = 30^\circ$

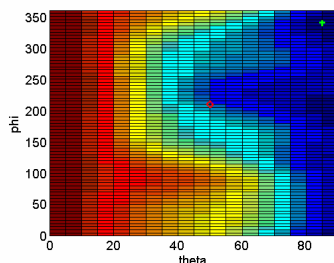


Figure C - 47: $\alpha = 40^\circ$

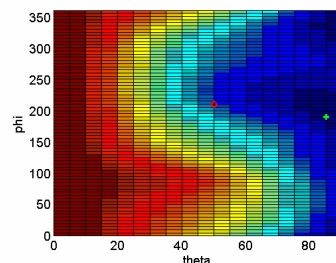


Figure C - 48: $\alpha = 50^\circ$

Maximum Likelihood Results 205mm Antennas

2.5GHz, no mutual coupling

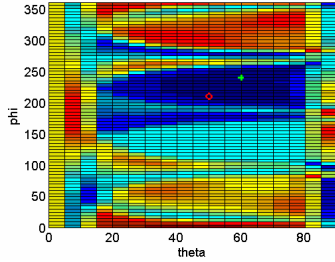


Figure C - 49: $\alpha = 1^\circ$

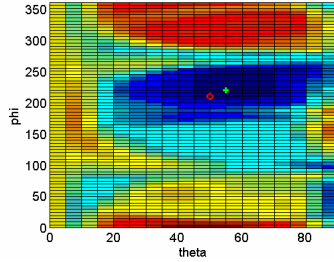


Figure C - 50: $\alpha = 10^\circ$

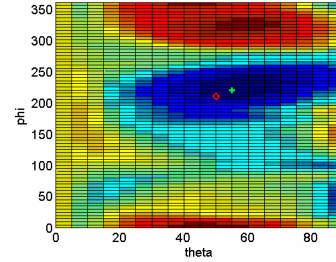


Figure C - 51: $\alpha = 20^\circ$

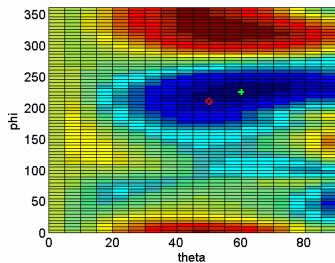


Figure C - 52: $\alpha = 30^\circ$

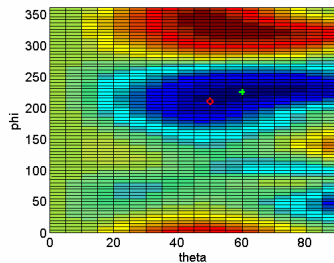


Figure C - 53: $\alpha = 40^\circ$

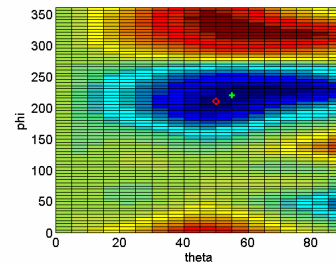


Figure C - 54: $\alpha = 50^\circ$

2.5GHz, with MUTUAL COUPLING

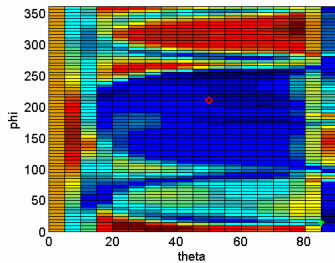


Figure C - 55: $\alpha = 1^\circ$

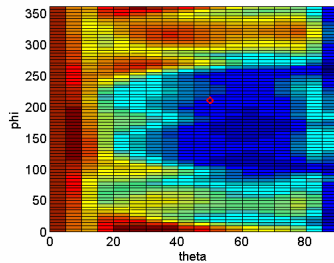


Figure C - 56: $\alpha = 10^\circ$

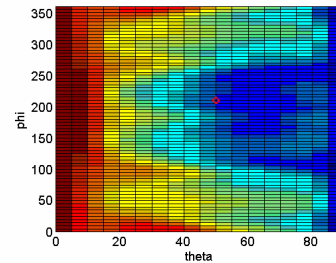


Figure C - 57: $\alpha = 20^\circ$

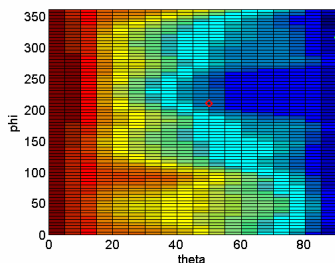


Figure C - 58: $\alpha = 30^\circ$

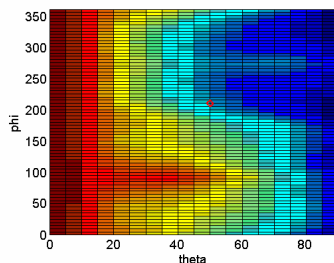


Figure C - 59: $\alpha = 40^\circ$

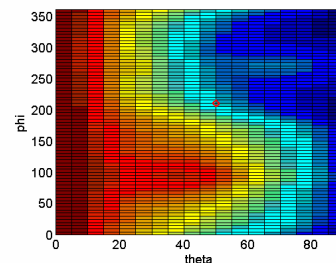


Figure C - 60: $\alpha = 50^\circ$

Maximum Likelihood Results 50mm Antennas

When there is no mutual coupling included in the simulation, the 50mm antennas produce g -value plots that are nearly identical over the entire frequency range of 0.5GHz to 3GHz for each value of α . To save space, only the results at 3GHz are shown. The remainder of the plots are for the case when mutual coupling is included.

3GHz, no mutual coupling

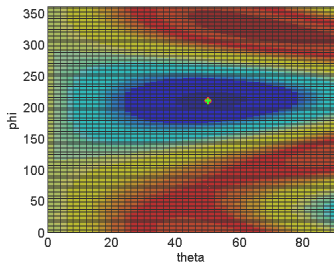


Figure C - 73: $\alpha = 1^\circ$

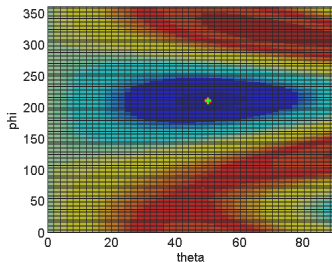


Figure C - 74: $\alpha = 10^\circ$

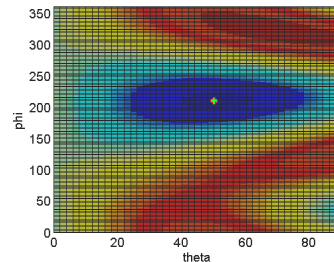


Figure C - 75: $\alpha = 20^\circ$

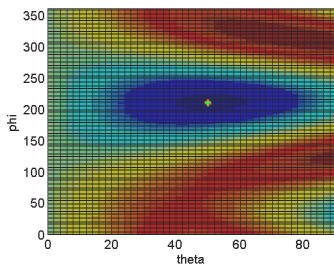


Figure C - 76: $\alpha = 30^\circ$

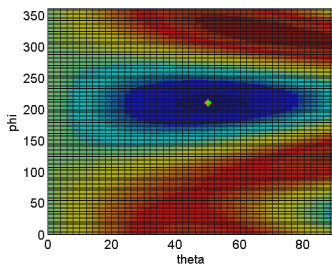


Figure C - 77: $\alpha = 40^\circ$

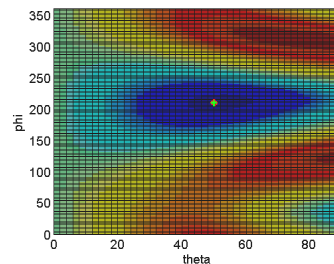


Figure C - 78: $\alpha = 50^\circ$

Maximum Likelihood Results 50mm Antennas

0.5GHz, with MUTUAL COUPLING

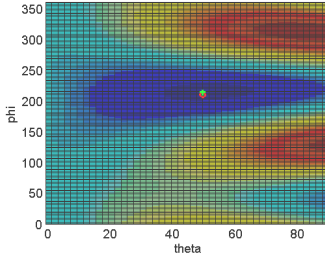


Figure C - 79: $\alpha = 1^\circ$

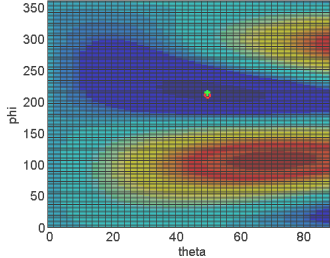


Figure C - 80: $\alpha = 10^\circ$

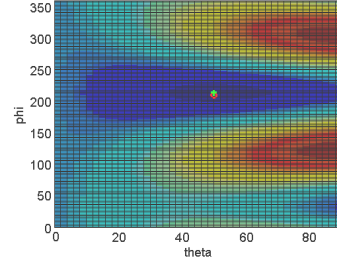


Figure C - 81: $\alpha = 20^\circ$

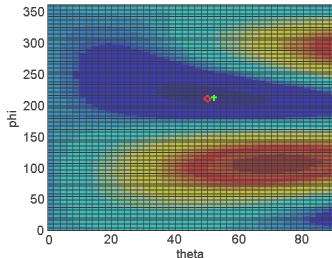


Figure C - 82: $\alpha = 30^\circ$

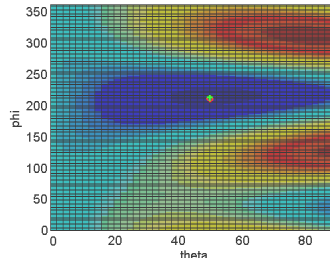


Figure C - 83: $\alpha = 40^\circ$

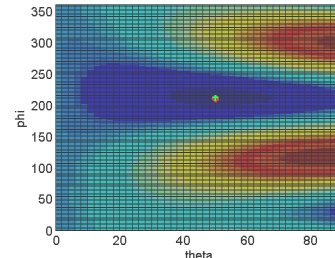


Figure C - 84: $\alpha = 50^\circ$

1.0GHz, with MUTUAL COUPLING

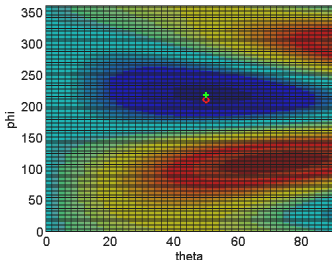


Figure C - 85: $\alpha = 1^\circ$

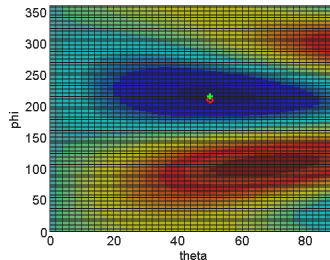


Figure C - 86: $\alpha = 10^\circ$

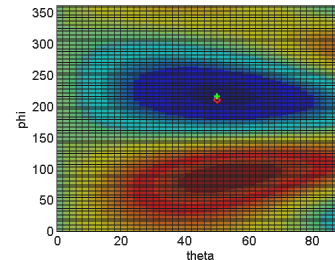


Figure C - 87: $\alpha = 20^\circ$

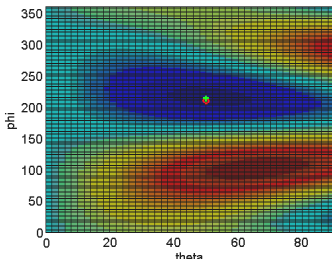


Figure C - 88: $\alpha = 30^\circ$

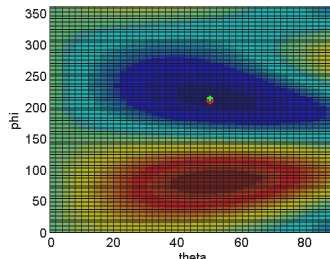


Figure C - 89: $\alpha = 40^\circ$

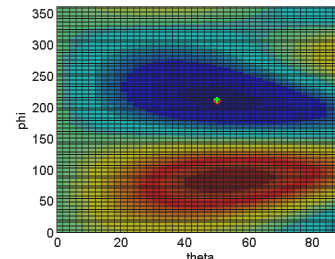


Figure C - 90: $\alpha = 50^\circ$

Maximum Likelihood Results 50mm Antennas

1.5GHz, with MUTUAL COUPLING

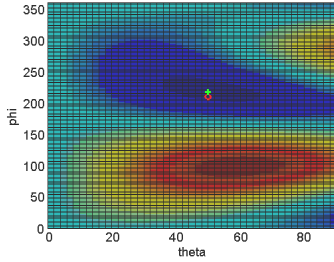


Figure C - 91: $\alpha = 1^\circ$

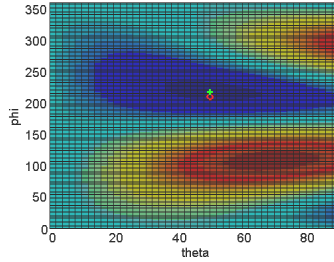


Figure C - 92: $\alpha = 10^\circ$

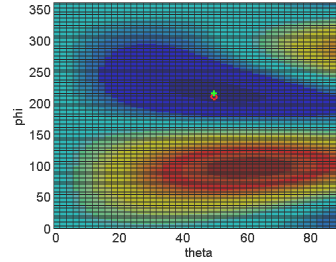


Figure C - 93: $\alpha = 20^\circ$

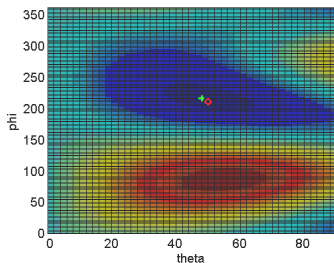


Figure C - 94: $\alpha = 30^\circ$

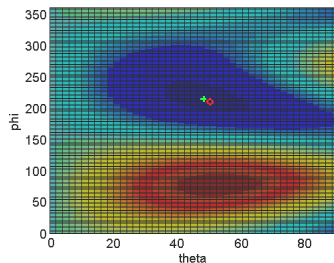


Figure C - 95: $\alpha = 40^\circ$

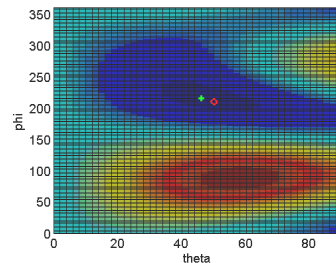


Figure C - 96: $\alpha = 50^\circ$

2GHz, with MUTUAL COUPLING

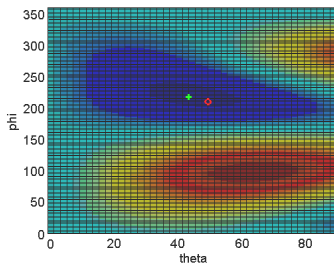


Figure C - 97: $\alpha = 1^\circ$

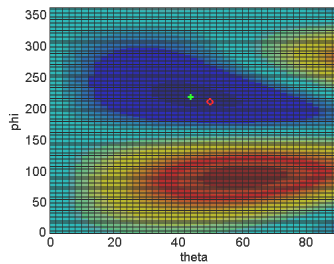


Figure C - 98: $\alpha = 10^\circ$

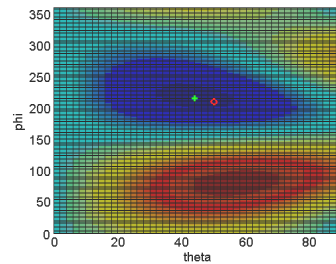


Figure C - 99: $\alpha = 20^\circ$

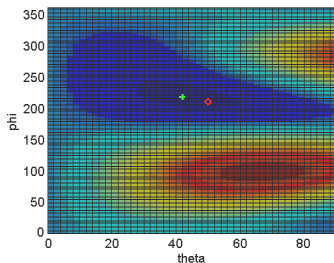


Figure C - 100: $\alpha = 30^\circ$

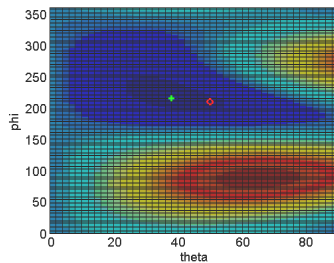


Figure C - 101: $\alpha = 40^\circ$

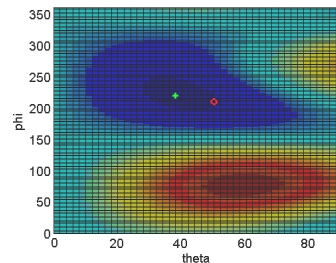


Figure C - 102: $\alpha = 50^\circ$

Maximum Likelihood Results 50mm Antennas

2.5GHz, with MUTUAL COUPLING

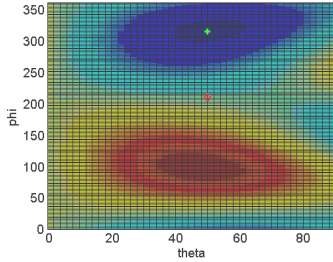


Figure C - 103: $\alpha = 1^\circ$

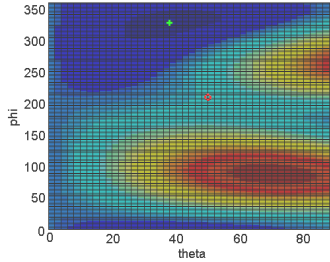


Figure C - 104: $\alpha = 10^\circ$

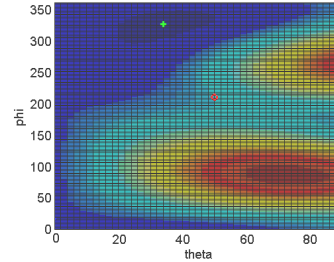


Figure C - 105: $\alpha = 20^\circ$

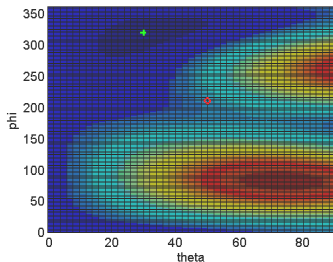


Figure C - 106: $\alpha = 30^\circ$

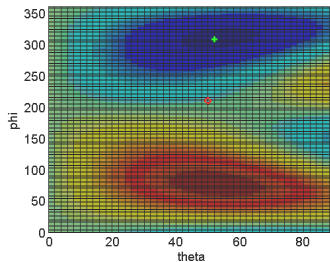


Figure C - 107: $\alpha = 40^\circ$

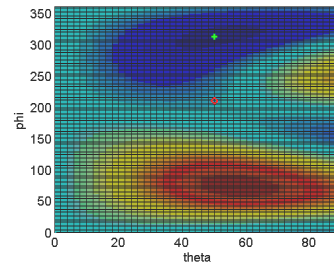


Figure C - 108: $\alpha = 50^\circ$

3GHz, with MUTUAL COUPLING

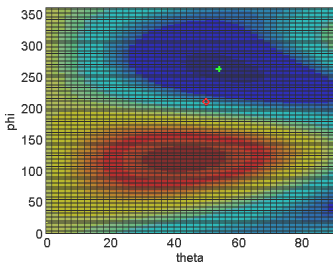


Figure C - 109: $\alpha = 1^\circ$

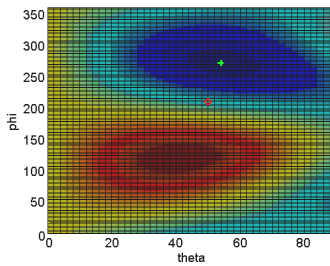


Figure C - 110: $\alpha = 10^\circ$

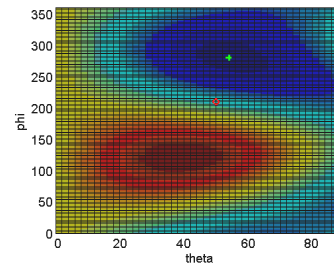


Figure C - 111: $\alpha = 20^\circ$

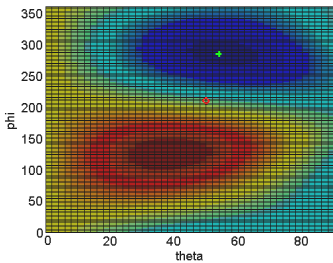


Figure C - 112: $\alpha = 30^\circ$

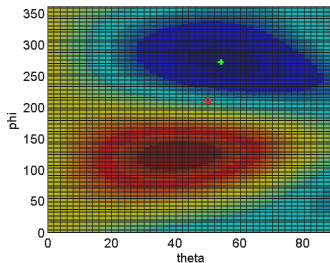


Figure C - 113: $\alpha = 40^\circ$

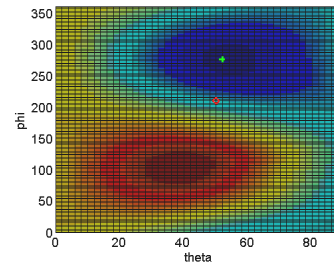


Figure C - 114: $\alpha = 50^\circ$

MUSIC Results 50mm Ant.

Below are the results from using the MUSIC algorithm on the 50mm biconical antennas with $SNR = 35dB$. Note that the scales are not the same on every figure.

0.5GHz, with MUTUAL COUPLING

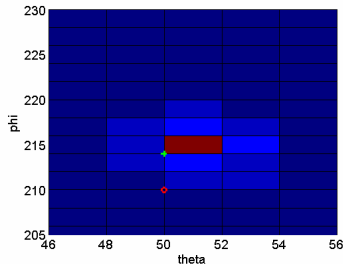


Figure C - 115: $\alpha = 1^\circ$

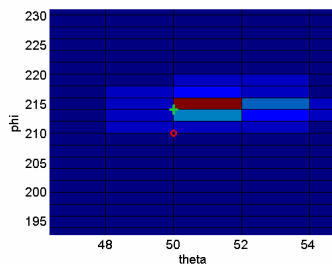


Figure C - 116: $\alpha = 10^\circ$

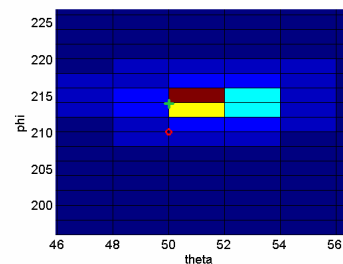


Figure C - 117: $\alpha = 20^\circ$

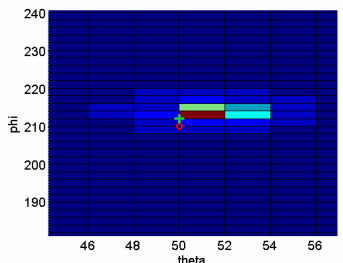


Figure C - 118: $\alpha = 30^\circ$

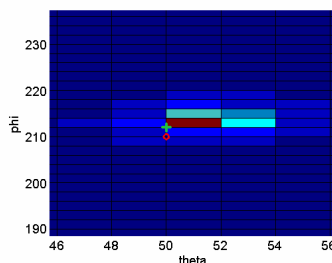


Figure C - 119: $\alpha = 40^\circ$

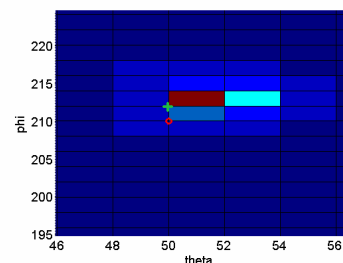


Figure C - 120: $\alpha = 50^\circ$

1.0GHz, with MUTUAL COUPLING

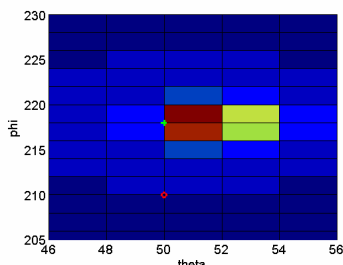


Figure C - 121: $\alpha = 1^\circ$

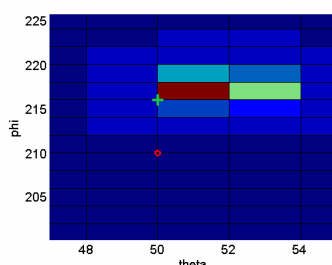


Figure C - 122: $\alpha = 10^\circ$

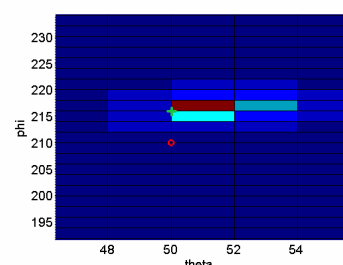


Figure C - 123: $\alpha = 20^\circ$

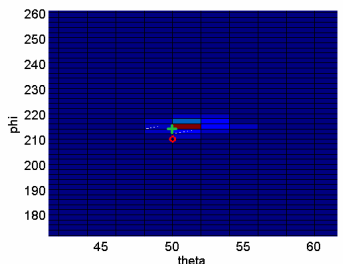


Figure C - 124: $\alpha = 30^\circ$

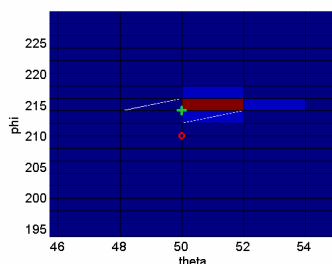


Figure C - 125: $\alpha = 40^\circ$

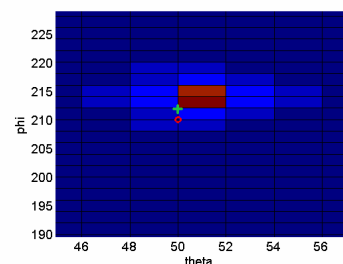


Figure C - 126: $\alpha = 50^\circ$

MUSIC Results 50mm Ant.

1.5GHz, with MUTUAL COUPLING

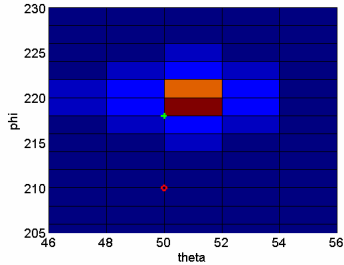


Figure C - 127: $\alpha = 1^\circ$

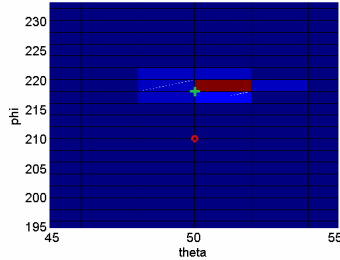


Figure C - 128: $\alpha = 10^\circ$

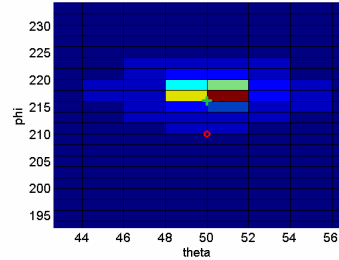


Figure C - 129: $\alpha = 20^\circ$

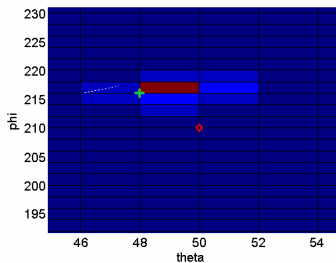


Figure C - 130: $\alpha = 30^\circ$

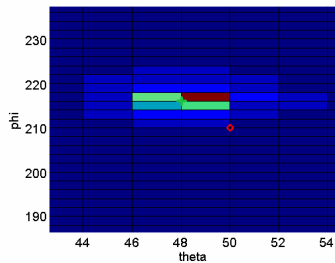


Figure C - 131: $\alpha = 40^\circ$

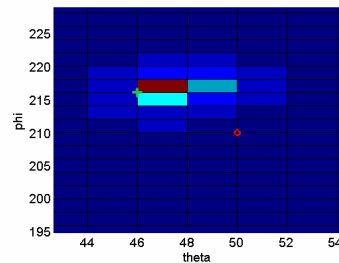


Figure C - 132: $\alpha = 50^\circ$

2.0GHz, with MUTUAL COUPLING

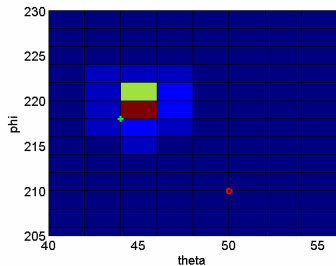


Figure C - 133: $\alpha = 1^\circ$

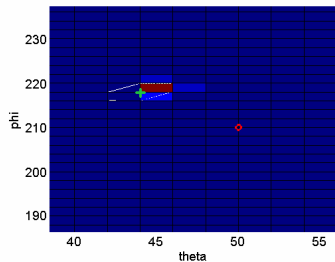


Figure C - 134: $\alpha = 10^\circ$

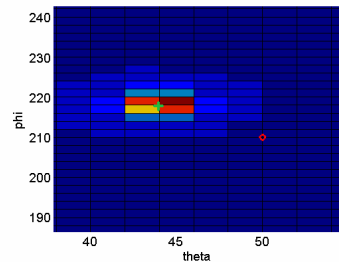


Figure C - 135: $\alpha = 20^\circ$

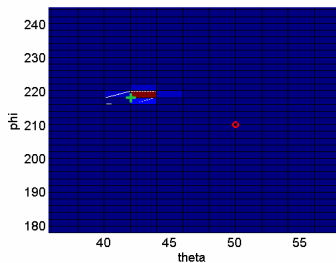


Figure C - 136: $\alpha = 30^\circ$

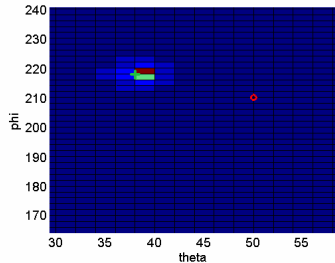


Figure C - 137: $\alpha = 40^\circ$

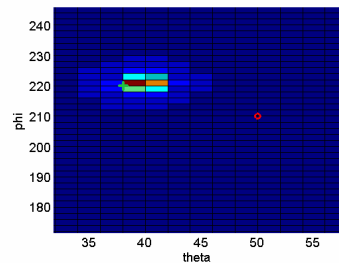


Figure C - 138: $\alpha = 50^\circ$

MUSIC Results 50mm Ant.

2.5GHz, with MUTUAL COUPLING

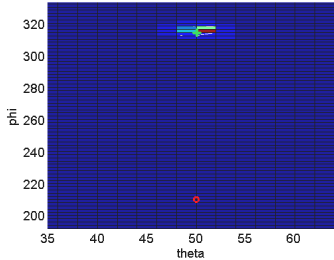


Figure C - 139: $\alpha = 1^\circ$

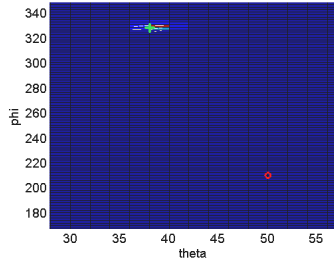


Figure C - 140: $\alpha = 10^\circ$

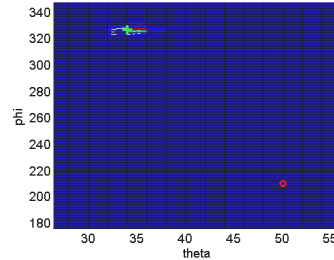


Figure C - 141: $\alpha = 20^\circ$

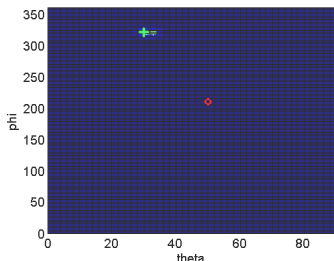


Figure C - 142: $\alpha = 30^\circ$

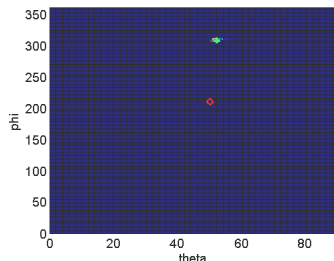


Figure C - 143: $\alpha = 40^\circ$

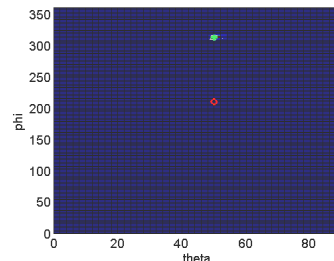


Figure C - 144: $\alpha = 50^\circ$

3GHz, with MUTUAL COUPLING

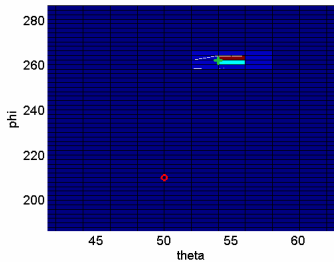


Figure C - 145: $\alpha = 1^\circ$

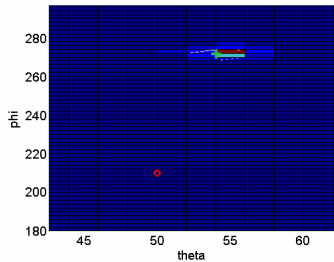


Figure C - 146: $\alpha = 10^\circ$

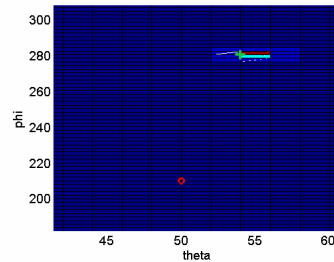


Figure C - 147: $\alpha = 20^\circ$

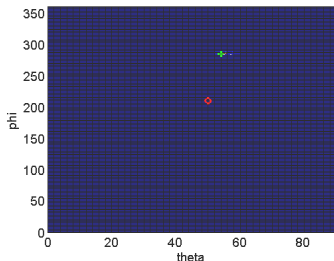


Figure C - 148: $\alpha = 30^\circ$

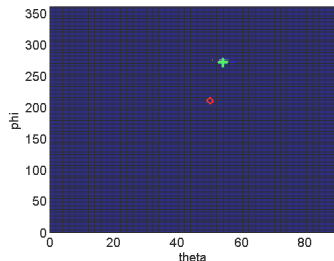


Figure C - 149: $\alpha = 40^\circ$

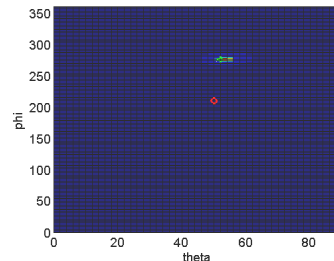


Figure C - 150: $\alpha = 50^\circ$

BIBLIOGRAPHY

- [1] J. D. Moell and T. N. Curlee, *Transmitter Hunting: Radio Direction Finding Simplified*. Tab Books, 1987.
- [2] R. G. Stansfield, "Statistical Theory of D.F. Fixing," *Journal of the Institution of Electrical Engineers - Part IIIA: Radiocommunication*, vol. 94, pp. 762–770, 1947.
- [3] K. T. Wong and M. D. Zoltowski, "Uni-Vector-Sensor ESPRIT for Multisource Azimuth, Elevation, and Polarization Estimation," *IEEE Transactions on Antennas and Propagation*, vol. 45 NO. 10, pp. 1467–1474, 1997.
- [4] T. E. Tuncer and B. Friedlander, Eds., *Classical and Modern Direction-of-Arrival Estimation*. Academic Press, 2009.
- [5] J. W. Nilsson and S. A. Riedel, *Electric Circuits, 7th Ed.* Prentice Hall, 2005.
- [6] C. A. Balanis, *Antenna Theory Analysis and Design, 3rd Ed.* John Wiley & Sons, Inc., 2005.
- [7] R. E. Walpole, R. H. Myers, S. L. Myers, and K. Ye, *Probability & Statistics for Engineers & Scientists, 8th Ed.* Prentice Hall, 2007.
- [8] G. Strang, *Linear Algebra and Its Applications, 4th Ed.* Thomson Brooks/Cole, 2006.
- [9] R. O. Schmidt, "Multiple emitter location and signal parameter estimation," *IEEE Transactions on Antennas and Propagation*, vol. AP-34, pp. 276–280, 1986.
- [10] P. Stoica and A. Nehorai, "Music, maximum likelihood, and cramer-rao bound," *IEEE Transactions on Acoustics, Speech, and Signal Processing*, vol. 37, pp. 720–741, 1989.
- [11] H. Elkamchouchi and M. A. E. Mofeed, "Direction-of-arrival methods (DOA) and time difference of arrival position location technique," *Twenty Second National Radio Science Conference*, vol. 1, pp. 173 – 182, 2005.
- [12] R. Roy and T. Kailath, "ESPRIT – estimation of signal parameters via rotational invariance technique," *IEEE Transactions on Acoustics, Speech, and Signal Processing*, vol. 37 NO. 7, pp. 984–995, 1989.
- [13] F. Gao and A. B. Gershman, "A generalized ESPRIT approach to direction-of-arrival estimation," *IEEE Signal Processing Letters*, vol. 12, NO. 3, pp. 254–257, 2005.

- [14] L. Daldorff, D. Turaga, O. Verscheure, and A. Biem, "Direction of arrival estimation using a single tripole radio antenna," in *2009 IEEE International Conferernce on Acoustics, Speech, and Signal Processing*, 2009.
- [15] J. R. T. Compton, "The tripole antenna: An adaptive array with full polarization flexibility," *IEEE Transactions on Antennas and Propagation*, vol. AP-29, NO 6, pp. 944–952, 1981.
- [16] E. K. N. Yung and C. L. Law, "A simple dbs receiving antenna – a tripole antenna," in *Antennas and Propagation Society International Symposium*, 1989.
- [17] A. Nehorai and E. Paldi, "Vector-sensor array processing for electromagnetic source localization," *IEEE Transactions on Signal Processing*, vol. 42 NO. 2, pp. 376–398, 1994.
- [18] L. L. Monte, B. Elnour, and D. Erricolo, "Design and realization of a distributed vector sensor for polarization diversity applications," in *International Waveform Diversity and Design Conference*, 2007.
- [19] L. Monte, B. Elnour, and D. Erricolo, "Distributed 6d vector antennas design for direction of arrival applications," in *International Conference on Electromagnetics in Advanced Applications, ICEAA*, 2007.
- [20] J. Tabrikian, R. Shavit, and D. Rahamim, "An efficient vector sensor configuration for source localization," *IEEE Signal Processing Letters*, vol. 11 NO. 8, pp. 690–693, 2004.
- [21] K.-C. Ho, K.-C. Tan, and W. Ser, "A study of the resolvability of the vector-sensor array in direction-of-arrival estimation," in *Singapore ICCS '94 Conference Proceedings*, 1994.
- [22] M. G. Morgan and J. W. Raymond Evans, "Synthesis and analysis of elliptic polarization loci in terms of space-quadrature sinusoidal components," *Proceedings of the I.R.E.*, vol. May, pp. 552–556, 1951.
- [23] E. Afraimovich, V. Chernukhov, V. Kobzar, and K. Palamartchouk, "Determining polarization parameters and angles of arrival of hf radio signals using three mutually orthogonal antennas," *Radio Science*, vol. 34 NO. 5, pp. 1217–1225, 1999.
- [24] E. Afraimovich, V. Kobzar, K. Palamartchouk, and V. Chernukhov, "Measureing the full field vector of the ionospheric radio signal on a short-range path when three mutually orthogonal antennas are used," in *Application of the Conversion Research Results for International Cooperation, 1999. SIBCONVERS '99. The Third International Symposium*, 1999.
- [25] E. Afraimovich, V. Kobzar, and K. Palamartchouk, "Determining the interference pattern velocity by analyzing three mutually orthogonal projections of the radio

signal field vector,” in *Application of the Conversion Research Results for International Cooperation, 1999. SIBCONVERS '99. The Third International Symposium*, 1999.

- [26] J. E. F. D. Rio and T. K. Sarkar, “Comparison between the matrix pencil method and the fourier transform technique for high-resolution spectral estimation,” *Digital Signal Processing*, vol. 6, Issue 2, pp. 108–125, 1996.
- [27] X. Wang and Z. xin Wang, “The estimation of the direction of arrival of the spread-spectrum signals with three orthogonal sensors,” *IEEE Transactions on Vehicular Technology*, vol. 51 NO. 5, pp. 817–822, 2002.
- [28] K.-C. Ho, K.-C. Tan, and T. B.T.G, “Linear dependence of steering vectors associated with tripole arrays,” *IEEE Transactions on Antennas and Propagation*, vol. 46 NO. 11, pp. 1705–1711, 1998.
- [29] S. Appadwedula and C. M. Keller, “Direction-finding results for vector sensor antenna on a small uav,” in *Fourth IEEE Workshop on Sensor Array and Multichannel Processing*, 2006.
- [30] C. A. Balanis, *Advanced Engineering Electromagnetics*. John Wiley & Sons, Inc., 1989.
- [31] H. Mott, *Polarization in Antennas and Radar*. John Wiley & Sons, Inc., 1986.
- [32] E. Gillespie, N. Alexopoulos, C. Allen, D. Bodnar, and A. Bresler, *IEEE Standard Definitions of Terms for Antennas*, Antenna Standards Committee of the IEEE Antennas and Propagation Group Std. IEEE Std 145-1983, 1983.
- [33] R. E. Collin, *Antennas and Radiowave Propagation*. McGraw-Hill, 1985.
- [34] D. D. Stancil, “Antenna with multiple co-located elements with low mutual coupling for multi-channel wireless communication,” U.S. Patent 20090174614, 2009.
- [35] W. L. Stutzman and G. A. Thiele, *Antenna Theory and Design*. John Wiley & Sons, Inc., 1998.
- [36] Y. Rahmat-Samii, “Useful coordinate transformations for antenna applications,” *IEEE Transactions on Antennas and Propagation*, vol. AP-27, NO. 4, pp. 571–574, 1979.

REPORT DOCUMENTATION PAGE				<i>Form Approved OMB No. 074-0188</i>	
<p>The public reporting burden for this collection of information is estimated to average 1 hour per response, including the time for reviewing instructions, searching existing data sources, gathering and maintaining the data needed, and completing and reviewing the collection of information. Send comments regarding this burden estimate or any other aspect of the collection of information, including suggestions for reducing this burden to Department of Defense, Washington Headquarters Services, Directorate for Information Operations and Reports (0704-0188), 1215 Jefferson Davis Highway, Suite 1204, Arlington, VA 22202-4302. Respondents should be aware that notwithstanding any other provision of law, no person shall be subject to a penalty for failing to comply with a collection of information if it does not display a currently valid OMB control number.</p> <p>PLEASE DO NOT RETURN YOUR FORM TO THE ABOVE ADDRESS.</p>					
1. REPORT DATE (DD-MM-YYYY) 24-03-2011		2. REPORT TYPE Master's Thesis		3. DATES COVERED (From - To) Sep 2009 - Mar 2011	
4. TITLE AND SUBTITLE Direction Finding With Mutually Orthogonal Antennas				5a. CONTRACT NUMBER	
				5b. GRANT NUMBER	
				5c. PROGRAM ELEMENT NUMBER	
6. AUTHOR(S) Chick, David F., 2d Lt, USAF				5d. PROJECT NUMBER None	
				5e. TASK NUMBER	
				5f. WORK UNIT NUMBER	
7. PERFORMING ORGANIZATION NAMES(S) AND ADDRESS(S) Air Force Institute of Technology Graduate School of Engineering and Management (AFIT/EN) 2950 Hobson Way WPAFB OH 45433-7765				8. PERFORMING ORGANIZATION REPORT NUMBER AFIT/GE/ENG/11-03	
9. SPONSORING/MONITORING AGENCY NAME(S) AND ADDRESS(ES) Air Force Research Laboratory, Radio Frequency Sensor Technology Division (AFMC) Attn: Dr. Charles Cerny 2241 Avionics Circle, Bldg 620 WPAFB OH 45433-7318 (937) 255-2620 x4067 (DSN 785-2620), charles.cerny@wpafb.af.mil				10. SPONSOR/MONITOR'S ACRONYM(S) AFRL / RYMRA	
				11. SPONSOR/MONITOR'S REPORT NUMBER(S)	
12. DISTRIBUTION/AVAILABILITY STATEMENT APPROVED FOR PUBLIC RELEASE; DISTRIBUTION UNLIMITED					
13. SUPPLEMENTARY NOTES This material is declared a work of the U.S. Government and is not subject to copyright protection in the United States.					
14. ABSTRACT Estimating the direction-of-arrival of incident electromagnetic plane waves (a.k.a. direction finding or DF) has typically been accomplished in the past using arrays of spatially separated antennas. The spatial separation produces a delay in each antenna's measured voltage due to the finite propagation time as the wave strikes each antenna in succession. In this thesis, we approach the problem differently by using three antennas that have been oriented in orthogonal directions but are co-located at the origin of a coordinate system. Being co-located, this mutually orthogonal arrangement of antennas cannot detect the propagation phase delay and must rely solely on the polarization properties of the incident waves. Using the vector effective height concept, three algorithms are formulated. The first algorithm estimates the direction-of-arrival by computing a vector that is perpendicular to the locus of the instantaneous electric field vector. The second and third algorithms are based on the well-known maximum likelihood and MUSIC algorithms. Simulation results show that each algorithm can estimate the direction-of-arrival with a root-mean-squared error within 1° or less when the incident wave is circularly polarized, the antennas are small compared to wavelength, and the signal-to-noise ratio is above 20dB.					
15. SUBJECT TERMS Mutually Orthogonal Antennas, Direction Finding, Direction-of-Arrival Estimation, Tripole					
16. SECURITY CLASSIFICATION OF:			17. LIMITATION OF ABSTRACT UU	18. NUMBER OF PAGES 157	19a. NAME OF RESPONSIBLE PERSON Dr. Andrew Terzuoli, Jr. (ENG)
REPORT U	ABSTRACT U	c. THIS PAGE U			19b. TELEPHONE NUMBER (Include area code) (937) 255-3636 x4717 andrew.terzuoli@afit.edu

Standard Form 298 (Rev. 8-98)

Prescribed by ANSI Std. Z39-18